Defect-stabilised Pt catalysts on UiO-66(NH_2)

Andrew Jones

Thesis submitted to the University of Nottingham for the degree of Doctor of Philosophy

Supervised by:
Dr Matthew Cliffe, Dr Jesum A. Fernandes
Dr Anabel Lanterna, Dr Sanliang Ling

University of Nottingham, UK
September 2024

I, Andrew Jones confirm that the work presented in this thesis is my own. Where information has been derived from other sources, I confirm that this has been indicated.

Abstract

This thesis broadly explores the use of the metal organic framework (MOF) UiO-66(NH_2) as a support material for photocatalytic hydrogen generation.

Hydrogen generation is an important reaction in sustainable catalysis, with the potential to create hydrogen fuel using sunlight energy, improving upon the current methods such as steam reforming, which produce CO_2 emissions during hydrogen generation. Hydrogen is an ideal candidate for an energy carrier in a net-zero fuel economy, and its production using sunlight is a highly promising prospect to contribute to the global effort of circumventing CO_2 emissions and reducing anthropogenic global warming.

UiO-66(NH_2) is an analogue of the highly popular MOF UiO-66, where UiO-66(NH_2) is composed of $Zr_6O_4(OH)_4$ zirconium-oxo clusters and linkers of 2-amino terephtalate. These building units co-ordinate into extended macromolecules developing a crystal structure with networks of high porosity. UiO-66, and its analogues exhibit relatively high thermal and chemical stability, an essential trait for catalyst supports. These MOFs also display a very high tunability, with the ability to replace the metal and organic components with certain candidates, while maintaining the crystal structure. UiO-66 family MOFs are perhaps most distinguished by their ability to form defects, which have been observed to present in a variety of ways, with the possibility for both cluster and linker vacancies, and phases of the material which naturally incorporate defects.

This research aims to use UiO-66(NH_2) catalysts to create more sustainable catalysts, by reducing sintering during catalysis. Sintering is a significant cause for loss of catalyst activity for catalysts where an active site is immobilised upon a support material. Agglomeration of the

catalyst particles reduces the surface proportion of atoms, and therefore the proportion of catalytically active atoms.

Chapter 4 presents a body of work in which I introduce missing linker defects to UiO-66(NH_2) in varying quantities, measuring the physical properties of the MOF using PXRD and SEM, and quantifying the missing linker concentrations by TGA. I explore the effects of missing linkers on catalytic activity towards photocatalytic hydrogen generation, and conduct post mortem analysis to measure nanoparticle sintering to assess the efficacy for missing linker defects introducing 'anchor sites' at which to stabilise catalyst nanoparticles.

Chapter 5 presents work which occurred in parallel with *Chapter 4*, developing and optimising a photocatalytic reactor cell to maximise the observed hydrogen generation from UiO-66(NH_2) photocatalysts. This chapter investiagtes key design parameters in a photocatalytic reactor, and achieves large increases in the observed rate of photocatalysis by applying the same catalyst to a new reactor. The development of this reactor was key to highlight changes in rate of H_2 generation in both *Chapters 4 and 6*.

Chapter 6 Investigates another approach to sustainable heterogeneous catalysis. Instead of stabilising Pt catalysts, I implemment Nickel and Nickel/ Platinum mixed metal catalysts, with the aim of using cheaper, more earth-abundant metals for photocatalysis.

Acknowledgements

First, I would like to thank my lead supervisor, Dr Matthew Cliffe, a brilliant supervisor from whom I have learned so much. Thank you for always having time for your students and always getting the best from us. I would also like to thank my other supervisors: Dr Anabel Lanterna, Dr Jesum Alves Fernandes and Dr Sanliang Ling, thank you for your advice and patience over the years.

Next, I would like to thank everybody from the Cliffe and Pilgrim groups in B52, past and present. I have enjoyed the company every day, and I will miss your presence at work. Particular thanks goes to Jem Pitcairn, who solved so many TOPAS and Python problems for me.

I have received help and advice from so many people over the course of my PhD. Dr Emerson Kohlrausch, Dr Ian Candillo-Zallo, Dr Andreas Weilhard, Prof. Andrei Khlobystov, Dr Mike Fay, everybody in workshops and glassblowing. Thank you to all of these people who have assisted in various analytical techniques, or building the reactors that I always seem to break.

Thank you to all of my family. My parents for always encouraging me and showing interest in my work. My siblings: Bethan, Russell, Kayleigh, Lisa and all their respective partners who will be thrilled to hear I will now be getting a 'real job'.

Most importantly, thank you to Chloe, who kept me sane during my thesis writing, supported me through my journey and always provided reassurance when it was needed.

Last but not least, I want to thank myself for doing all this hard work.

Table of Contents

List of Figures

List of Tables

Chapter 1

Introduction

1.1 Catalysis

Catalysts are components of chemical reactions which decrease the activation energy of a reaction by providing alternative reaction pathways to reach the product, while remaining themselves chemically identical after the catalytic cycle. Restoration of the catalyst's identity after each reaction mean small amounts of a catalyst can induce large numbers of turnovers, with each active site able to catalyze thousands of reactions. The reduced activation energy from a catalyst provides the benefit of both faster rates of reaction and potential for milder reaction conditions.

Catalysts are broadly divided into two categories: homogeneous and heterogeneous catalysts. Homogeneous catalysts are in the same phase as reactants (liquid), and heterogeneous catalysts are in another phase (e.g. solid catalysts with gaseous or liquid reactants).

Homogeneous catalysts are typically dissolved in a solvent, catalysing reactions in the liquid phase. In this state, homogeneous catalysts are highly dispersed, meaning that each active site is available for reaction, which creates an innately highly active catalyst. When a heterogeneous catalyst is a metal, they commonly have ligands, which have a profound effect on the catalyst metal's catalysis. As such, ligands can be tailored, affecting steric and electronic effects at the active site, allowing for a high degree of control over the catalyst's properties such as activity and selectivity. The drawback of homogeneous catalysts, however, is that they can not be easily separated from reaction products. As the

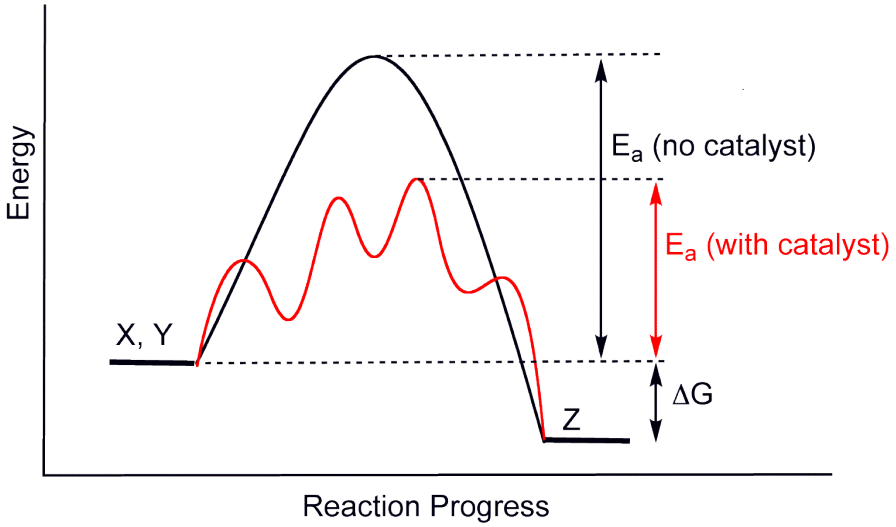

Figure 1.1: Example potential enerygy diagrams for a reaction progressing with (red) and without (black) a catalyst. The alternative reaction pathway created by catalyst presence has caused the reaction to progress through multiple intermediates, and given a lower activation energy (E_a). Reproduced from https://en.wikipedia.org/wiki/Catalysis, accessed 16.08.2024.

catalyst is dissolved, chemical processes are required to remove the catalyst for product purification and catalyst recycling. Catalyst removal is expensive, time consuming and produces waste products which require treating and removal. As a consequence, heterogeneous catalysis is favoured in industry, to avoid the difficulty of homogeneous catalyst separation. Over 75% of reactions in industry utilize heterogeneous catalysts. Heterogeneous catalysts can be easily removed from the products in physical processes, and they can be very easily be recycled ready for use in the next reaction. The difference in separation procedures between homogeneous and heterogeneous catalysts is so great that often it is economically beneficial to move away from a homogeneous catalyst, to a less active heterogeneous catalyst for the ease of separation.

Aside from enzymes, the vast majority of catalysts utilize transition metals as the active site. Transition metals are effective catalysts as they have multiple stable oxidation states. Some of the most active catalysts are the platinum group metals(PGMs), such as platinum, palladium and ruthenium. Their high activity can often be attributed to the Sabatier principle, which dictates that a catalyst must bind reactants and intermediates at its surface with moderate strength. If a metal binds too weakly, reaction kinetics will be hindered. If the metal binds intermediates or reactants too strongly, desorption is sluggish, occupying active

sites and reducing the turnover number.[1]Platinum group metals often exhibit optimal adsorption strength, allowing catalytic activity and desorption to occur quickly, which is the Sabatier optimum. The Sabatier principle is commonly depicted as 'volcano plot', Fig. 1.2. The elements at the apex of the volcano are those with optimal binding for reactions and desorption.

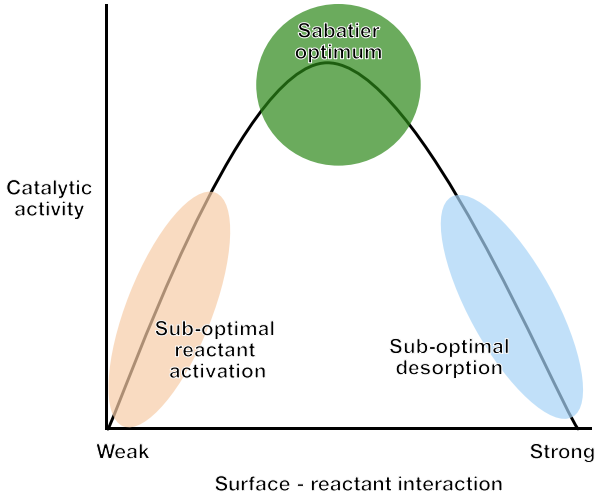

Figure 1.2: A volcano plot, graphically representing the Sabatier Principle. Species with stronger surface - reactant adsorption will quickly produce products, but slowly desorb the products, occupying the active sites for the next reaction.

1.1.1 Catalyst synthesis

In a heterogeneous catalyst, only the surface atoms are available for reactions. This means that a pure species of the active catalyst will be an inefficient use of the material. Metals are non-porous and display low specific surface areas, therefore most atoms present in a sample will not be accessible for a reaction when in their bulk metallic form. To address these issues, catalyst supports can be employed, upon which, small particles of active catalyst can be deposited, generally in the range of 1 –10 wt %. This creates a more cost effective catalyst by reducing the amount of costly metal, and creating a stable catalyst with respect to catalyst dissolution. Porous supports such as zeolites, nanotubes, and alumina are particularly useful, as their high surface area allows for a high dispersion of metal nanoparticles.

Catalysts are deposited onto support materials through different techniques. These are broadly split into two categories: top-down, wherein bulk metals are fragmented or atomised into the desired size

of particle, and bottom-up wherein dispersed atoms are agglomerated into particles.[2] Most commonly, catalyst deposition is through chemical methods, such as wet impregnation or coprecipitation. These techniques use dissolved metal precursor cations, such as Pd^{2+}, which are then reduced to cause a precipiation at the surface of a support material. Once precipitated, catalyst atoms can adsorb to a support material, immobilising the catalyst. This is popular due to the low technological barrier to entry, coprecipiation can be performed in a round-bottomed flask, requiring little technical equipment compared to alternative methods. Coprecipitation allows for catalysts to be easily dispersed into pores and interlayer cavities to maximise separation, minimise particle size and potentially utilise confinement effects.[2] While this technique is very effective, coprecipitation methods produce large amounts of waste products. When metal salts undergo redox reactions to induce precipitation, there is significant waste derived from the cation and reducing agent. This waste can be avoided by using physical deposition methods rather than chemical ones.

When precipitating salts into elemental metal, the anions are waste side-products and must be disposed of or recycled, which could be avoided using physical methods rather than chemical.

A deposition technique to minimise waste is magnetron sputtering, a physical process in which elemental metal forms a condensable vapour that is directly deposited onto support material. This technique is highly scalable, and practised within the industry of surface coatings on multi-ton scales[3]. At reduced pressures ($\leq 10^{-6}$ atm), a potential difference is applied through a working gas (in this thesis argon) between an anode and cathode, where the cathode is the 'target metal'. The potential difference applied causes ionisation of the Ar to Ar^{+}, in a discharge glow. Ar^{+} cations are accelerated towards the negative biased cathode, causing very high velocity collisions between Ar^{+} and target metal. These high energy collisions provide a momentum exchange between Ar^{+} and the metal surface, and if the energy is sufficient, single atoms are ejected from the target metal.[4] As metal atoms are vaporized, simultaneously, secondary electrons are also emitted. These secondary electrons are strongly repelled by the negatively biased cathode, and often possess enough energy to ionise surrounding Ar as a result. By placing a magnet behind the cathode, electron lifetime in its vicinity is extended. This is achieved by creating a trap using the electric and magnetic fields in

unison, causing almost all Ar ionisations to occur next to the cathode target. The introduction of magnets provides higher sputtering deposition rates through localised ionisations, allowing for lower working gas pressure and lower discharge voltages, saving time and energy.[4,5]

Magnetron sputtering is a sustainable deposition technique because it creates little waste. Elemental metal which is deposited inside the pressure chamber and not onto catalyst support can be recycled easily, and this waste is proportionally very small in industry.[3]

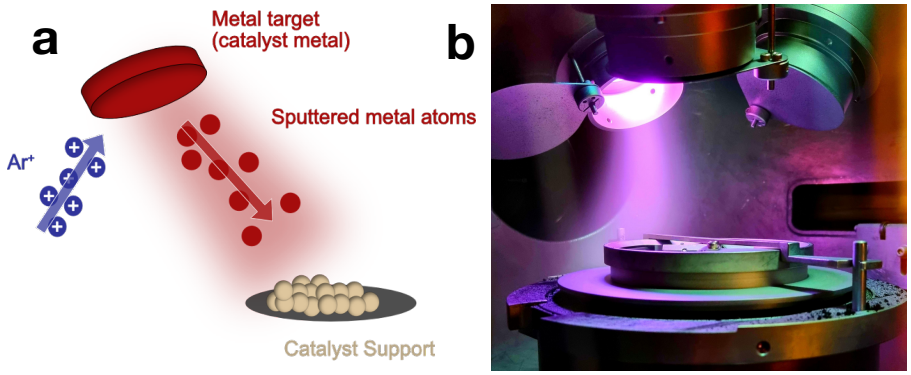

Figure 1.3: (a) Illustration of the magnetron sputtering process for depositing a catalyst onto support material (b) The magnetron sputtering chamber at the University of Nottingham in operation, colours accurate. Purple colours present at the catalyst target are from the plasma present, created by secondary electrons at the cathode.

1.1.2 Catalyst Supports

Catalyst supports are available in many forms, and can be differentiated at their base level, according to the general structures. These can be further differentiated by the sample-specific properties. For example, a common photocatalytic support is TiO_2, synonymous with photocatalytic hydrogen generation due to its efficacy, price, accessibility and non-toxicity. Titania can be found naturally as the minerals rutile, anatase and brookite, which have different band gaps. Beyond these basic structures, support materials such as P90 are used, which are a mixture of two crystalline forms (92% anatase, 8% rutile), or even supports containing amorphous TiO_2 such as PC500. Broadly speaking, support materials can be grouped into: metal oxides, carbonaceous (nanotubes, carbon nitride, graphene) or framework materials (COFs and MOFs), though there are other supports which do not fit exactly into these criteria such as nitrides.

Specific support materials are chosen to suit the requirements of an application, key considerations are: stability, surface electronics, porosity and surface area. Specifically to photocatalysis is also the optical properties, as UV and visible absorption is the most important factor.

1.1.3 Sustainable Catalysis

Elemental sustainability is an important topic in catalysis, as catalysts are often composed of metals in short supply, such as PGMs, which are commonly relied upon due to their outstanding catalytic properties in many applications. Due to the scarcity of PGMs these are often difficult to extract from ore, leading to high energy demand. To preserve our natural resources and drive the chemical industry more sustainably, reduction of our PGM use in catalysis is a major target. Achieving sustainable use of natural resources, such as PGMs, is key to achieving UN Sustainable Development Goal 12 - Responsible consumption and production.[6] Three particularly popular PGM catalysts are platinum, palladium and rhodium. Fig. 1.4 displays the increasing demand for these PGMs over time, over half of the demand for most PGMs can be attributed to catalytic applications.[7]

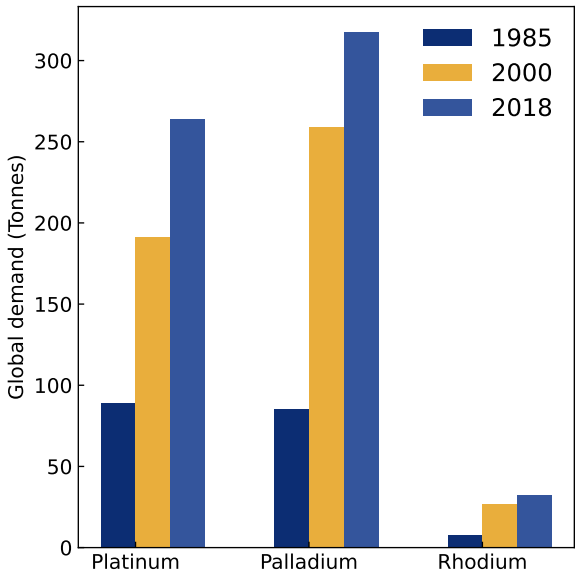

Figure 1.4: The demand for platinum, palladium and rhodium growing from 1985 to 2018, an increase largely driven through catalysis.[7]

Some of the metrics associated for PGM primary production are listed in Table 1.1.[8] These metrics highlight the requirement to most efficiently

utilise PGMS,to reduce demand for extraction and primary production, therefore reducing energy usage, carbon emissions and water consumption.

Metal	GWP kg CO_2 eq.	PED MJg^{-1}	BWC kg g^{-1}
Pt	41.8	464.9	265.1
Pd	25.3	318.9	172.5
Rh	36.9	414.2	242.8

Table 1.1: Global Warming Potential (GWP), Primary Energy Demand (PED) and Blue Water Consumption (BWC) for primary production of one gram of Pt, Pd and Rh. Primary production includes the processes: Mining and crushing, concentration, smelting and purification.[8]

One popular approach to make more sustainable catalysts is to substitute PGMs entirely for more sustainable, earth abundant metals, such as Cu and Ni.[9] This is very useful where possible, as it preserves our natural resources, and allows PGMs to be applied where they are strictly irreplacable. In some cases, the catalysis itself is an instance of an irreplacable application, due to the much increased activity of PGMs in catalysis. An example of such reaction is platinum co-catalysts in photocatalytic hydrogen generation. This reaction is important to target clean fuel production, and is discussed more in the later sections *Hydrogen generation* and *Hydrogen in Green Chemistry*.

If replacement of a PGM is detrimental to the activity of a catalyst, reducing the amount of PGM required is the logical next process. If this is executed while increasing the specific activity of the PGM catalyst, the catalysts are becoming more sustainable.

Reducing the size of catalyst particles is often an effective way of improving the specific activity of a heterogeneous catalyst, allowing for catalyst material to be saved. By reducing the size of our particles, we are able to reduce the proportion of atoms which exist below the surface, thereby increasing the specific activity. This concept of proportionally available atoms is called atom utilization, and it is important to maximise the atom utilisation to create sustainable catalysts.

1.1.4 Nanocatalysts

Classical supported metal heterogeneous catalysts contain metal particles with a broad size distribution and irregular morphologies , where

only a fraction of the metal atoms (those at the surface) can function as active sites.[10] Due to the heterogeneity of the material, the atoms that do exhibit catalytic activity display different performances, and ultimately different selectivities.[10]

Heterogeneous catalysts are now produced with size as a primary consideration- nanocatalysts and single atom catalysts (SACs) provide higher specific activity than the classical heterogeneous catalyst, which is achieved through a higher atom utilization. Fig. 1.5 displays the relationship of nanoparticle size and surface atom proportion (which is directly linked to atom utilization) through an example for cuboctohedral Pt.[11] This figure uses the 'magic number' of atoms for each nanoparticle, which is the fixed number of atoms required to produce a nanoparticle of a specific symmetry.[12] This figure shows the trend that, smaller nanoparticles have larger surface atom proportions, and by extension higher atomic utilisations. This increased atomic utilisation means that smaller catalyst nanoparticles are have a higher specific activity than their larger nanoparticle equivalents.

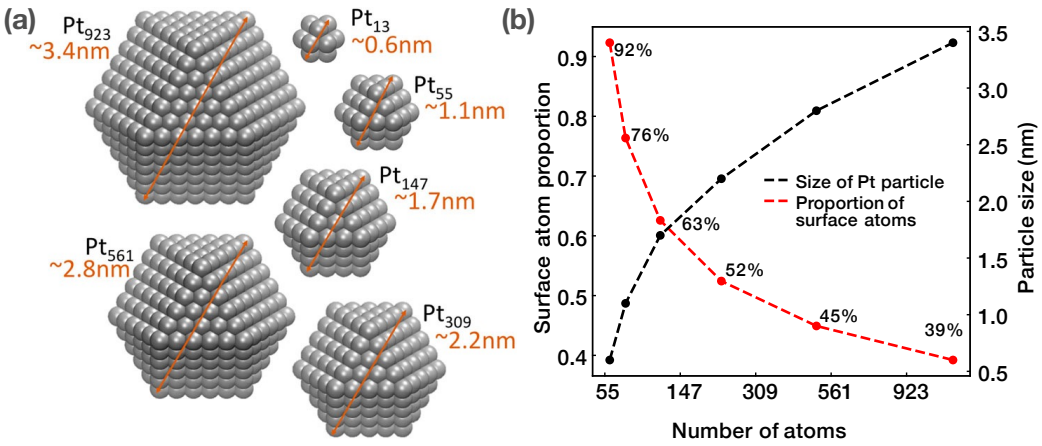

Figure 1.5: (a) Platinum cuboctohedral nanoparticles of the first 6 magic numbers, reproduced from ref [12] (b) The number of atoms, particle size and surface atom proportion for each of those nanoparticles

The defining feature for SACs is that every catalyst atom is available as an active site, therefore fully using the potential of the catalyst material. They consist of discrete single atoms of active catalytic metals anchored to supports and are used as heterogeneous catalysts. SACs take the principle of atom utilisation to its absolute limit. The specific activity of SACs is beyond what can be achieved with supported nanoparticles, stemming primarily from this 100% atom utilisation.[13] This enhanced activity is demonstrated in research by *Hejazi et al*[14] . In their research,

the activity of Pt SACs @ TiO_2 towards photocatalytic hydrogen generation was compared with large nanoparticles upon the same support. The specific activity of Pt SACs was found to be 150 times higher than that of the equivalent nanoaparticle species, indicating clearly the ability of SACs to more efficiently utilise catalyst material.

SACs are never found in a system as solely single atoms, because of their high surface energy, and thus mobility which causes enthalpically favoured agglomeration. SACs are accompanied by at least nanoclusters (NCs) <2 nm and often nanoparticles (NPs) >2 nm. NCs (generally comprised of 20 or less atoms) are often referred to under the umbrella term of SACs, which is because SACs and NCs display similar properties. NCs often orient such that every atom is present at the surface either due to their small size or 2D morphology, this allows NCs to show 100% atom utilization and similar electronic properties to SACs, Figure 1.7[13].

Atom utilization could be considered the most important variable when altering the particle size of nanocatalysts, though in many instances electronic effects have shown to be more important to the activity of a catalyst. The electronic effects of nanocatalysts change drastically within small particles (<100 atoms), an example of which can be seen in Fig. 1.6. This shows how the work function of Au nanoparticles changes according to the atomicity, and emphasises the volatile electronic properties of particles containing 20 or fewer atoms. The electronic states of SACs and nanoclusters are distinctly different from those of a larger nanoparticle, due to the quantum size effect, in which electrons are confined into a smaller space and thus have more widely spaced energy levels.[10] Instead, the electronic energy levels are discrete, with distinct HOMO-LUMO gaps. The effect of particle size on electronic states is displayed in Fig. 1.7.

SACs also benefit from metal-support interactions at every active site, allowing all of catalyst atoms to benefit from the associated stability increase, and the electron transfer directly between active sites and support material.[15] One electronic feature of SACs, which is most important to this research, is the affect of a SAC's electronic properties depending on its co-ordination environment. It is well established that support materials have a significant effect on the supported active catalyst species, and this effect is even more pronounced with SACs than larger particles, as the co-ordination enviornment is effectively acting like a ligand

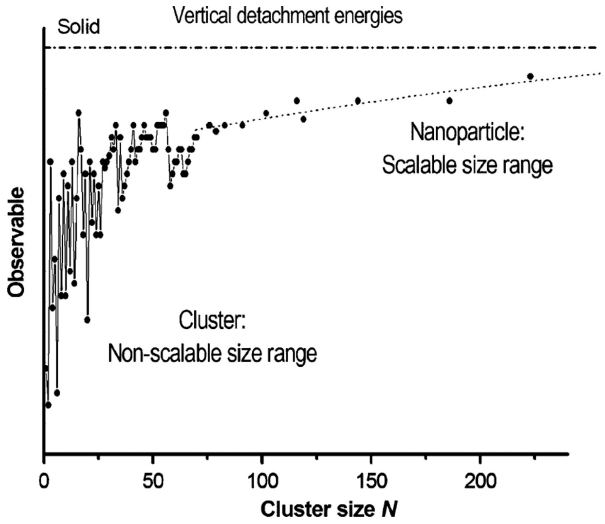

Figure 1.6: The experimentally calculated work function for Au nanoparticles according to the number of atoms present in the nanoparticle. Reproduced from [10]

in homogeneous catalysts. This increased influence from the surroundings makes SACs more tunable than NPs, therefore allowing them to be optimised for specific properties or reactions.

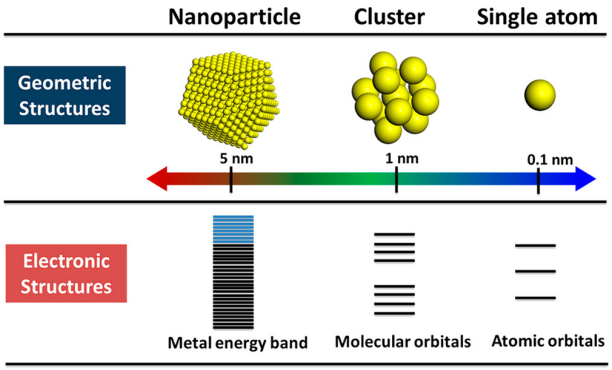

Figure 1.7: Geometric and electronic structures of NPs, NCs and SACs. Reproduced from [15]

Single atom catalysts have been synthesised and characterised in many publications, summarised in a range of useful reviews.[10,13,16] SACs have been shown to be extremely effective in a range of applications, for example Pd(II) @ Al_2O_3 SACs have been shown to produce the highest ever reported activity for cinnamyl alcohol oxidation, a common reaction benchmark reaction for oxidation catalysts.[17]

The main limitation of SACs is their stability to sintering and leaching. The high surface free energy of SACs causes arrangements of atoms within nanoparticles to be more thermodynamically stable than in SACs, and generally SACs have high mobility on the surface.[10,15] Leaching is to be expected in heterogeneous catalysis to some degree, however is more

prevalent in SACs. Isolated single atoms are much more easily removed by solvation than those already stabilised within a nanoparticle.

Heating Pt NPs in the presence of O_2 actually reverses the process of sintering, reverting Pt NPs back to SACs.[18] There are other cases which display resistance to sintering, such as *Qiao et al*[19] reporting single atoms of Pt which are very stable with respect to sintering over long reactions.

1.1.5 Photocatalysis

Solar energy is an ideal source of renewable energy as it is available in large quantities, is effectively infinite and present around the world. Harnessing this energy to fuel the chemicals industry and the energy transition from fossil fuel reserves is one of the most promising options available. One such method to harness solar energy is through photocatalysis, utilising photons to provide energy for chemical transformations.

The thermal route is the most common energy source for catalysis, where the energy is transferred to the active sites through conduction from the heat source. For photocatalysis, the energy source is light, and reactions occur exclusively in species excited by incident photons of the light source. Photoexcitation creates an excited electron which is promoted to higher energy, and an associated positive 'hole' where the photoelectron originated[20]. The photoelectron and hole are very strong reducing and oxidising agents respectively[21].

This thesis focuses on heterogeneous supports with nanoparticles deposited onto them. To clarify the terms which are not obvious to those not familiar with photocatalysis: The 'support' material, which absorbs the light but is not neccesarily the active site for catalysis is the catalyst. The nanoparticles deposited onto the support material are referred to as the co-catalyst, where the co-catalysts are the active sites, the mechanisms through which co-catalysts function are discussed in this section.

The process for photocatalysis is:
(a) Absorption of a photon of sufficient energy to generate an electron-hole pair.
(b) Electron promotion from occupied molecular orbitals (or valence

band in a semiconductor) into the a high energy state. This creates an excited, high energy photoelectron and an associated positive 'hole' where the photoelectron originated.
(c) Holes and photoelectron migration to the photocatalytic surface.
(d) Charge carriers' strong redox potentials induce reaction with an adsorbed chemical.[22]

The process of photocatalysis in a semiconductor with Pt co-catalysts is depicted in Fig. 1.8

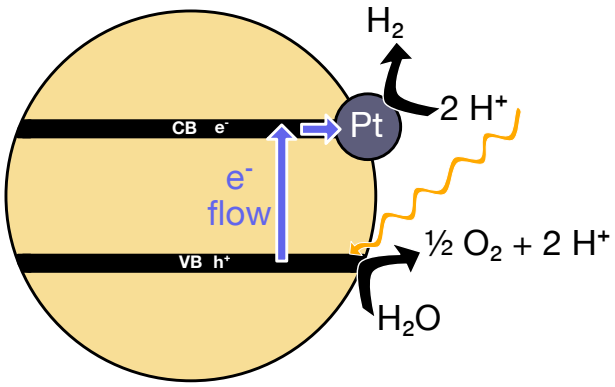

Figure 1.8: A schematic for photocatalytic water splitting in a Pt-doped semiconductor. Light is absorbed, promoting electrons from the valence band (VB) into the conduction band (CB), generating a hole and photoelectron at each respectively. The photoelectron migrates from the CB to the Pt particle, which in this case is the photocatalytic surface. The high redox potentials of the photoelectron and hole mediate reduction and oxidation respectively, and after reactant desorption, restoring the catalyst to its original state.

Where the heating mechanism for thermal catalysis inputs large amounts of non-specific energy, and hence leads to significant sintering, photocatalytic light energy is much more specific. Photons are absorbed at the chromophores for more direct, efficient translation translation of input energy to the catalyst. The benefit of this more direct energy source is that reactions are able to perform under milder working conditions. By removing non-specific energy, and creating a thermally milder environment, catalyst atoms have less mobility and will typically sinter more slowly than in thermal catalysis. Milder operating conditions also provide less hazardous reaction conditions and satisfy a core principle of green chemistry[23]. The mild reaction conditions are also useful for supports with relatively poor thermal stability e.g. MOFs, where the activation energy may not be met under thermal conditions before the support thermally decomposes.

One of the biggest challenges in photocatalysis is that of recombination,

the process in which photoelectrons return to the position of the photogenerated hole, as depicted in Fig.1.9. This process is problematic, wasting photoelectron energy and releasing heat from relaxation.[24] The heat energy is not productive for the reaction therefore this reduces the quantum efficiency, the measure of proportionally how many absorbed photons induce desired reactions. The address this problem, one must increase photoelectron lifetime by stabilising the photoexcitated state, this is achieved primarily through use of heterostructures, at which heterojunctions are created. A heterojunction is the interface between two semiconductors which have different band structures, and at their interface, semiconductors establish an equalized Fermi level, which creates an electric field (Fig.1.10). This field promotes electron-hole separation, thus reducing recombination and increasing quantum efficiency.

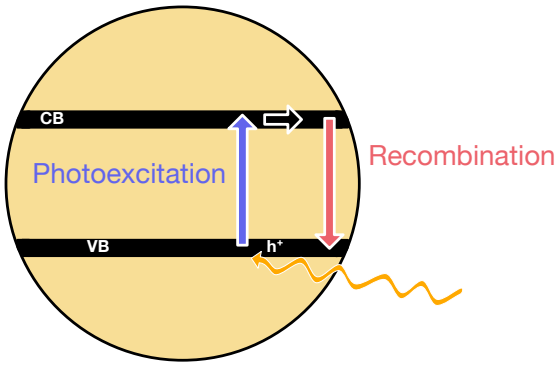

Figure 1.9: Electron photoexcitation in a semiconductor, followed by recombination. Thus the photocatalyst is unable to induce a reaction before another photon is absorbed to produce a new photoelectron hole pair.

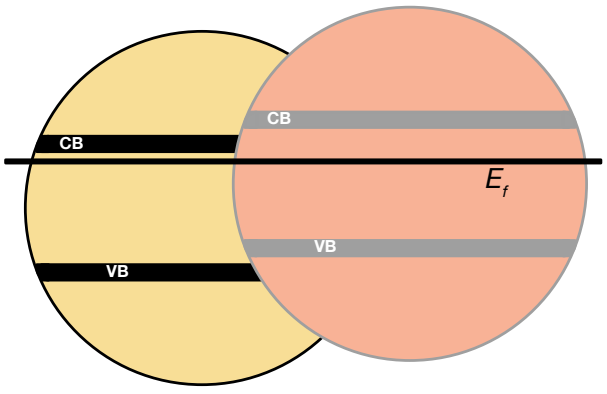

Figure 1.10: A heterojunction of two semiconductors, at which the Fermi level is equalized.

Another common approach to reducing recombination, the primary approach in this thesis, is through use of a co-catalyst. At the interface

of a co-catalyst particle and band-structured support material, a Schottky junction is created (Fig. 1.11). This junction creates 'band bending' in the support material, at the CB at the semiconductor- cocatalyst interface. Bending at the interface is not an immediate change, but rather a gradual change in energy levels over the course of multiple lattice spacings (a few nm). The energy levels make photoelectron flow to co-catalyst more favourable, and likely to occur. The co-catalyst serves as an effective electron trap, and reduces the occurence of recombination[25,26] Photocatalytic supports doped with co-catalysts have their activity largely defined by their work function, ϕ, which is the energy required to promote an electron from the Fermi level to a vacuum. At the interface, electrons flow towards the component with the higher work function (ϕ). So if the work function of the metal is higher than the semiconductor, electrons flow into the metal until Fermi levels of the semiconductor and metal are equalized. This removes free charge carriers from the surface of the semiconductor, creating a space charge region.[27]

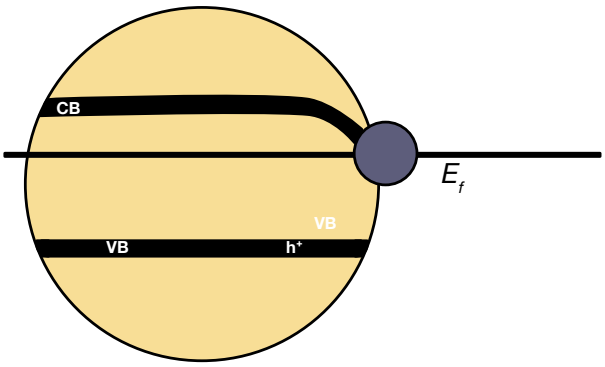

Figure 1.11: Band bending in a semiconductor-cocatalyst interface where the photocatalyst has a higher work function than the semiconductor.

Band bending influences the rate of electron-hole recombination, thereby influencing quantum efficiency. The electric field generated at the interface of semiconductors and metal nanoparticles facilitates physical separation between electron and hole, reducing recombination rate.

The direction of band bending can influence the availability of electrons and holes at the surface for photocatalytic reactions. If bands bend down towards the surface, photoelectrons are more available at the surface for reactions, whereas upwards band bending creates more available hole species at the surface. So if the catalyst is intended to reduce a species (such a protons to H_2 half reaction), then a co-catalyst with a high work

function is desired such as Pt.

The positions of valence bands with respect to the redox potentials of desired half reactions are the most important factor in photocatalytic support, but activity is also defined by charge separation, one of the biggest challenges in photocatalyis. Charge separation refers to the separation of photoelectron and hole after light absorption, and the inhibition of their recombination into their original states with no enhanced redox activity. Co-catalysts are a tool used to tackle charge separation, by introducing physical distance, and Schottky barriers to reduce recombination.[22,28] Aside from reducing recombination, co-catalysts still contribute a role to the catalytic cycle.

Schottky Barrier Height (SBH) is the measure of mismatch of the energy levels for a majority of carriers across the metal-semiconductor interface. SBH controls electronic transport across the interface and dictates semiconducting behaviour. Preparation of the metal-semiconductor interface has an effect on SBH beyond just the work function of the metal, however higher work function metals are generally much higher SBHs than those with lower work functions.[29]

1.1.6 Hydrogen in green chemistry

The depleting petroleum reserves, and global warming from CO_2 emissions from hydrocarbon combustion are cause for a reform of our current energy sources, prompting a search for alternative energy sources and fuels. Hydrogen is one of the most promising candidates as an energy carrier, benfitting from a relative ease of storage compared to electrical energy. The only product of hydrogen combustion is water, which is ecologically and environmentally benign, removing fossil fuel emissions and reducing problematic particulate emissions in highly populated areas. Also, water can be used as the starting material for hydrogen generation in a 'water splitting' reaction, producing a circular economy for fuel production. Hydrogen also beneftis from high energy density, producing 122 kJg^{-1} , which is much higher than gasoline at 40 kJg^{-1}.[21]

Although hydrogen is sustainable as a fuel, acting as an energy carrier, the methods to obtain it are important to critically evalute hydrogen as a fuel source. Creating hydrogen is energy intensive $\Delta G = +237$ $kJmol^{-1}$, therefore if the production methods are carbon-emitting from

fossil fuel relience then the resulting hydrogen is not a sustainable fuel. The ultimate goal is to produce hydrogen from water through clean energy sources such as renewable electrical energy or sunlight, as shown in equation (1.1).[30]

$$2\,H_2O \longrightarrow 2\,H_2 + O_2 \tag{1.1}$$

With $\Delta G = +237$ kJmol^{-1}, from a single photon, the minimum energy required to induce water splitting is 1.240 eV. The wavelength equivalent to this is approximately 1000 nm, therefore any photon with $\lambda \leq 1000$ nm could induce a water splitting reaction.

Currently, hydrogen is primarily produced most commonly through steam reforming at 700-800 °C at elevated pressures and occurs through 3 reactions:[31]

$$CH_4 + H_2O \rightleftharpoons CO + 3H_2 \Delta_{298}\text{=}206\text{kJ/mol} \tag{1.2}$$

$$CH_4 + 2\,H_2O \rightleftharpoons CO_2 + 4H_2 \Delta_{298}\text{=}164.9\text{kJ/mol} \tag{1.3}$$

$$CO + H_2O \rightleftharpoons CO_2 + H_2 \Delta_{298}\text{=}-41\text{kJ/mol} \tag{1.4}$$

Steam reforming uses methane as a starting material, which is a potential energy source, and produces the greenhouse gas CO_2 as a side product, thus hydrogen produced through stream reforming leaves room for improvement regarding sustainability. Other current industrial processes for hydrogen generation electrolysis, oil-based production and coal gasification, none of which are environmentally benign enough to drive a 'hydrogen economy' of fuel, due to their reliance on fossil fuels for raw materials or energy.[32]

To achieve the most environmentally benign hydrogen, production harnessing the energy of sunlight would be the ideal to overcome the large enthalpy of formation. This can be achieved through solar energy capture (photocatalysis) or electricity through renewable energy sources.

The challenge of hydrogen as an energy carrier is logistical. High pressure cylinders are heavy and thus inefficient for fuel consumption in transport, with the significant dangers regarding hydrogen as a highly flammable gas. Liquid hydrogen is also inefficient, due to the energy costs associated with its liquification. To meet the standards set by

petroleum in transport vehicles, volumetric and gravimetric energy densities require large improvements over these choices. A popular approach to this issue is through use of an intermediate for energy storage, such as hydrides or ammonia.[33] Ammonia is a promising intermediate, allowing for a circular economy, with catalytic steps in the hydrogen generation, ammonia synthesis and decomposition, displayed in Fig. 1.12. Ammonia has a higher volumetric energy density (12.92-14.4 MJL^{-1}) than even liquid hydrogen, when ammonia is liquified at 10 bar and ambient temperature. For comparison, lithium-ion batteries have volumetric energy density in the range of 0.9 - 2.63 MJL^{-1}.[34]

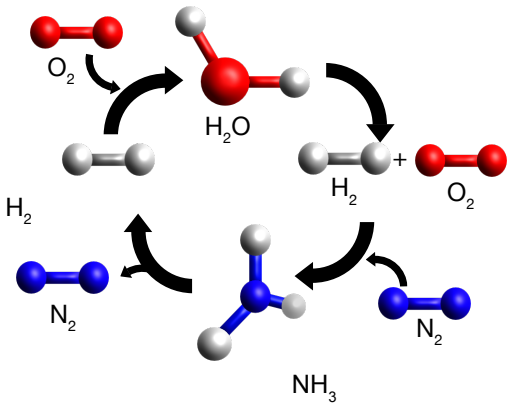

Figure 1.12: The circular economy of ammonia energy carriers, which is a potential improvement on the logistics of hydrogen energy carriers, due to the higher energy density

1.1.7 Photocatalytic hydrogen generation

Hydrogen generation from water requires a large energy input, $\Delta_G = +237$ $kJmol^{-1}$ therefore the potential for hydrogen as a sustainable fuel source relies upon clean energy sources for its production, such as renewable electric energy or sunlight.[30]

Hydrogen generation is distinct from the previously discussed 'water splitting reaction'. The difference between the reactions is that hydrogen evolution utilises sacrificial electron donors, commonly organics such as triethanolamine or methanol, with oxidation half-reaction (1.10) and water splitting oxidises water at the anode with half reaction (1.6) . Electron donors are chosen for their oxidation potentials, where they are less positive than water, allowing for faster hole scavenging and thus reducing the potential for recombination.[28] The products of hydrogen evolution

oxidation half reactions are more easily oxidised than methanol, therefore half reaction (1.7) is also observed when using methanol electron donors. The hydrogen evolution reaction (HER) at the cathode is identical in both (1.8) Although electron donors are an additional cost, they increase activity by reducing photoelectron-hole separation and provide the opportunity to treat waste-waster simultaneously producing hydrogen due to the wide variety of potential electron donors[22]

$$CH_3OH_{(aq)} \longrightarrow HCHO_{(aq)} + 2\,H^+(aq) \tag{1.5}$$

$$H_2O_{(l)} \longrightarrow \frac{1}{2}O_{2(g)} + H_{2(g)} \tag{1.6}$$

$$HCHO_{(aq)} + H_2O_{(l)} \longrightarrow CO_{2(g)} + 4\,H^+(aq) \tag{1.7}$$

$$2\,H^+(aq) \longrightarrow H_{2(aq)} \tag{1.8}$$

Photocatalytic hydrogen generation has the potential to harness either renewable electric energy or sunlight for the energy source, in the form of light. The current method for hydrogen production is primarily steam reforming, which relies on petroleum starting materials beng processed at temperatures above 650 °C and elevated pressures.

Photocatalytic hydrogen generation was first discovered in 1972, using a TiO_2 photocatalyst, revealing the potential for semiconductors in photocatalysis[35]. Since the discovery of the efficacy of TiO_2, d^0 metals and semiconductors containing these metals have become some of the most popular systems for hydrogen generation; examples include Zr(IV) and W(VI).[3637]

Support materials in photocatalytic hydrogen generation are desired to possess a more negative conduction band than the potential for hydrogen reduction (H^+ / H_2 = -0.41 V vs NHE) and a more positive valence band than that of the oxidation potential of water (H_2O/O_2 = 0.82 V).[38]

TiO_2 is an ideal material for photocatalytic hydrogen generation, as the band gap is well suited, with UV absorption for excitation of electrons into the conduction band and good stability with respect to UV and visible light irradiation. Not only is it well suited to the task, but also is readily available and very cheap. TiO_2 is the most well studied chemical for this reaction, and is the state-of-the-art when paired with Pt co-catalysts.

Many materials are deposited with additional electron accepting co-catalyst metals to increase their ability to generate hydrogen through photocatalysis, with the most effective co-catalyst being platinum. The increased reactivity with addition of co-catalyst can be attributed to the increased separation of photoelectron and hole after excitation[39]. Increased separation of photoelectron and associated hole decreases the likelihood of recombination, which reduces the photonic yield, losing excited electrons and producing heat or photons.[24]Therefore, increasing the separation also increases the likelihood of a photoelectron's successful reaction to generate hydrogen.

Sacrificial reagents, such as methanol or triethanolamine are used in photocatalytic hydrogen production to maintain photoelectron-hole separation.[28]

$$\mathrm{H_2O_{(l)}} + 2\,\mathrm{h^+_{(VB)}} \longrightarrow \frac{1}{2}\mathrm{O_{2(g)}} + 2\,\mathrm{H^+}(1) \tag{1.9}$$

$$2\,\mathrm{H^+} + 2\,\mathrm{e^-_{(CB)}} \longrightarrow \mathrm{H_{2(g)}} \tag{1.10}$$

Platinum is the most commonly used co-catalyst for photocatalytic hydrogen generation by far. It creates effective schottky junctions by acting as an electron trap, and is the active site for proton adsorption and reduction. Pt is a particularly effective catalyst in this reaction, as it has the largest work function of the noble metals.[40] Increased work functions have been correlated experimentally with increased activity in catalysing the proton reduction half reaction (Eq. (1.8)).[41] This is because a lower volatage (or photon energy) is required to activate the surface catalyst with an electron, as excited electrons have a higher probability of tunelling[42] .

1.2 Metal organic frameworks

1.2.1 Introduction to Metal-organic frameworks

Metal-organic frameworks (MOFs) are a class of crystalline materials consisting of metal atoms, or metal-based inorganic clusters referred to as secondary building units (SBUs), and organic linkers. The linkers, by necessity require 2 or more co-ordinating groups to create an extended

network of co-ordination, therefore MOFs are a subset of co-ordination polymers.[43] MOFs are differentiated from other co-ordination polymers by their building blocks being specifically organic (commonly defined by the presence of a C-H bond), compared to another linker such as thiocyanate, and the presence of pores within a MOF. To maintain macrostructure and porosity, many MOFs utilise dicarboxylate linkers which form strong bonds to hard acid metals. MOFs are extremely diverse, with over 100,000 known structures[44] . This wide variety of structures has led to much research attention, allowing for precise tuning of functional groups and metals for a specific application. They have been applied to a wide array of applications, such as gas separation and capture, water harvesting, catalysis, drug delivery, contrast agents, and sensing.

Nomenclature of MOFs follows a letter sequence (generally corresponding to acronyms associated with the insitute of MOFs discovery), followed by numbers (corresponding to the iteration of MOF or synthesis within a series), e.g. (UiO-66). Some of the most common MOFs, for example are: UiO = Universitet i Oslo, MIL= Materials of Institute Lavoisier.[45] [46] However this naming convention is not always the case, with materials containing structural descriptor acronyms such as ZIF = Zeolitic Imidazole framework or PCN = Porous co-ordination network, or the eponymous 'MOF' series, which stands for Metal organic framework (aswell as the type of material, as this was named before it was accepted to associate a MOF with its instituion of discovery).[47,48]

1.2.2 Metal-organic framework syntheses

While the variety in MOF synthesis has increased in recent years, the archetypal MOF synthesis utilises temperatures in the range of 100-200 °C inside a sealed vessel (teflon-lined autoclaves at high temperatures or other vessels leading to autogeneous pressure), without stirring. This synthesis technique is commonly used for many reasons: it is (relatively) easy to replicate, slow cooling allows longer crystallisation times (thus larger crystallites), and it enables high throughput in parallel to explore the many variables in a MOF synthesis.

Of the conventional MOF syntheses, there are two categories, solvothermal and non-solvothermal. Solvothermal syntheses are those in which

the solvent is heated above its boiling point, generating autogeneous pressure within the sealed container. Non-solvothermal syntheses are at temperatures below the boiling point of the solvent. Hydrothermal syntheses are also commonly used, which are solvothermal syntheses where the solvent is water.[49]

Modulators have become close to ubiquitous in MOF synthesis, particularly in the UiO-66 family or any syntheses with defect control in mind. These components of a reaction mixture contribute a controlled rate of reaction by competitively inhibing metal-linker co-ordination, forming labile co-ordination bonds. Generally modulators are mono-carboxylic acids, such as formic or acetic acid for their conjugate Lewis-base character, but other conjugate bases such as Cl^- have been reported.[50][51] By reducing the rate of reaction between metal nodes and linkers, crystallisation is slower, therefore larger crystallites can be obtained (Fig. 1.13).[52] These modulator species have also been applied to promote defect formation, which is discussed in the sub-chapter *Defects in UiO-66*.

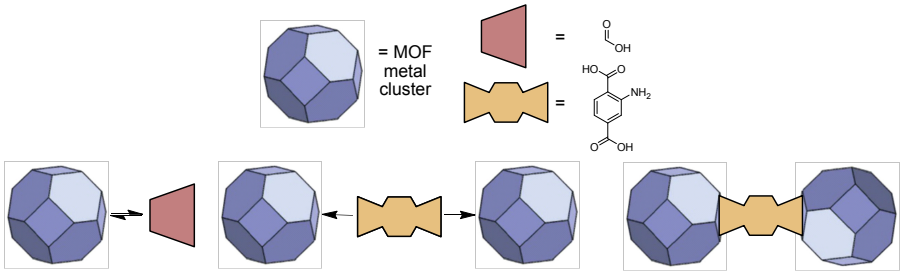

Figure 1.13: Formic acid modulator competitively inhibiting node-linker bond formation.

Some MOFs are notoriously difficult to synthesise replicably, as shown by an interlaboratory study.[53] Figure 1.14 exemplifies this difficulty with the powder diffraction patterns of 8 independent laboratories following the same synthetic instructions for 2 separate MOFs, (a) PCN-222 and (b) PCN-224.[53] These diffraction patterns show that the same instructions yielded different phases or mixtures thereof from each laboratory and, in these 16 syntheses, only 3 match that of the intended products (despite the syntheses being reported to produce them prior to the study).

The difficuly in replicability of MOF synthesis is, in-part, due to the number of parameters MOF chemists wish to control. We have interest in controlling surface area, defects and crystallite size, to name a few, and all of these parameters are second priority to the phase and purity thereof. These parameters are intertwined by their independent

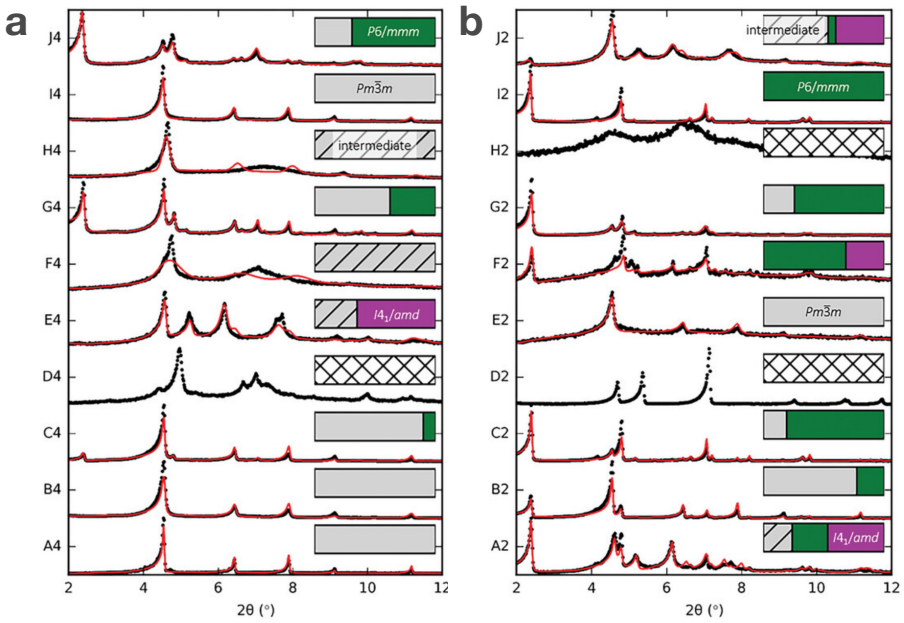

Figure 1.14: Powder X-ray diffraction patterns of the products of 8 independent laboratories (labelled A-J) following the same synthetic procedures for PCN-224 (a) and PCN-222 (b)PCN-224. Reproduced from [53]

variables. For example, adding modulator could feasibly increase crystallite size and simultaneously introduce defects (which are documented to have profound effects on surface area).[54]

The list of independent variables which can effect physical and chemical properties of the MOF is extensive. There are the more obvious, such as: solvent and modulator selection, metal anions, synthesis temperature, which are of course not the source of difficulty in synthesis. Other factors, which are more problematic for reproducibility are: reaction pressure (linked to reactor headspace), moisture content (which can be linked to laboratory humidity if not otherwise controlled)[53], mixing methods (if any), crystallisation time and crystallisation rate. Some of these parameters are those which would typically be excluded from a methods section, although as this synthetic difficulty becomes acknowledged more widely, methodological sections are becoming more exhaustive in response.[53]

During the synthesis of MOFs containing $Zr_6O_4(OH)_4$ nodes, such as UiO-66, NU-1000 or MOF-808, it has been established that the first stage of synthesis is the formation of $Zr_6O_4(OH)_4$ nodes.[55,56] This stage of formation gives potential for water content in a reaction to control physical properties, such as phase or defect concentration, as the commonly used Zr reagents $ZrCl_4$ or $ZrOCl_2$ require oxygen sources for clus-

ter formation. The ability for water to control the phase of UiO-66 was shown by Firth et al, synthesising the previously unreported **hcp** phase through this technique.[51]

1.2.3 Defects

In solid state chemistry, introducing defects is a useful tool to adjust the properties of a material. Over time, synthetic methods and post-synthetic procedures have been adapted to precisely control the structure and composition of materials to harness this tool. Defects have been introduced and characterised in many forms, although this thesis focuses on point defects (Fig. 1.15).

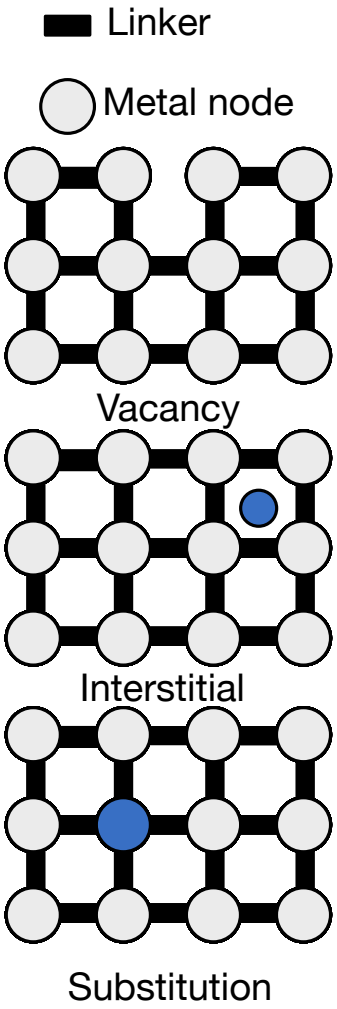

Figure 1.15: The three types of point defect in the context of a metal-organic framework: Vacancy corresponds to a missing component, such as a linker. Intersitials are atoms placed between the symmetric positions of atoms within a crystal, or between layers. Subsitutions are atoms which have been replaced in the structure by an another atom.

Point defects are local sites in which the regular crystal structure is

changed at a given point in the structure. These defects are not necessarily recurring, nor ordered, however a point defect can extend for a few atomic distances. Because of their 'random' distribution, they are difficult to investigate and characterise using most techniques (such as X-ray diffraction) which characterise the average structure throughout a crystal. Their effect on the average structure is possible to observe in high concentrations, where a relaxing effect can be observed, potentially giving rise to small changes in lattice parameters, or through local structure probing in the pair distribution function where diffuse diffraction features are considered.[57,58]

Point defects are entropically favoured to form, to some extent, as their introduction to a perfect crystal increases the possible configurations. The configuational energy is given by equation (1.11).[59]

$$S = k \ln W \tag{1.11}$$

Where k is Boltzmann's constant, and W is the number of arrangements of point defects. Vacancy defects are simple in elemental solids, where an atom will be missing from the lattice. In ionic compounds, these defects are more complicated, as charge neutrality must be maintained in the lattice, therefore a Frenkel or Schottky defect will be observed, compensating for the charge of the vacancy. Schottky defects occur as cation vacancies, where anion vacancies of sufficient stoichiometry to compensate for the charge of the missing cation will be introduced. For example, in an NaCl crystal structure, one Na^+ vacancy would produce one Cl^- vacancy; whereas in $MgCl_2$, an $Mg_2{}^+$ vacancy would produce two Cl^- vacancies.

Point defects can form aggregates in different ways. In an elemental solid, two vacancies will be favoured adjacent to one another, as the number of bonds required to be broken in forming of a vacancy will be lower, thus the internal energy is lower for a region with two adjacent vacancies than two separated vacancies.[59] Alternatively, in a Frenkel defect, interior atoms can jump into interstitial positions adjacent to a vacancy for local charge balancing, creating an interstitial defect adjacent to a vacancy.

In Schottky defects, formal charges are associated with each vacancy, negative for vacant cations and positive for vacant anions. Because of the charges associated with these vacancies, their attractions can lead

to vacancy clustering, where the defects become more concentrated over specific regions.[60]

1.2.4 UiO-66

UiO-66 is one of the most well researched MOFs to date. The material is composed of $Zr_6O_4(OH)_4$ and 1,4-benzene dicarboxylate (BDC) in an fcc structure, with the space group $Fm\bar{3}m$.[61] Isoreticular structures are also possible by functionalising the ligands with groups such as: CH_3, NH_2, and NO_2 The nodes are composed of $Zr_6O_4(OH)_4$, with Zr(Hf, Ce or even U) atoms forming an octahedron. Each point in the octahedron is linked to its adjacent Zr atoms by bridging oxide and hydroxide anions in a 1:1 ratio.[46,55,62]

A large contributor to the popularity of UiO-66 is its high stability, displaying good stability (relative to other MOFs) with respect to acidity, nucleophiles, electrophiles and oxidants, although its structure is susceptible to change or decay through reaction with bases or reductants.[63] Zr(IV) is highly charged and not very polarisable, making it a hard Lewis acid. Terephthalate ligands are hard Lewis bases, creating very strong co-ordinating interactions between Zr-BDC.[64] This strong bond is generally only susceptible to breaking by hard Lewis bases, such as F^-, PO_4^{3-} and OH^-. Thermal stability in air allows this material to withstand temperatures up to ~300 °C, though the stability is affected the synthetic conditions.[54]

1.2.5 Defects in UiO-66

Defect chemistry in UiO-66 is rich, with a variety of defect types and a capacity to accomodate defects in large concentrations while maintaining stability. There have been many publications characterising UiO-66 defect types, and elucidating the chemical and physical environments resulting from defect generation.[54,65–68] Defects in UiO-66 are most commonly vacancies, with linker vacancies the most prevalent (Fig. 1.16c), and missing clusters are observed in the nano **reo** phase (Fig. 1.16 d,e).[68] The interesting phase chemistry of UiO-66 can also be noted alongside defects, as the phase changes introduce new chemistry at points of the crystal in a similar manner, for example the **hcp** phase, displaying the

'double cluster' motif.[51]

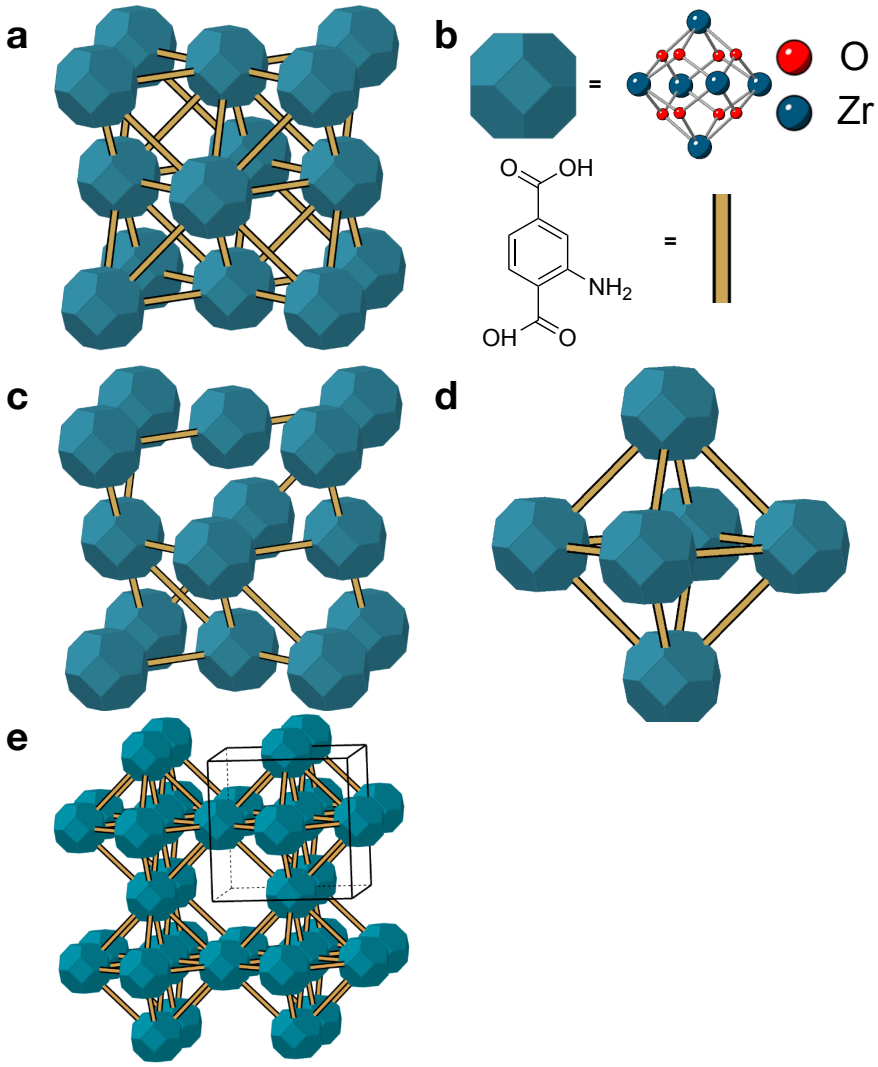

Figure 1.16: (**a**) The crystal structure of defect free **fcu** UiO-66. (**b**) The strucutre of UiO-66 secondary building units (cluster and linker). (**c**) Randomly distributed missing linker defects from the **fcu** crystal structure. (**d**)The crystal structure of **reo** UiO-66, a correlated defective primitive structure observed in nanoregions, rather than a phase-pure sample (**e**) A 2x2 supercell of **reo** UiO-66, showing the channels created through ordered missing linkers.

The most common technique to incorporate defects into UiO-66 is through a modulated synthesis. These modulators are mono-carboxylic acids, which are understood to compete with linkers for Zr co-ordination sites. While a modulator occupies a Zr site, the crystal will form around this occupied site, eventually forming the framework with linker vacancies. Remaining monocarboxylate or solvent which is co-ordinated to these 'open' Zr sites at defects can be driven off with heat during the activation process.[69] A schematic is included in Fig.1.17

Both missing linker and missing cluster defects have been imaged using

high resolution transmission electron microscopy in extraordinary detail, allowing visualization of individual defects.[70] The images of defect-free, missing linker and missing cluster defects have been reproduced in Fig. 1.18 (a),(b), and (c) respectively.

Missing clusters require more precise synthetic conditions to achieve than missing linker defects. High concentrations of formic acid modulator have been shown as a key factor in the creation of this defect type. These defects have been observed to be more prevalent in longer duration syntheses, which shows that the formation of Zr-BDC bonds are reversible in the correct conditions, and the defects are expected to form as a result of ligand displacement by formate ions, as per equation (1.12).[68]

Missing cluster defects through **reo** UiO-66 nanodomains can be detected through diffuse reflectance in the *100* and *110* peaks in a powder diffraction pattern. These peaks are symmetry forbidden, but observed due to primitive nanodomains present within the structure as confirmed by X-ray pair distribution funtion (XPDF) analysis.

$$[\mathrm{HfO_4(OH)_4}][\mathrm{C_6H_4(COO)_2}]_{12/2} + x[\mathrm{HCOO}]^- \rightleftharpoons$$
$$[\mathrm{Hf_6O_4(OH)_4}]_4[\mathrm{HCOO}]x[\mathrm{C_6H_4(COO)_2}]_{\frac{12-x}{2}} + \frac{x}{2}[\mathrm{C_6H_4(COO)_2}]^{2-} \tag{1.12}$$

This thesis focuses on creating and utilising missing linker defects in heterogeneous catalyst support materials, as these defects provide beneficial chemical and physical traits to the support material. At a given under coordinated note adjacent to a linker vacancy, charge balancing occurs co-ordination of one hydroxide ion. Another co-ordination site is available after charge balancing, where a water molecule (when present) which will physisorb at Zr adjacent to the hydroxide co-ordination. Be-

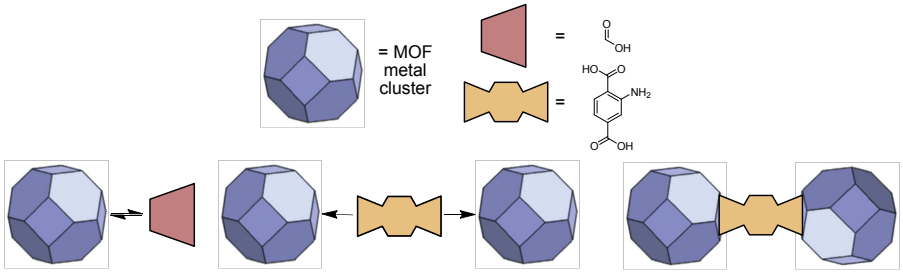

Figure 1.17: The effect of modulators within a MOF synthesis

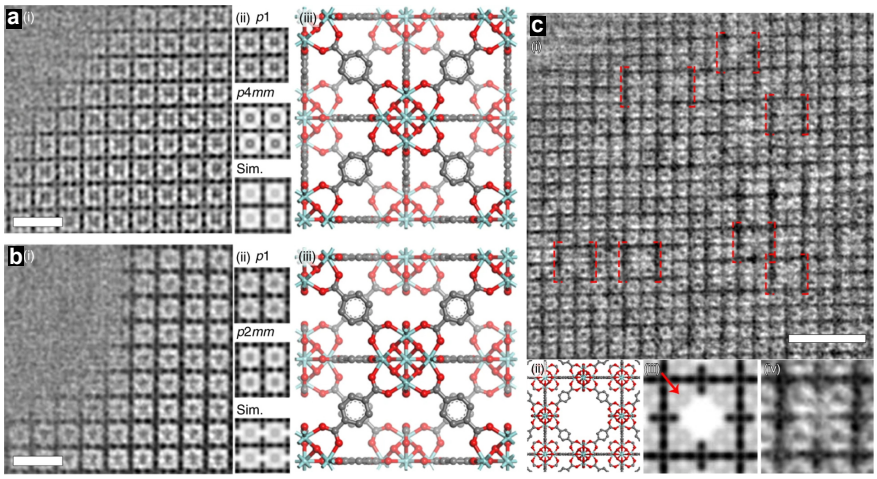

Figure 1.18: Contrast transfer (CTF) correction HRTEM images and structural models of: (**a**) The [001] plane of **fcu** UiO-66.(**b**) Missing linker defects in UiO-66. (**c**)A missing linker defect in the **reo** structure. In each set of images: (i) is CTF corrected HRTEM images ,scale bar = 2 nm in (a,b) and 5 nm in (c).(ii) is projected structural models along the axis of respective HRTEM images (iii) is simulated projected potential map of respective HRTEM images (iv) is experimental images of the respective features of interest (processed by real space averaging to enhance signal-to-noise ratio. Reproduced from [70].

tween this OH^- and H_2O, rapid proton exchange is observed.[66]

Missing linker defects have been shown to tune the electronic structure of UiO-66, by allowing for μ_2-OH to be deprotonated, relaxing the node and inducing shorter Zr-O bond lengths and reducing the energy required for electron excitation within the ligand chromophore, a highly beneficial effect for photocatalytic applications.[67]

Missing linkers also give rise to the possibility for tuning either Lewis or Brønsted acidity, which is controlled through hydration. Undercoordinated Zr sites can be capped by oxygen from water, creating highly labile δ^+ H atoms, allowing Brønsted acidity. Missing linker defects have also shown to make UiO-66 more hydrophillic, and Brønsted acidic(an effect observed even more strongly in UiO-66(NH_2)).[71] If water is not present at the surface of the MOF, these undercoordinated Zr sites act as Lewis acids.

Missing linker defects are measured through thermogravimetric analysis, where weight loss during thermal decomposition of the framework is lower than that expected from the 'pristine' MOF. The presence of these defects has also been confirmed through neutron diffraction.[72] These defects cannot be observed through powder X-ray diffraction, as they are randomly distributed and do not effect symmetry or lattice parameters

(of an observable magnitude), and the X-ray atomic scattering factors of the atoms in the organic ligands are small compared to the Zr atoms, thus ligand occupancy cannot be measured.

Defects can affect the stability of their respective crystal structures, and UiO-66 is no exception. This framework, however, has shown the ability to sustain huge amounts of defects, while maintaining the crystal structure and good thermal stability. The framework is capable of withstanding up to ~36 % missing linker defects before experiencing collapse[73]. The reason for this stability lies partly in the strong Zr-O co-ordination bonds mentioned in the previous section, and partly due to the highly connected nature of the crystal structure. The nodes in UiO-66 are 12-connected, thus each is co-ordinated strongly to 6 ligands. This co-ordination network allows for the framework to stay connected with a large amount of missing linkers, and the 2 strong bonds at each ligand prevent collapse from any defect-induced crystal strain.

Defects can also be generated using post-synthetic techniques, such as plasma cleaning or solvent assisted-ligand exchange (SALE).[74] Plasma cleaning can produce defects by bombarding the as-synthesised MOF with high energy Ar^+ (although this can be other gases), whereas SALE utilises high concentrations of functionalised ligands to exchange with those present.[75]

1.2.6 Post-synthetic defect generation

Examples in literature show gases such as O_2, CF_4, C_2F_6 plasmas, however this research only focuses on the utilization of Ar plasma. Ar plasma is chosen here as I identify a route to create defects in an inert atmosphere, and deposit co-catalyst metals in the same chamber under the same gas. This combination of Ar plasma defect engineering and co-catalyst sputtering provides a facile, fast route to modify and tune a support material very precisely.

Ions of a higher mass, such as O_2^+ and CF_4^+ have higher momentum at the moment of incidence upon the MOF, therefore transfer more energy to the MOF and create larger defects. Ar^+ typically only induces a point defect ejecting a few atoms. Figure shows SEM micrographs of pristine anatse on the left, and N_2 plasma treated on the right, with ~1 $/mu$m pores. Figure shows SEM images of as-synthesised UiO-66

on the left, and after 30 minutes of Ar plasma treatment. After Ar plasma treatment, the surface is clearly rougher, however the large pores observed from N_2 plasma treatment are not present. Molecules such as O_2, which are capable of chemically reacting as well as providing ion bombardment are established to induce chemical functionality through reactions after the bombardment.

Ar plasma was used by Xiang *et al.* to introduce missing linker defect into UiO-66, enhancing the activity towards CO_2 cycloaddition. In this research, exposure to plasma reduced the intensity of PXRD peaks with time exposed. No fitting was performed to assess peak broadening or other features changing as the material is exposed. The MOFs developed a yellow tinge with plasma exposure, which can be attributed to missing linker defects changing the band structure and increasing the light absorption in the visible region. These optical property changes are also seen in the Tauc plots, where the calculated band gap decreases with plasma exposure.

1.2.7 Metal-organic framework catalysts

MOFs have proven effective and catalysts for a variety of applications. The main attraction for use of a MOF catalyst is the degree of tunability available, with synthetic conditions able to control functionality, metal centres, topology, surface area, and defect concentration. All of these attributes give rise to variations in the catalytic performance, which allow for very tightly controlled properties, otherwise unavailable in classical support materials such as metal oxides. The porous network also allows for a larger amount of open catalytic sites which are accessible to reactants beneath the surface.

Incorportaing catalytic metals into the framework structure is a common method for creating MOF catalysts, using metals such as Cu and Ni. This can be achieved by using them as a structural component of the framework,[76] where the metal nodes act as active sites for reactions. Another common approach is to incorporate catalytic metals into the framework through co-ordination, which is prevalent in porphyrin MOFs, where the centre of the porphyrin ring facilitates catalyst atom co-ordination. This is particularly useful in photocatalysis, where a catalyst metal is immobilisied directly adjacent to a strongly absorbing

chromophore

Metal-organic frameworks have much lower stability than traditional support materials, with 'stable' MOFs such as ZIF-8 and UiO-66 degrading at relatively low temperatures (300 °C).[77] This stability makes these support materials limited in their applications to thermal catalysis at high temperatures, such as cracking of hydrocarbons. To avoid the thermal stability issues of MOF catalysts, their investigation in photocatalysis has increased greatly. The targetted, specific energy input in photocatalysis allows for the activation energy of a reaction to be met, while avoiding the non-specific energy of high temperatures which can lead to framework breakdown and organic component oxidation.

As a particularly stable MOF, UiO-66 has been implemented in many catalysts. The hydroxylated $Zr_6O_4(OH_4)$ clusters at missing linker defects allow for Brønsted acidity and, when heated in anhydrous conditions, these hydroxides are removed, leaving co-ordination vacancies at Zr atoms, allowing Lewis acidity.[78] This is shown in Fig. 1.19 (reproduced from ref.[78]). UiO-66 provides great evidence for the tunability of MOFs. The 1,4- benzene dicarboxylate linkers can be substituted for functionalised linkers, containing amines or nitro groups to improve visible light absorption and thus photocatalytic activity under visible radiation. UiO-66 MOFs with functionalised linkers are isoreticular to one-another and UiO-66, therefore this tuning provides very effective control over optical properties, while minimising unwanted effects to catalytic performance.

Missing linker defects are well documented to increase the activity of UiO-66 catalysts across many reactions, such as carbon dioxide cycloaddition, photocatalytic hydrogen generation, cyclisations, esterifications and many more.[73,75,79] There are no reported instances (to my knowledge or that of the extensive review in ref.[75]) of defects reducing catalytic activity not caused by collapse of the framework structure. Missing linker defects are reported to increase catalytic activity through surface area increase, enhanced visible light absorption and exposed Brønsted and Lewis acidic sites.[75,78,80]

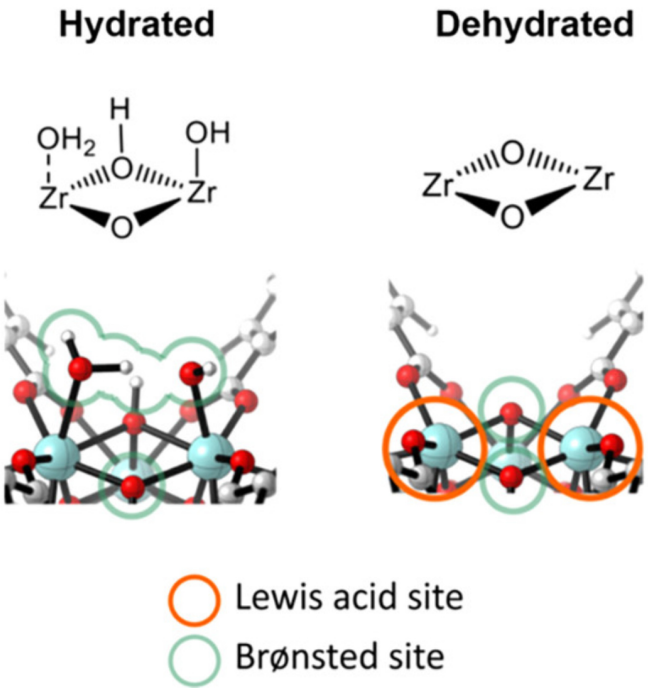

Figure 1.19: Left: A hydrated zirconium-oxo cluster adjacent to a missing linker defect with Brønsted acidity at the hydroxides. Right: The dehydrated cluster with Brønsted acidity at the undercoordinated Zr atoms. Reproduced from reference [75]

TEM is the most commonly used technique to analyse the particle size of co-catalysts deposited on MOF, as the micrographs are very useful to measure particles directly, while simultaneously giving information on co-catalyst particle distribution.[81–83] XPDF can also be a useful technique for determining the structure of deposited metal clusters(not always in the field of catalysis), by probing the local structure.[84] The ability of PDF to decipher precise interactions between MOF and metal particles has been shown in metal adsorption, during synthesis and in catalysis[85–87].

The most extenisve publication probing the structure of catalyst nanoparticles upon a MOF using PDF is by Platero-Prats *et al.*, where NU-1000 was deposited with NiO_xH_y by ALD.[88] The deposited nickel species was shown to develop one-dimensional nanowires, as elucidated by PDF, EXAFS, XRD and computational modelling. This case shows very specific catalyst structure, which is not always expected, particularly with larger catalyst loadings inducing nanoparticle formation.

Newton et al report in-situ XPDF analysis of Pt @ Al_2O_3 during CO oxidation, probing the changing structure of nanoparticles.[89] By measuring XPDF of Al_2O_3 with and without Pt, subtraction of the support material's PDF yields only Pt-related correlations. This was referred to as a differential PDF (d-PDF). d-PDF allows resolution of only Pt correlations, despite there being only 1 wt% Pt in the sample. In situ PDF observes changes in Pt-Pt nearest distance decreases when exposed to oxidising conditions, and an additional correlation is observed at 3.3 Å. Both observations are reversible and repeatable on the same sample. The d-PDF shows no changes in the local-structure of Pt beyond 3.3 Å, and the fcc Pt structure is retained, indicating that the core of the nanoparticle remains unchanged, and short-range structural changes are at the surface.

Further analysis was conducted, subtracting PDF of Pt @ Al_2O_3 (under oxidising conditions) from PDF of Pt @ Al_2O_3 to obtain a "surface" d-PDF. This subtraction reveals several additional features at 2.0, 2.6, 3.3 and 4.4 Å, attributed to a PtO AB-stacked phase. This publication highlights the power of PDF to measure extremely dilute phases of nanoparticles on a support material, even deconvolving the surface and sub-surface nanoparticle correlations. No nanoparticle-support interac-

tions were observed, indicating that there is no uniform binding motif for Pt NPs @ Al_2O_3

Chupas *et al.* report another example of d-PDF for nanoparticle structure elucidation in Pt @ TiO_2.[90] Authors used TiO_2 subtractions to obtain d-PDF of Pt - related correlations. Measurements were taken at a dedicated XPDF beamline 11-ID-,B with high energy X-rays (0.2128 Å). Even with a state-of-the-art experimental setup, highly experienced experimentalists and a stable support material, d-PDFs still show residual peaks related to support material and non-flat baselines. This shows that d-PDFs are not always perfect subtractions, even in ideal conditions. It is important to note each component in these d-PDFs and account for unexpected features by first considering how they could be introduced by incorrect subtractions. Authors were able to observe Pt-Cl correlations decreasing as the Pt species was reduced into nanoparticles, and Pt-Pt and Pt-Cl correlations are observed at the same time. The use of short scans in-situ is able to deconvolve Pt and support correlations, in weight loadings at low at 2.5 wt%. d-XPDF is easier when NPs are strongly X-ray scattering, such as Pt, and when the support material is a weaker X-ray scatterer.

PDF analysis of nanoparticles can be assisted by modelling, such as through attenuated crystal (AC) approximation.[91] Building nanoparticle models, and processing the data through highly constrained refinements allows the researcher to account for physical parameters relating to a nanoparticle's shape and size. This approach is useful for 'simple' nanoparticles , such as those with few defects, which are phase-pure and are homogeneous from core to shell. Supported catalyst nanoparticles rarely fit these specifications, particularly when there is a strong interaction with the support material therefore a 'bulk' model from a crystallographic information file describes the nanoparticle approximately as accurately as a modelled nanoparticle, and relevant physical parameters can still be refined in fitting software such as Topas Academic.

The relative merits for both TEM and XPDF for structural analysis of nanoparticles deposited onto MOF supports are different. TEM provides information on nanoparticle sizes, the size distribution and the nanoparticle distribution about the MOF, allowing us to 'see' the nanoparticles.

XPDF is a bulk technique, and measures all of the material present, revealing NP interactions with the MOF, showing atoms deep beneath

the MOF surface which are not visible by TEM, and taking into account inhomogeneity regarding nanoparticle distribution. Despite the different merits, these techniques are not commonly used synergistically for nanocatalysts deposited onto MOFs, which leaves some information 'on the table'. This thesis aims to highlight the benefits of using both XPDF and TEM synergistically, providing an in-depth view of how nanocatalysts interact with defect 'anchor sites' in UiO-66(NH_2). Large amounts of effort have been dedicated to elucidating the structure of defects in UiO-66 structures, for the interesting chemistry that occurs at defect sites.[65,66] Despite numerous publications investigating co-catalysts (commonly platinum) @ defective UiO-66 and UiO-66(NH_2), the interaction of metal nanoparticles and defect sites is still not well understood.[81,83,92] Only TEM has been used to probe the physical properties of nanocatalysts deposited onto UiO type MOFs. This thesis presents the most in-depth analysis of Pt @ UiO-66(NH_2), analysing the structure and chemical environments of Pt NPs on different defect concentrations of UiO-66(NH_2), with an aim to elucidate the interface between NPs and support materials.

1.3 Characterisation techniques

1.3.1 X-ray Diffraction

X-rays are electromagentic radiation with their wavelength, λ, typically of the order of 1 $\times 10^{-10}$ m. Their use in materials science and solid state chemistry is ubiquitous for diffraction applications amongst many other techniques. λ and direction of an X-ray can be described by the wave vector $\mathbf{k}$. This is a vector in the direction of the X-ray, with a magnitude of:

$$|\mathbf{k}| = \frac{2\,\pi}{\lambda}\,. \tag{1.13}$$

An X-ray wave is more precisely expressed according to its angle and magnitude according to (1.14):

$$\psi = A\exp(i\mathbf{k}\cdot\mathbf{x}) \tag{1.14}$$

Where $\mathbf{x}$ is a position in space, and $\mathbf{k}\cdot\mathbf{x}$ has units of an angle (radians).

Figure 1.20 illustrates how incident X-rays, $\mathbf{k}_i$ are scattered by two par-

ticles, changing the direction in $\mathbf{k}_s$. Only the direction of the waves are changed through scattering, but their magnitude do not change. If both incident X-rays are in-phase, they become out of phase from the scattering process, due to their differences in path length before scattering, l_1 and after scattering l_2 . We can calculate the path length difference, as cos α is related to the dot product of $\mathbf{k}_i$ and $\mathbf{r}$:

$$\mathbf{k}_i \cdot \mathbf{r} = |\mathbf{k}_i| r\cos\alpha = \frac{2\pi}{\lambda} r\cos\alpha \tag{1.15}$$

and cos β is related to the dot prouct of $\mathbf{k}_s$ and $\mathbf{r}$:

$$\mathbf{k}_s \cdot \mathbf{r} = |\mathbf{k}_s| r\cos(180^\circ - \beta) = \frac{2\pi}{\lambda} r\cos\beta \tag{1.16}$$

The path length difference as a result of equations (1.15) and (1.16) each contribute a phase difference. The total phase difference is a sum of both phase differences, and the total phase difference can be shown as:

$$\frac{2\pi l_1}{\lambda} + \frac{2\pi l_2}{\lambda} = (\mathbf{k}_i \cdot \mathbf{r}) - (\mathbf{k}_s \cdot \mathbf{r}) = (\mathbf{k}_i - \mathbf{k}_s) \cdot \mathbf{r} \tag{1.17}$$

The overall phase change depends on $\mathbf{Q}$, which is the change in wave vector:

$$\mathbf{Q} = \mathbf{k}_i - \mathbf{k}_s \tag{1.18}$$

From (1.14), we can define the specific scattered X-ray according to its complex exponent as:

$$\psi_1(\mathbf{x}) = \exp(i\mathbf{k}_s \cdot \mathbf{x}) \tag{1.19}$$

The scattered wave will be out-of-phase:

$$\psi_2(\mathbf{x}) = \exp(i\mathbf{k}_s \cdot \mathbf{x})\exp(i\mathbf{Q} \cdot \mathbf{r}) \tag{1.20}$$

Therefore the total scattering is the sum of both X-rays:

$$\psi_1(\mathbf{x}) + \psi_2(\mathbf{x}) = \exp(i\mathbf{k}_s \cdot \mathbf{x}) \times (1 + \exp(i\mathbf{Q} \cdot \mathbf{r}) \tag{1.21}$$

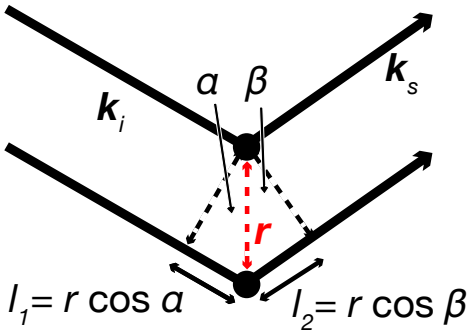

Figure 1.20: Scattering of X-rays $\mathbf{k}_i$ to $\mathbf{k}_s$ by two particles separated by a vector $\mathbf{r}$

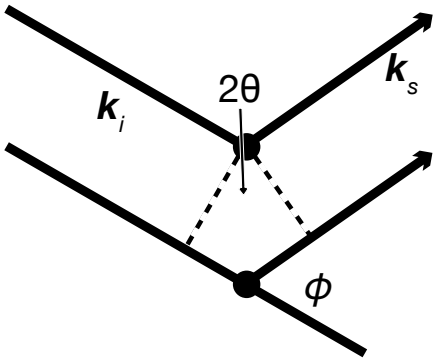

Figure 1.21: Scattering of X-rays $\mathbf{k}_i$ to $\mathbf{k}_s$, showing the labelling 2θ as the internal angle of scattering between $\mathbf{k}_i$ and $\mathbf{k}_s$ and ϕ as the external angle between textbf$\mathbf{k}_i$ and $\mathbf{k}_s$.

The amplitude is modified by the phase factor:

$$F(\mathbf{Q}) = 1 + \exp(i\mathbf{Q} \cdot \mathbf{r}) \tag{1.22}$$

From (1.18):

$$|Q|^2 = |\mathbf{k}_i - \mathbf{k}_s|^2 = {\mathbf{k}_i}^2 + {\mathbf{k}_s}^2 - 2\mathbf{k}_i \cdot \mathbf{k}_s \tag{1.23}$$

We know that magnitudes of each wave are $2\pi/\lambda$, therefore:

$$\mathbf{k}_i \cdot \mathbf{k}_s = \left(\frac{2\pi}{\lambda}\right)^2 \cos 2\phi \tag{1.24}$$

and

$$|\mathbf{Q}|^2 = 2\left(\frac{2\pi}{\lambda}\right)^2 - 2\left(\frac{2\pi}{\lambda}\right)^2 cos2\theta = \frac{8\pi^2}{\lambda^2}(1 - cos2\theta) = \frac{16\pi^2}{\lambda^2} sin^2\theta \tag{1.25}$$

and through calculating the root of each side of this equation, the Bragg equation is obtained:[93]

$$Q = |\mathbf{Q}| = \frac{4\pi}{\lambda} sin\theta \tag{1.26}$$

The Bragg equation is used to equate scattering angles in a diffractometer to real space, d through the equation

$$\lambda = 2dsin\theta \tag{1.27}$$

and reciprocal space, Q using the equation

$$Q = 2\pi/d \tag{1.28}$$

The theory so far discussed is applicable to crystalline systems of an infinite size. In a real sample, adaptations and alterations must be made to consider the effect of finite particles. The sinc function is used to account for the effects of finite particles:

$$g(k) = \sin(k\alpha)/k\alpha \tag{1.29}$$

The form of the sinc function is displayed in Fig.1.22. And in practice, this is used in the form of the Scherrer equation (1.30), used to quantify full width-half max (FWHM) of Bragg reflections, and how their FWHM is related to particle size.

$$\mathrm{B}(2\theta) = \mathrm{K}\lambda/\mathrm{L} \cdot \cos\theta. \tag{1.30}$$

Where B(2θ) is the peak width at a given 2θ value and K is a shape constant for crystallite shape and L is the crystallite size. The Scherrer equation is used by first obtaining the diffractometer-limited peak shape, that is, diffraction patterns in which the crystallite domains are sufficiently large so that the Scherrer broadening is not observed due

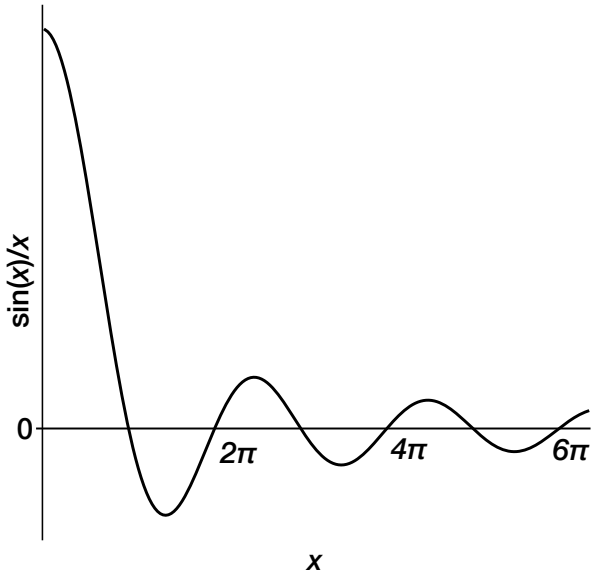

Figure 1.22: sinc function, the product of Fourier transforming the slit function

to other effects being larger.[94] This is created through fitting Pseudo-Voigt function, convoluting Gaussian and Lorentzian functions with a known, highly crystalline standard such as Si or annealed CeO_2. From this peak shape, fitting of the diffraction pattern through the variable L to broaden reflections in the Scherrer equation.

1.3.2 Powder X-ray diffraction

To understand the structure of a given crystal, diffraction is one of the most effective, and information-rich methods. A diffraction pattern can give information of the orderings of crystal planes, the size of crystal domains, disorder and defects.

The most readily available, fastest and cheapest method of diffraction is through use of X-rays. X-ray diffraction relies on measuring the diffraction of monochromated X-rays, which have been scattered by a crystal structure in such a way that the photon's energy does not change. This is referred to as coherent elastic scattering.

The most important information garnered from X-ray diffraction is the distances between atom planes. Where between two planes, separated by distance d, the diffraction can be measured as an intense peak at the angle θ according to the Bragg equation:

$$n\lambda = 2\,d\sin\theta \tag{1.31}$$

In a powder sample, which is composed of polycrystalline material, the diffraction patterns is distinctly different from that of a single crystal. A polycrystalline sample has a distribution of all orientations of a crystal present, due to the lack of conformity between crystal domains of different particles. As such, the orientation of the crystal is not a relevant factor, only the angle between X-ray source and detector. Because the orientation can be disregarded, the sample can be irradiated in the same configuration, with the incident angle being the independent variable for powder diffraction.[93]

1.3.3 X-ray pair distribution function

X-ray pair distribution function (XPDF) is a diffraction-based technique, the main application for which is elucidating the short-range ordering of a material. By measuring the X-ray diffraction pattern, and performing a Fourier transform, the atomic pair distribution function is generated. The Fourier transform allows information from both Bragg peaks and diffuse reflectance to be combined, giving a real space measurement for atomic distance correlations.

Because of the Fourier transform required to generate XPDF data, measurements require data to be measured over a wide range of Q (up to 30 - 50 $Å^{-}1$), as this dictates the resolution. To achieve such a range of Q, short wavelength radiation is required, thus synchrotrons are commonly used for measurements to achieve high brilliance and tunable wavelength. There are now two different dedicated diffractometers for XPDF analysis, I15-1 at Diamond Light Source, and 11-ID-B at Advanced Photon Source. These dedicated beamlines are necessary for some XPDF measurements, as the data demands very short wavelength radiation, and detectors at very high angles to obtain the highest possible range of Q for the highest quality data. High brilliance from synchrotron radiation is beneficial particularly for analysis of small crystalline domains (such as nanoparticles) where they contribute small proportions of total scattering due to support materials, or highly disordered or liquid samples, to maximise the signal from these features.

Pair distribution function data shows the distance of an atomic correlation in real space, and the relative frequency at which these correlations occur. This can be used to observe nanoparticles , crystal structures, disorder or amorphous materials.

Real space in a crystal structure can be represented as a histogram of interatomic distances within a crystal strucutre, with distance on the x-axis and number of pairs in the y-axis(Fig. 1.23). This histogram describes an atom, i and the number of correlations to other atoms j at a given distance, r_{ij}. For every atomic pairing, this is weighted according to the scattering intensity of the given atoms, in the case of X-ray diffraction this is weighted according to the number of electrons, and is represented as b in the below equation for a radial distribution function.

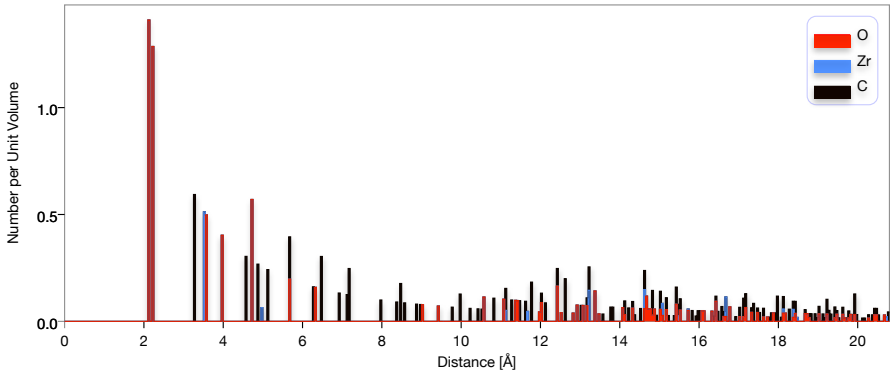

Figure 1.23: A histogram showing the number of correlations involving Zr atoms with Zr,O and C atoms. Due to the strong X-ray scattering of Zr relative to O and C, this is a good approximation of the radial distribution function.

.

$$\mathrm{R(r)}=\frac{1}{\mathrm{N}}\sum_{\mathrm{i,j}\neq 1}\frac{\mathrm{b_i}^{*}\mathrm{b_j}}{\langle \mathrm{b}\rangle^{2}}\delta(\mathrm{r}-\mathrm{r_{ij}}) \tag{1.32}$$

Where $\langle \mathrm{b}\rangle$ is the stoichiometric average of weights across the crystal, and * repesents the complex conjugate of weights. A delta function has an area of 1, thus $\int_{lower}^{upper}\delta(r)dr=1$, which can be used to integrate R(r) from below to above, to obtain N(r).

$$N(r)=\int_{r_{below}}^{r_{above}}\frac{\langle b\rangle^{2}}{b_i^{*}b_j}R(r)dr \tag{1.33}$$

After this data has been normalized according to x-ray scattering factors, peak sizes (integral values) are not identical. These are affected by the

form factor of X-rays, where peaks become dampened at larger values of r., and multiplicity of pairs.

The delta function in above equations describes a finite location for each pair, which is incorrect in a physical system with Brownian motion. Including gaussian peak shapes describes a real system more precisely.

In an extended crystal structure, the number of atomic correlations for r_i increases as the distance $\mathrm{r_{ij}}$ increases, growing as the surface area of the sphere $\mathrm{r_{ij}}$. As such, the number of atomic correlations increases $\propto 4\,\pi \mathrm{r}^2 \rho_{\mathrm{o}}$, where ρ_{o} is the average atom number density.

The quadratic baseline makes analysing features at longer values of r difficult, therefore removing it is necessary in an extended structure. Normalising the radial distribution function according to the spherical area generates G(r).

$$G(r) = \frac{R(r)}{r} - 4\pi r \rho_0 \tag{1.34}$$

G(r) is the most common function referenced in PDF. Its baseline, $-4\pi r \rho_{\mathrm{o}}$, is less obstructive to features in the data than the quadratic of R(r), allowing it to be easily fit, and allowing large ranges of Q to be observed.

γ_{o} allows the G(r) function to describe physical samples more presicely, with γ_{o} representing crystallite domain sizes, and the peak intensities resulting from this physical property. When crystallites are very large, this term tends to γ_o=1, so it is only very relevant for nanocrystallites or nanoparticles.

$$G(r) = \frac{R(r)}{r} - 4\pi r \rho_0 \gamma_0 \tag{1.35}$$

Pair distribution function requires a large amount of data processing from its raw form, the powder X-ray diffractogram. First the diffractogram is Fourier transformed,and corrected for erroneous effects such as Compton scattering, fluorescence, and scattering from sample holders. These steps yield the function I(Q).

$$I(Q) = \int_0^\infty \sum_{i,j} b_i^* b_j \delta(r - r_{ij}) \frac{sin(Qr)}{Qr} dr \tag{1.36}$$

$$= p + \sum_{i=0}^{n} f(x)$$

I(Q) is the background-corrected intensities, measured against Q ($Å^{-1}$). S(Q) is the total scattering, normalizing intensities by the average scattering factor (ρ_0). F(Q) is the reduced structure function. G(r) is the Pair distribution function.

$$G(r) = \frac{2}{\pi} \int_0^\infty 4\pi r[\rho(r) - \rho_0] \tag{1.37}$$

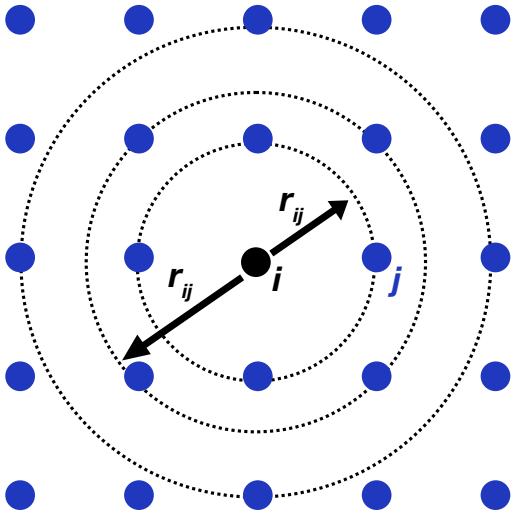

Figure 1.24: An example crystal, where atoms in blue are observed from the atom, i, black. The interatomic distances from i - j are shown as r_{ij}.

.

XPDF experiments measure complete scattering of the sample during irradiation, and the observed data is F(Q), where Q is the wave vector change in the experiment. Obtaining the G(R) of true physical representation requires precise data processing. Tuning parameters in data processing is essential to extract true data from PDF analysis; polynomial background terms (r_{poly}),Q_{max} and Q_{min}

In the appendix, Fig.6.2 shows the importance of data processing for PDF. The same data processed with different r_{poly} values produce completely different G(r)

1.3.4 Transmission electron microscopy

Electron microscopes come in various forms, suited to specific purposes, such as topographic mapping, electron diffraction, 2D and 3D imaging. This thesis utilises scanning electron microscopy (SEM), transmission electron microscopy (TEM) and scanning tunelling electron microscopy (STEM). SEM is best suited for low magnification imaging of surfaces (generally of the order of 10s of nm or above), whereas TEM and STEM are capable of much higher resolution and thus magnification, allowing imaging of surfaces, lattices and features down to the sub-nanometer level. TEM and STEM provide unique insights to the structure of heterogeneous catalysts, nanoparticle size, morphology and variation thereof.

The resolution of a microscope can be defined by the Rayleigh criterion for visible light microscopes,

$$\delta = \frac{0.61\lambda}{\mu sin\beta}. \tag{1.38}$$

Equation (1.38) describes the smallest distance, δ, which can be resolved by a microscope of radiation wavelength λ, where μ is the refractive index of the viewing medium and β is the semi-angle of collection of the microscopes lens. $\mu sin\beta$ is often simplified to 1. In a visible-light microscope, this allows for the imaging of features down to approximately 300 nm, which is not suitable for imaging of anything chemically relevant. Electron microscopes introduce much higher resolution, as high energy electrons have much shorter λ than visible light. A 200 kV electron has a wavelength of 2.5079 1×10^{-12} m, whereas the shortest wavelength of visible light is ~3.8×10^{-7} m. These wavelengths lead to an increased resolution of 10^5 by using electrons over visible light.

In an electron miscroscope, the smallest feature which can be imaged, δ is more precisely defined by function (1.39):

$$\delta = \frac{1.22\lambda}{\beta}. \tag{1.39}$$

Equation (1.39) is different, as diffraction lenses are not possible for electron microscopes. The wavelength of an electron can be calculated according to the De Broglie wavelength, (1.40), where E is the electron

energy in eV.

$$\lambda = \frac{1.22}{E^{1/2}}. \tag{1.40}$$

The theoretical resolution limit which can be calculated using equation (1.39) suggests that it is possible to resolve individual atoms with ease, however this is often not the case.

Limitations of electron microscopy, particularly TEM and STEM, are found in the lens apparatus. These systems most commonly use magnetic lenses, the strength of a magnetic field controls the electron trajectories, thus the focus which is a defining parameter of final resolution of an image. Lens imperfections cause a point to be distorted into a gaussian image with a radius dependent on the magnitude of said imperfections. Lens imperfections are largely comprised of, but not limited to: Spherical abberation, chromatic abberation and astigmatism. Spherical abberation refers to the imperfect focusing of electrons at a single point, due to the increased angle of focus for those electrons further from the magnetic axis.

Scattering in electron microscopy occurs as a result of incident electrons (herein referred to as e_i) interacting with the nucleus of an analyte. This scattering can be elastic or inelastic. The chance of an electron interacting with an atom depends on the cross section of said atom, which is defined by equation (1.41)

$$\sigma_{\text{atom}} = \pi r^2. \tag{1.41}$$

For a real sample consisting of multiple atoms, the cross-section can be derived from equation (1.42),

$$\sigma_{\text{total}} = N\sigma_{\text{atom}} = \frac{N_0 \sigma_{\text{atom}} \rho}{A}. \tag{1.42}$$

Where N_0 is Avogadro's number, ρ is the material density in kg m $^{-3}$ and A is the atomic weight in kg mol $^{-1}$.

Inelastic scattering of electrons at a sample give rise to beam-induced damage of the sample. This damage is dependent on the energy of incident electrons, and the dose of electrons received by the sample. Beam damage is comprised of thee main mechanisms:

Radiolysis: Where inelastic scattering from electron- electron interac-

tions leads to ionisation, breaking bonds within the analyte. These interaction promote electrons from valence bands to conduction bands in semiconductors, crystals or polymers. Excited electrons can recombine with their associate hole, and either fluoresce or create an exciton. The pathway leading to excitons creates amorphisation of crystals.

Knock-on damage: Where high energy e_i transfer their energy to atoms within a lattice, and this energy is sufficient to overcome δ_G and displace the atom, leading to a point vacancy and an interstitial defect . This atom can be completely ejected from the structure (therefore producing only a point defect), at which point the process is referred to as sputtering.

Heating: Beam exposure can create phonons within the sample, which leads to heating of the sample and causing thermal degradation. This mechanism is least relevant in this thesis, as the analytes are mostly thermally stable up to 300 °C in inert atmospheres.

All samples will experience beam damage at high currents of high energy electrons, and some which are prone to damage require special treatment to minimise it. Minimising damage can be achieved by using lower energy electrons, by reducing the electron dose experienced by the sample, or a combination of both.

TEM resolution is governed by the ability of the objective lens to image and object.

In TEM, a thin sample is illuminated by a broad monochromatic (or close enough that this assumption holds) electron beam of uniform intensity. The scattering of these incident electrons towards a non-uniform pattern and intensity is the measured quantity used to generate images.

1.3.5 X-ray Photoelectron Spectroscopy

XPS is a surface sensitive technique, probing the elemental composition of the surface and ~10 nm depth. It can identify and quanitfy elemental composition, and give information on chemical envionments and oxidation states.

The principle of XPS relies on the elastic photoemission, wherein an incident photon annihalates upon interaction with an electron at the

surface of a material. During annihilation, complete energy transfer from the photon occurs, and if the energy is sufficient to overcome the work function, the electron is ejected from the surface without losing energy. Kinetic energy of the emitted electron is equal to that of the photon minus the binding energy, as seen in equation (1.43).

$$KE_{\text{Photoelectron}} = E_{\text{X-ray}} - \phi_{\text{XPS}} - E_B^F. \tag{1.43}$$

Where ϕ_{XPS} is the work function of the instrument, this accounts for the minimum energy required to remove an electron from the instrument. E_B^F is the electron binding energy (BE) relative to the Fermi level of the sample. The kinetic energy of the emitted electron is the measured quantity in XPS. This quantity is used to decipher element and chemical environment, as the work function is variable based on these parameters.

If the analyte is insulating, with a poorly defined Fermi level, the energy of photoelectrons can be calculated using equation (1.44)

$$KE_{Photoelectron} = E_{X-ray} - \phi - E_B. \tag{1.44}$$

In (1.44), ϕ is a term which represents uncertainties relating to surface potential and BE. The difference in analysing insulating samples is that the BEs need to be related to by using a reference point.

Fig. 1.25 shows the process of incident x-rays of sufficient energy to overcome ϕ_{XPS} interacting with a Pt $4f_{5/2}$ electron.

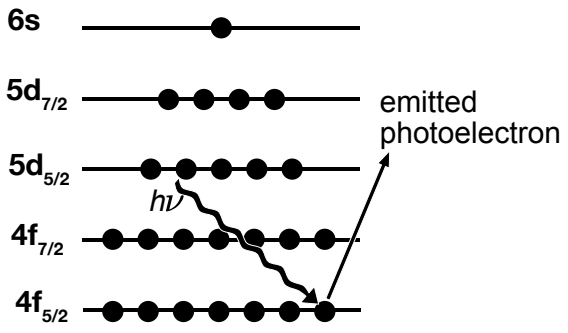

Figure 1.25: A schematic of the XPS analysis process on a platinum atom, measuring the binding energy of a $4f_{5/2}$ electron.

Photolectrons produced through electron de-excitation are also observed in XPS, produced through the Auger process and referred to as Auger electrons. Instead of electrons directly ejected through photon energy

transfer, Auger electrons are valence electrons, which have relaxed to fill a hole generated in a core-shell, resulting in emission.

The spectrum generated in XPS, while measuring $KE_{\text{photoelectron}}$, uses binding energy BE as the independent variable. This is because $KE_{\text{photoelectron}}$ is dependent on the incident X-ray enrgy, whereas BE is not.

X-ray notation uses capital letters: K, L, M, N, O to denote the principal quantum number, where K=1 and so forth. Within the X-ray notation, electrons within a shell are denoted with a subscript integer, where the integer denotes their energy level within the shell, i.e M_1 is the lowest energy level electrons in the d-shell.

Spin-orbit coupling has observable impacts on the binding energies of electrons in an atom. When 2 electrons have the same n but different l, this can be observed. Spin-orbit coupled electrons are differentiated by denoting their j value, where j is the total angular momentum quantum number and $j = l + m_s$. In the example of a $2p$ orbital, spin-orbit coupled electrons would be denoted as $2p_{1/2}$ and $2p_{3/2}$. These electrons exist in slightly different energy states, and these splittings in energy are referred to as the fine structure.

Subshell	j values	Area ratio
s	1/2	-
p	1/2, 3/2	1 : 2
d	3/2, 5/2	2 : 3
f	5/2, 7/2	3 : 4

Table 1.2: Spin orbit coupling effects on different subshells in XPS.

The intensities of measured photoelectrons are dependent on 3 parameters, (a) Physics of photoelectron production (b) Parameters describing the interaction of produced photoelectrons with the measured material and (c) Instrument geometry

The physics of photoelectron production is generally accounted for by the photoelectron cross section, which describes the likelihood of photoelectron production from a specific atom type. The photoelectron cross-section is element specific, and will not vary based on chemical environment.

l is the angular momentum quantum number, with integer values from

0 to n -1. When $l = 0$, electrons exhibit spherical distributions, and l $\neq 0$, distributions are non-spherical.

XPS is capable of differentiating between oxidation states and chemical states at a surface. This is achieved by using 'chemical shift', which gives rise to BE differences. The atomic charge relates to BE through the charge potential model,

$$E_i = E_i^0 + kq_i + eV_i \text{ where } V_i = \sum_{i \neq j} \frac{q_i}{r_{ij}}. \tag{1.45}$$

Where E_i is the BE for a specific electron at atom i, E_i^0 is reference energy, k is a constant, q_i is atomic charge at atom i and V_i sums the potential at atom i due to effects from on other atoms, j, including point charges q_i and distance from i, r_{ij}. For atom i, shifting its chemical environment, (1.46) shows how the BE changes

$$\Delta E_i = k\delta q_i + e\delta V_i. \tag{1.46}$$

Chapter 2

Experimental

2.1 UiO-66(NH_2) synthesis

UiO-66(NH_2) syntheses were all conducted in solvothermal conditions using either Parr teflon autoclave or Schott Bottles. Teflon autoclaves are used where the temperatures are expected to generate significant pressure, or when reproducing previous work.

After synthesis, the microcrystalline powders require washing and activation to remove solvents and unreacted starting materials. Solids are isolated after synthesis, and between each wash, by centrifugation until the supernatant is clear. Specific procedure is detailed for each synthesis.

2.1.1 Defect-controlled hydrothermal synthesis of UiO-66(NH_2)

In a 23mL Teflon-lined autoclave, 0.3 mmol of $ZrCl_4$ and different amounts of NH_2BDC (0.3, 0.6, 0.9 1.2 mmol) were added to 4 mL H_2O and 1 mL formic acid (where the formic acid: Zr ratio is 88:1). The vessels were sealed and heated to 120 °C for 24 hours. Samples were then cooled and washed in H_2O at 60 °C once for 24 hours, and then a further two times for 2.5 hours each. The remaining solid is activated at 200 °C for 24 hours.

2.1.2 Stoichiometry to control defects in UiO-66(NH_2) (DMF)

In a 23mL Teflon-lined autoclave, 0.3 mmol of $ZrCl_4$ and different amounts of NH_2BDC (0.3, 0.6, 0.9 1.2 mmol) were added to 4 mL DMF and 1 mL formic acid (where the formic acid: Zr ratio is 88:1). The vessels were sealed and heated to 120 °C for 24 hours. Samples were then cooled and washed at 90 °C in DMF once for 24 hours, and then a further two times for 2.5 hours each. The remaining solid is activated at 200 °C for 24 hours.

2.1.3 Modulator concentration to control defects in UiO-66(NH_2)

In a Schott bottle, 1.2 mmol of $ZrCl_4$ and 1.2 mmol NH_2BDC were added dissolved in different amounts of formic acid (1, 2, 5, 10 mL) with formic acid: Zr ratios of 22:1, 44:1, 110:1 and 220:1 respectively, and DMF (24, 23, 20, 15 mL). The mixture was heated at 90 °C for 24 hours beforewashing at 100 °C in DMF once for 24 hours, and then a further two times for 2.5 hours each. The remaining solid is activated at 200 °C for 24 hours.

2.1.4 Water content to control defects in UiO-66(NH_2)

To control the defect properties of UiO-66(NH_2) using water content, reactants are added in order of hygroscopicity. Deionised water was added first (**high defect** 0.2 mL, **med defect** 0.1 mL, and no water for **low defect**), followed by 2-aminoterephtalic acid (H2NH2BDC) (43.5 mg, 0.24 mmol), 4.8 mL anhydrous DMF, 0.2 mL formic acid and finally $ZrCl_4$ (55.9 mg, 0.24 mmol). The formic acid: Zr ratio is 22.1:1. The vessel was placed into a 150 °C oven for 24 hours, then allowed to fully cool before the solid light yellow microcrystalline powder product was collected by centrifugation.

2.1.5 Washing and activation procedures of UiO-66(NH_2)

Around 200 mg UiO-66(NH_2) was washed with 10 mL DMF for 2.5 hours at 100 °C before the solvent was exchanged and the washing repeated twice: once for another 2.5 hours and then finally for 16 hours. The DMF-washed UiO_66(NH_2) was then solvent-exchanged using 20 mL MEOH for 2 hours and then dried, and activated by heating at 150 °C for 24 hours.

2.2 Plasma cleaning of UiO-66(NH_2)

10 mg UiO-66(NH_2) powder was dispersed in methanol and sonicated for 5 minutes. The suspension was dropped onto a silicon chip of dimensions approximately 15 x 10 mm, and allowed to evaporate at room temperature yielding a thin film. The thin film was placed under an argon atmosphere of 0.04 bar, and argon ions were induced with a power of 50-100 W, where samples were exposed for different amounts of time. Plasma cleaned samples were analysed by PXRD on the Si chip due to the small amount of sample, and for direct comparison by PXRD before and after plasma cleaning.

2.3 Powder X-ray diffractometry (PXRD)

PXRD data was collected using a PANalytical X'Pert Pro diffractometer using monochromated Cu Kα 1 radiation (λ= 1.5406 Å). Measurements were performed from 2°–70 ° in Bragg Brentano geometry.

2.4 Pawley refinement of PXRD data

Pawley refinements of UiO-66(NH_2) were carried out carried out using TOPAS Academic.[95] The refinement was carried out using a space group $Fm\bar{3}m$ as there was no evidence of diffuse scattering corresponding to primitive defect nanodomains. In addition to the lattice parameter and a Chebyshev background term, sample-dependent peak broadening terms were refined (crystallite size-dependent Gaussian broadening), with in-

strumental peak parameters derived from refinement of a highly crystalline standard.

2.5 Thermogravimetric analysis (TGA) measurement

TGA measurements were collected using a Q500 TA Instruments TGA. 5–10 mg sample was loaded into a platinum pan and heated at a ramp rate of 10 °C /min, from 25 °C – 1000 °C, under an airflow of 40 mL/min.

2.6 Platinum deposition

This section describes deposition of Pt co-catalyst onto UiO-66(NH_2) support material to create the photocatalyst (Pt @ UiO-66(NH_2))investigated for photocatalytic hydrogen generation.

300 mg of activated UiO-66(NH_2) was heated at 60 °C under vacuum for 6 hours to remove any surface moisture and then loaded into a bulk deposition holder for a magnetron sputtering deposition. The dried sample was stirred under vacuum, and Pt nanoclusters were deposited onto the sample using Ar plasma and a Pt target (Kurt J. Lesker), with a power of 70 W for 30 minutes.

After deposition, Pt content was determined using inductively coupled plasma optical emission spectroscopy, and PXRD measurements of the catalyst were taken to ensure the MOF maintained its structure upon Pt deposition.

2.7 Transmission Electron Microscopy Measurement

TEM images were collected at the University of Nottingham Nanoscale and Microscale Research Centre on a JEOL 2100F field emission gun TEM with an accelarating voltage of 200kV. The microscope is equipped with Gatan K3–IS camera, using the Gatan GMS software for analysis.

Images were analysed using Fiji. All distances quoted are measured by drawing line profiles across the largest diameter of quoted particles, and particle size histograms were fit to lognormal distributions.

2.8 Photocatalysis reactions

Photocatalysts were first prepared by creating a thin film on a glass slide. Catalyst samples of Pt @ UiO-66(NH_2) (3mg) were suspended in methanol (~2mL), sonicated for 30 seconds and dropped onto a borosilicate glass slide (15 x 45 mm) and dried at ambient to create a thin film. This slide was loaded in a quartz glass reactor and 10 mL 10% aqueous methanol solution added, ensuring that all catalyst is below the surface of the solution. The reactor was then purged with argon, by bubbling into the solvent at 100 sccm for 15 minutes, at which point N_2 and O_2 peaks were no longer observed in thermal conductivity detectors in gas chromatography of the headsapce. The reaction was then illuminated with 50 W 365 nm Evoluchem UV LED placed at 5 cm from the catalyst, under 1.0 sccm Ar gas flow. Every 14 minutes, automatic gas injections were taken from the reaction headspace by a programmed gas chromatogram (GC), for GC analysis using thermal conductivity and flame ionisation detectors.

2.9 X-ray pair distribution function analysis

All X-ray pair distribution function (XPDF) analysis was conducted at Diamond Light Source, beamline I15-1 using X-rays with λ =0.161669.

Data for Pt @ UiO-66(NH_2) samples after catalysis were collected for 30 minutes. Variable temperature measurements for Ni/Pt @ UiO-66(NH_2) were collected for one minute per measurement.

XPDF data was processed using PDFgetx3. Due to the small change in F(Q) between samples, they were all processed using the same parameters: $r_{poly} = 0.9$, $Q_{maxinst} = 19$, $Q_{max} = 19$, $r_{min} = 0.0$, $r_{max} = 28.9$, $r_{step} = 0.01$. XPDF data was fit using TOPAS academic v6, using *fcc* Pt, with *r*-dependent peak broadening and peak damping.[95]

2.10 Scanning electron microscopy (SEM)

SEM samples were prepared by grinding analyte into a fine powder, then applied to a carbon tab on a 10 mm stub. Samples are are coated with carbon and imaged in a JEOL 7100F field emission gun scanning electron microscope.

2.11 Diffuse reflectance spectroscopy ultraviolet-visible spectroscopy (DRS UV-vis)

Samples for DRS UV-vis analysis were analyzed on a Cary series UV-vis-NIR spectrophotometer in a teflon sample holder. Measurements were taken from λ = 200 - 800 nm at 1 nm intervals.

2.12 X-ray photoelectron spectroscopy

XPS measurements were performed on a Kratos Axis Ultra DLD spectrometer with a monochromatic Al K α X-ray source (hν = 1486.6 eV).

XPS data was fit using Casa XPS. All peaks used Shirley backgrounds. FHWM for spin-orbit coupled peaks were constrained to be equal. Spectra were calibrated using adventitious carbon at 284.8 eV. Peak shapes and splitting constraints for each element are shown in table 2.1. Oxygen was fit to three peaks, corresponding to the three O environments in UiO-66(NH_2): Zr-O-Zr, Zr-O-H, Zr-O-C. Pt was fit to two Pt^0 peaks when the data gave sufficient fit, however often it was necessary to introduce a second pair of $Pt^{\delta+}$ peaks. Zr was fit to two peaks when the data gave sufficient fit, however in defective samples it was sometimes necessary to introduce a second pair of peaks. Some C1s spectra gave insufficient fits with only three components, and required a π - π^* satellite peak to be added, however this component is only present if the fit was otherwise missing intensity at high BE.

Element	Peak shape	Splitting constraint (eV)
Zr 3d	GL(30)	2.4
Pt ^{0}4f	LA(1.2,3,50)	3.35
Pt $^{\delta+}$4f	GL(50)	3.35
C 1s	GL(30)	NA
O 1s	LA(50)	NA
N 1s	LA(50)	NA

Table 2.1: Peak shapes and spin-orbit coupled splitting constraints for components in XPS fitting

2.13 Inductively coupled plasma optical emission spectroscopy (ICP-OES)

Approximately 1 mg of catalyst was dispersed in a solution of aqua regia (prepared by mixing 32% HCl and 32 % HNO_3 in a 3:1 v/v ratio). The dispersion was sonicated for one hour, and left to stand for a further 72 hours at room temperature. Any solids remaining were separated by centrifugation, and the supernatant was measured on a Perkin Elmer Optima 2000 spectrometer.

2.14 Gas chromatography

Products evolved during photocatalysis were analysed using an Agilent 7890B gas chromatograph, where the thermal conductivity detector (TCD) was used to detect hydrogen, nitrogen and oxygen. Any impurities or side-products are detected using the flame ionisation detector (FID). Injections from the reaction headspace were taken every 14 minutes, with the first injection taken as the light source is illuminated.

Chapter 3

Defect-stabilised Platinum Catalysts at UiO-66(NH_2)

3.1 Introduction

In Chapter I, I introduced the scarcity of PGMs and the associated environmental impacts of their extraction. This chapter investigates one approach for the more efficient use of PGMs in catalysis, increased atomic utilization through reduced particle sizes, and stabilisation of small nanoparticles to extend the lifetime of these highly active species. By tuning metal-organic frameworks, it is possible to induce large concentrations of vacancy defects, which can provide an anchoring sites for the deposited catalysts, stabilising them with respect to sintering. This chapter applies these defect-stabilised catalysts to photocatalytic hydrogen generation, an important reaction for potential future fuel applications. Developing stable nanoparticles on a photocatalyst is pertinent, as photon energy is less likely to cause sintering than thermal catalysis, as discussed in *Photocatalysis*. Combining defect engineered support materials with photon energy sources gives a high likelihood of generating stable supported nanoparticles.

It is important to clearly state nomenclature in photocatalysis, which is unclear and sometimes counter intuitive to those who are not experienced with photocatalysis. The support material (UiO-66(NH_2)) is the photocatalyst, absorbing photons and transferring energy to the deposited material (Pt). Pt is the co-catalyst (despite being the 'active site' for hydrogen generation), as its role is to accept photoelectrons

and increase the rate of photocatalysis. I often refer to the material (Pt@UiO-66(NH_2)) as a 'catalyst', when not describing individual elements for ease of communication.

The MOF UiO-66(NH_2) is a commonly used catalyst for photocatalytic hydrogen generation, due to its high stability and visible light absorption.[96–98] This material is most commonly deposited with Pt, where UiO-66(NH_2) act as a photocatalyst for photoelectron capture. The Pt species enhances charge separation and accepts photoelectrons, acting as the active site for photocatalysis, greatly increasing the TOF. It has been shown that Pt particles located beneath the surface of the MOF produce a greater activity than those at the surface (Fig.3.2)[81]. This discovery was characterised using TEM, relying on the ability for electrons to penetrate through the whole UiO-66(NH_2) particle and observe all Pt present. Larger UiO-66(NH_2) particles make this characterisation increasingly difficult, as electron scattering becomes more apparent.

Composite materials are a commonly used method to enhance photocatalytic activity, due to the heterojunctions created, as discussed in *Photocatalysis*. These composites have also been used to stabilise Pt co-catalysts in a Pt @ UiO-66(NH_2) system. A composite of UiO-66/SnO_2 nanoparticles immobilises SACs, and increases activity towards photocatalytic hydrogen production by 5 times compared to Pt @ UiO-66(NH_2).[99] The research by Sui *et al.*[99] (Fig. 3.1) and that of Xiao *et al.*[81] (Fig. 3.2) are the state-of-the-art in Pt @ UiO-66(NH_2) photocatalytic hydrogen production, although it should be noted that even the best UiO-66 and UiO-66(NH_2) photocatalysts have notably lower activity than TiO_2 or Pt @ TiO_2 towards photocatalytic hydrogen generation. However, UiO-66(NH_2) photocatalysts still receive lots of attention due to the visible absorption present, which is highly important when considering the applications in harnessing sunlight, as sunlight produces only 3 % UV light.

Defects have been introduced to catalyst supports to effectively provide both active sites for reaction and anchoring sites for catalysts.[100,101] The latter is particularly commonly applied for single-atom catalysts, which are highly mobile due to their high surface energy.[13]

Fig.3.3 shows an example of a defect site used to stabilise a Ni SAC in defective graphene. HAADF-STEM images show the Ni atom residing

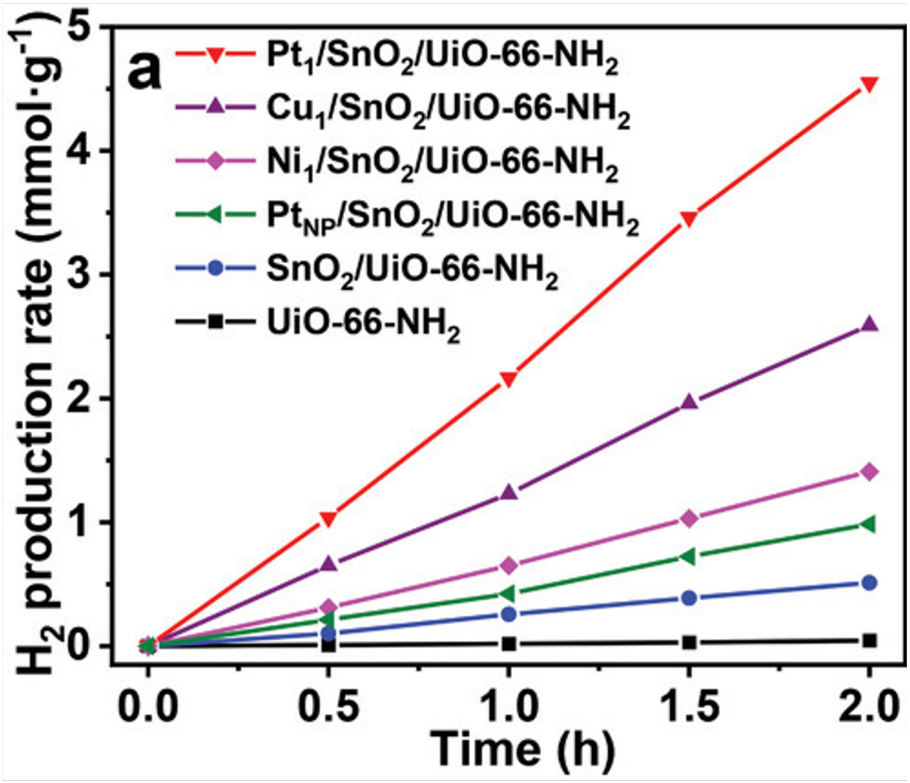

Figure 3.1: Photocatalytic hydrogen generation activity for UiO-66(NH_2) without Pt, with Pt deposited, and various UiO-66(NH_2/SnO_2 composites). Reproduced from ref. [99]

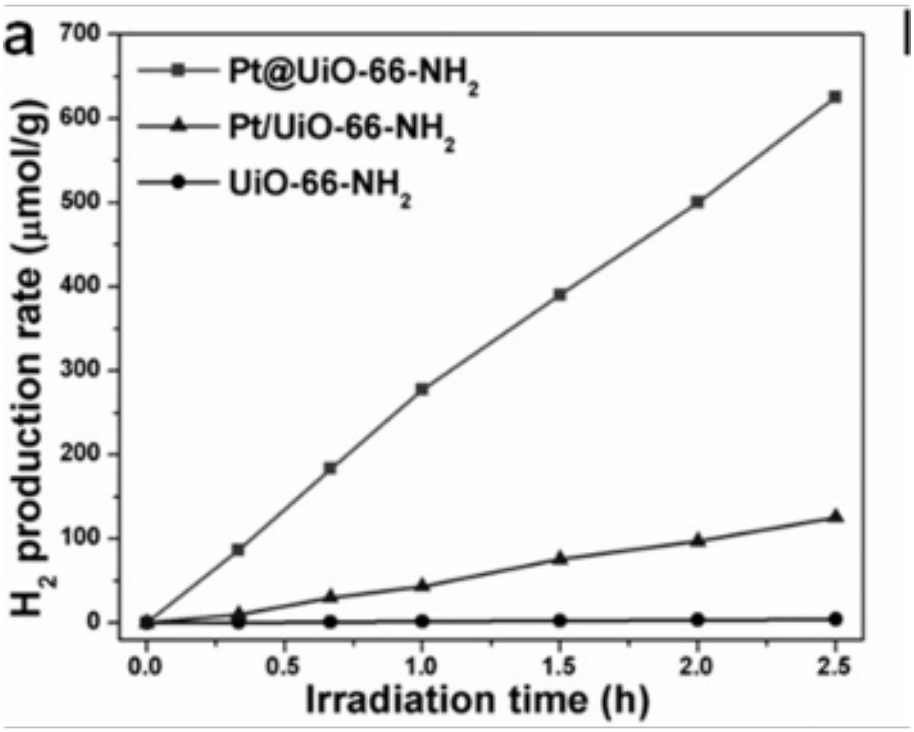

Figure 3.2: Photocatalytic hydrogen generation activity for UiO-66(NH_2) without Pt, with Pt deposited at the surface (labelled Pt/UiO-66-NH_2) and Pt deposited inside MOF particles (labelled Pt @ UiO-66-NH_2). Reproduced from ref. [81]

within the defect site, with a vacancy defect highlighted in (a), and a vacancy stabilising Ni single atom at the defect site highlighted in (b).

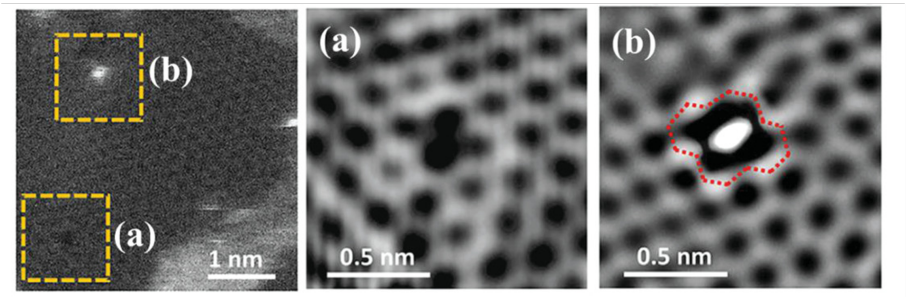

Figure 3.3: (left) A wide view of Ni@ defective graphene, with the highlighted sections (a) and (b) shown in the middle and right images respectively. (middle) A carbon vacancy point defect in graphene. (right) A carbon vacancy point defect in graphene anchoring a Ni single atom. Reproduced from[101]

Supports such as graphene and ceria, have positive results regarding defect chemistry in catalysis, although these supports are limited by their low concentration of point defects.[102,103] Metal-organic frameworks, particularly the UiO family of MOFs, can facilitate much larger concentrations of defects due to high connectivity, rigid ligands and strong Zr-O bonds. UiO family MOFs provide an opportunity to exploit the potential of defects in catalysis further, providing stabilising effects at more 'anchor sites', therefore allowing larger loadings of catalyst with good dispersion and low particle sizes.

3.2 Results

3.2.1 Defect-controlled synthesis

This research project requires a series of MOFs with different missing linker defect concentrations to use as support materials. A synthesis for UiO-66(NH_2) meeting this criterion has not been reported for a series of more than two defect concentrations. This subchapter explores synthetic procedures to generate MOFs with different missing linker defect concentrations. Any references to 'defects' in this thesis hereafter refers to missing linker vacancies, unless otherwise specified.

I aim to vary defect concentration while leaving other MOF properties unchanged, to isolate the effects of defects on catalytic activity and stability. I synthesised UiO-66(NH_2) using multiple independent variables

to introduce missing-linker defects. In this sub-chapter, some of the most interesting series of syntheses are shown, with the PXRD and TGA analysis characterisation reported for samples in the series. In this thesis, independent variables utilised to introduce defects here are: modulator concentration, linker concentration and water content. PXRD analysis is used to assess the phase purity of the desired fcu UiO-66(NH_2), characterising any **reo** or **hcp** phases and particle size dependent broadening. TGA is used to quantify the combustion of organic linkers under aerobic heating, comparing to the final weight at 1000°C (ZrO_2) to calculate stoichiometry between linker and cluster, thus generating a missing linker concentration. All PXRD patterns are normalised such that the most intense peak is equal between samples, and shown with a zoomed section into the low Q range with the same normalisation. Normalisation makes comparison between sample peak intensities more clear, and removes any ambiguity which may arise due to overall intensity changes caused by PXRD methodology. Zooming into the low Q region better shows any **reo** nanodomains or **hcp** presence, both of which are undesired phases. All TGA data are normalized by their final weight (which is normalized to 100%), for clarity of visual comparison.

The ratio of NH_2BDC: $ZrCl_4$ in reported syntheses is typically equimolar in a UiO-66(NH_2) synthesis, as they are equimolar in the desired MOF, but can be varied to induce change on defect concentration or phase.[51,54] By increasing the concentration of linker, while keeping a constant modulator and metal salt concentration, the inhibition towards cluster-linker co-ordination formation (and therefore missing linker concentration) should be reduced, and vice versa. Using this method to control defect formation, I developed a synthesis of UiO-66(NH_2) with variable stoichiometry ratios of linker:cluster . This series is shown in Fig.3.4.

For the ligand:metal ratios 0.25:1 and 0.5:1, the product is clearly of low crystallinity, indicated by broad peaks and a low signal:noise ratio, indicating that the crystalline domains are very small. The first peak (which would be *111* in the **fcu** phase) in the 0.5:1 ratio is split into two; the locations and magnitudes of these two peaks indicates that this contains **hcp** phase, and therefore not the desired phase-pure **fcu**.

All remaining ligand:metal ratios show phase-pure, crystalline **fcu** phase. The material synthesised using a 0.75:1 ratio has broader peaks, indicat-

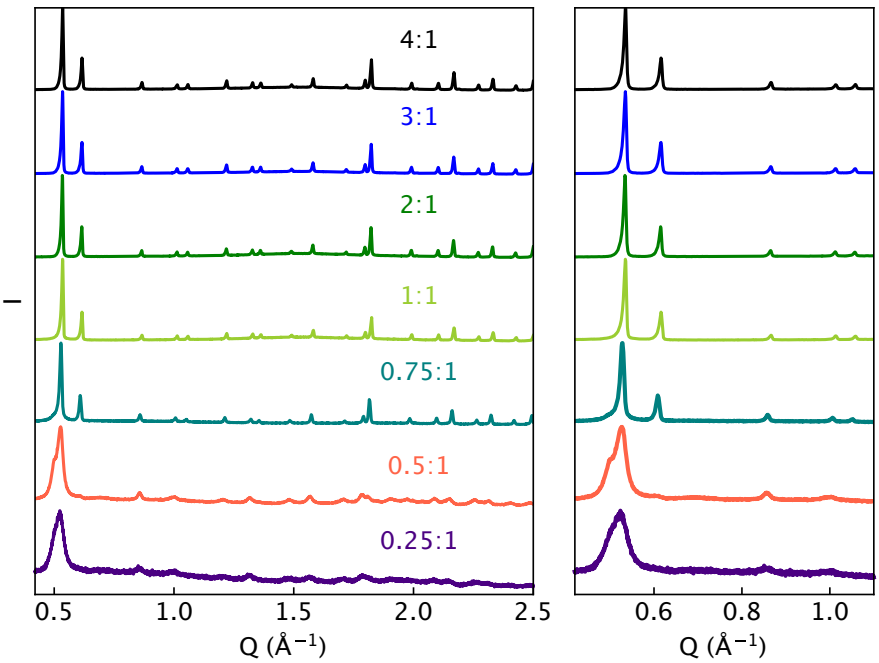

Figure 3.4: PXRD of UiO-66(NH_2) with varied NH_2BDC:$ZrCl_4$ ratios.

ing that the particle size is lower. 1:1, 2:1, 3:1 and 4:1 have almost identical PXRD patterns, however the presence of missing linkers is randomly distributed, and the atoms within linkers scatter X-rays much weaker than Zr atoms, so similar PXRD patterns does not inform of defect concentrations. TGA analysis is required to understand the proportion of randomly distributed missing linker defects.

The TGA data for these samples using stoichiometry control are shown in Fig.3.5. The black dashed line relates to the lowest temperature at which surface-adsorbed water has been completely evaporated, with an elemental composition of $Zr_6O_4(OH)_4(NH_2BDC)_x$. I refer to this temperature as the 'dehydrated temperature'. Samples 0.25:1 and 0.5:1 show very low mass losses after the dehydration temperature, which would indicate high defect concentrations, however the potential for **hcp** and amorphous domains in these samples make the calculations imprecise, therefore defect concentrations cannot be clearly stated.

The 0.75:1 has 26.7 % missing linker defects, 1:1 has 35.0 % and 2:1 has 10%. In this series, I expected the lower ligand: metal ratios to show higher defect concentrations, whereas the data does not follow this trend.While a wide range of defect concentrations were created in this series, the synthetic procedure does not have a rational trend which can be relied upon for defect generation. TGA data for Ligand: metal ratios

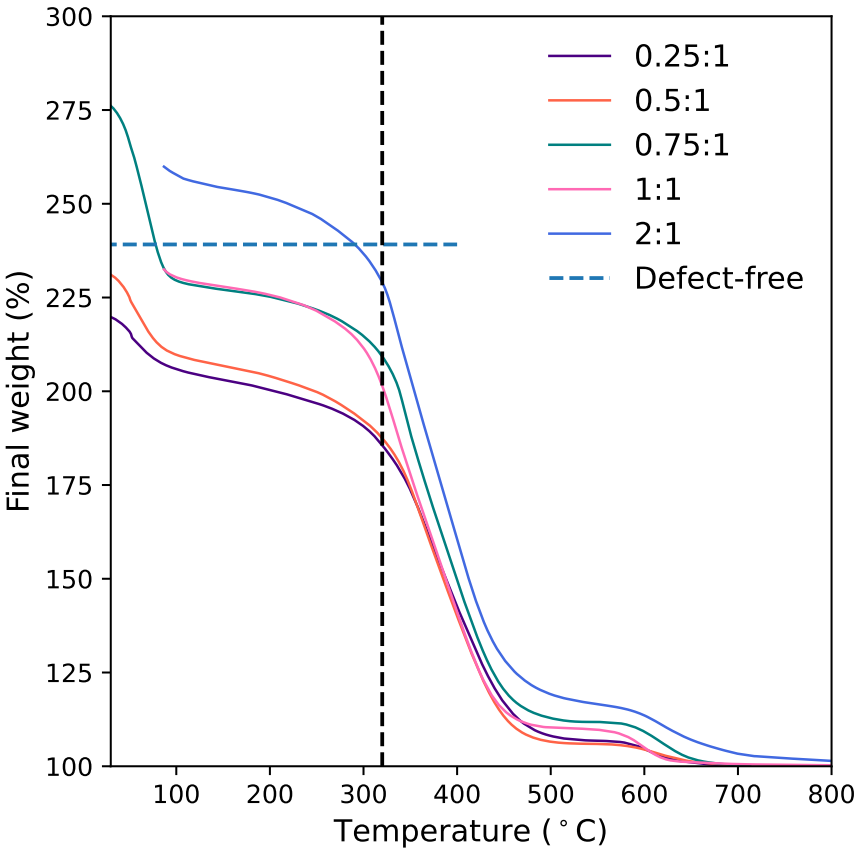

Figure 3.5: TGA of UiO-66(NH_2) with varied NH_2BDC:$ZrCl_4$ ratios.

above 2:1 are not shown, as such large concentrations of ligand leave large amounts unreacted, which is difficult to remove from the pores during washing. This unreacted ligand causes spurious results in TGA analysis, due to increased mass losses from its combustion.

Washing procedures are very important for the synthesis of a MOF, particular one of high porosity such as UiO-66. Washing removes excess unreacted starting materials and co-ordinated modulators, which will effect applications, diffraction patterns, surface area and TGA analysis. If the MOF contains materials which cannot be precisely accounted for, such as unreacted starting materials, TGA analysis is impossible to use quantitatively because the mass losses are unpredictable. In the syntheses using excess ligands, these extra mass losses were clearly observed. The acidic reaction conditions of UiO-66(NH_2) synthesis mean that unreacted ligand will be in the diacid species, NH_2BDCH_2. NH_2BDCH_2 is very poorly soluble in every solvent due to the large amount of potential hydrogen bonds, and washing in hot (120°C) DMF was not enough to remove the large amounts of unreacted ligand in higher ligand:metal

ratios.

To create robust washing procedures, I tested the effects of washing on TGA data. Washing the MOF synthesised in a 2:1 ligand:metal ratio, and analyzing by TGA to measure the number of washes required to completely remove unwanted material from the framework. 2:1 was tested because it allows for hyperstoichiometric ligand, but any higher stoichiometries I deemed wasteful with respect to the large amount of DMF required to completely remove unwanted material through washing. The testing is shown in Fig.3.6

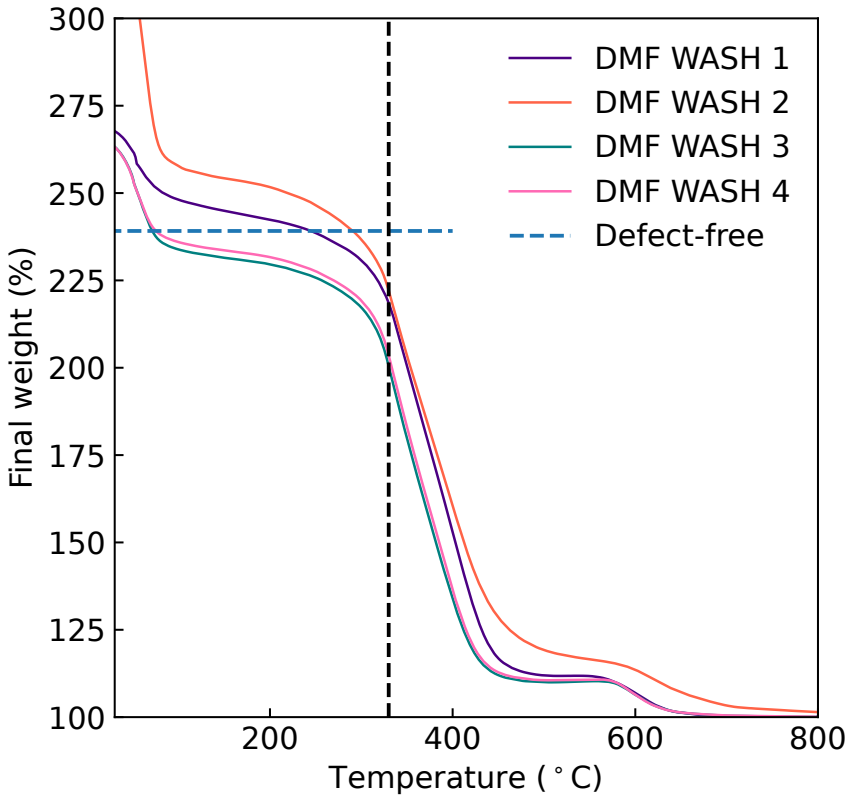

Figure 3.6: TGA of MOFs synthesised in a 2:1 ligand:metal ratio, washed from 1 –4 times in DMF for 2.5 hours.

Fig.3.6 shows that increased mass losses are observed in the samples which have been washed once or twice, compared to those washed three and four times. This mass loss difference is attributed to unreacted ligand in the pore, as this synthesis utilises hyper-stoichiometry of ligand. To ensure all samples are properly removed of unreacted linker, sythesised UiO-66(NH_2) is washed three times according to this procedure.

As modulators are responsible for defect introduction during a synthesis,

these are a possible variable by which the concentration of defects can be controlled. Fig.3.7 shows the structural effects of varying amounts of modulator, using 1, 2, 5 and 10 mL formic acid (with formic acid: Zr ratios of 22:1, 44:1, 110:1 and 220:1 respectively). Powder patterns show very little difference between all of these samples, with all samples being crystalline, phase pure **fcu** UiO-66(NH_2). The sample synthesised with 1 mL formic acid shows an asymmetric peak shape in the *111* reflection, with a high Q tail. This peak shape is sample-dependent, and indicates a stacking disorder within the sample.

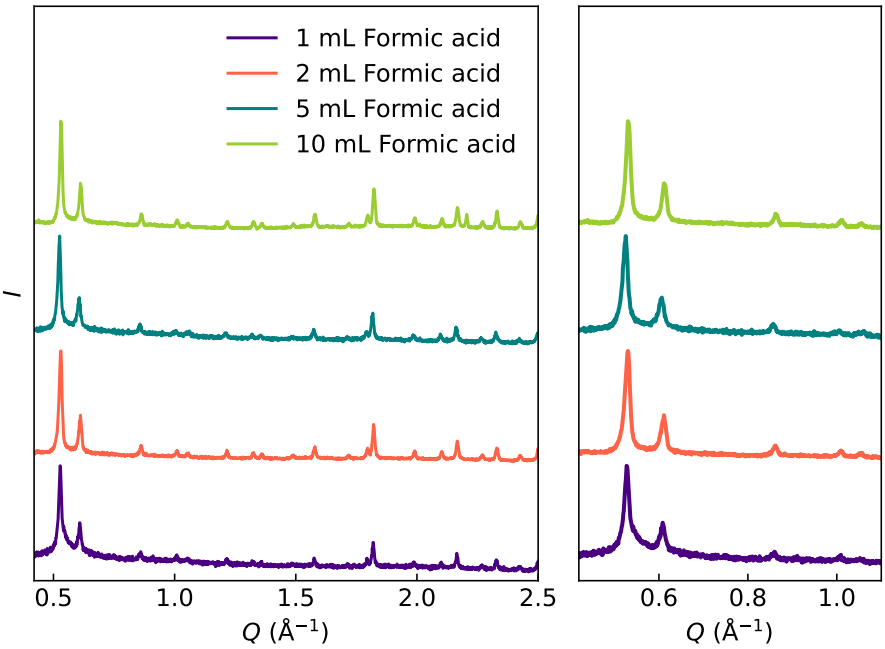

Figure 3.7: PXRD of UiO-66(NH_2) with varied modulator concentrations.

The TGA data for the modulator-controlled syntheses are shown in Fig.3.8. The missing linker concentrations from the 1 mL, 2 mL, 5 mL and 10 mL samples are 6.7 %, 8.3 %, 28.3 % and 32 % respectively. At lower concentrations of modulator, the trend behaves as expected, where increasing the concentration of modulator creates higher defect concentrations.

In these syntheses containing 5 mL and 10 mL formic acid, the volume of formic acid represents very large proportions of the total reaction volume. The effects of larger modulator concentrations causes unexpected defect concentration changes from 5 mL to 10 mL. Such proportions of modulator can act as a solvent in the reaction, changing the reaction properties beyond simply modulation. Formic acid is difficult to dry completely, as it decomposes (generating water) in its pure state, there-

fore by adding large amounts of modulator, water concentrations are also changing, which is a known variable for defects and phase control in UiO-66 synthesis.[51] These reactions are carried out above the boiling point of formic acid (and water), and the headspaces in the reaction vessel are decreased upon adding more modulator, therefore the pressure inside each reaction vessel will be different, which can affect the properties of the MOF greatly. For these reasons, I deemed the control of formic acid content in the reaction to introduce too many independent variables, as such large proportions of formic acid were required to obtain the desired effects.

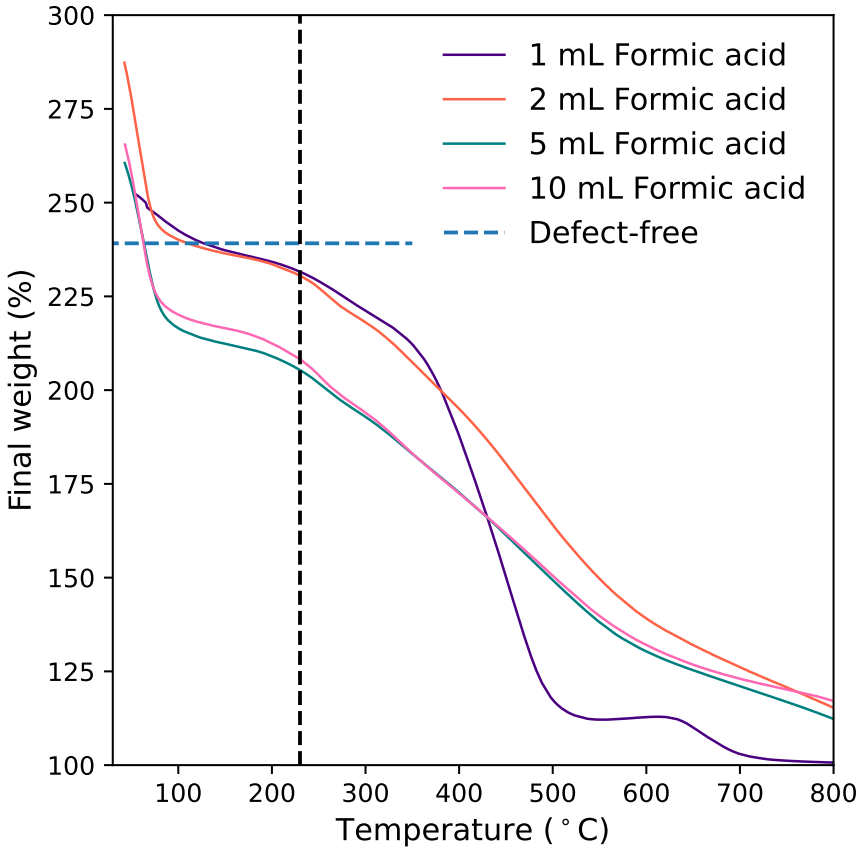

Figure 3.8: TGA of UiO-66(NH_2) with varied modulator concentrations.

3.2.2 Post-synthetic defect generation

Post-synthetic defect engineering was also attempted, using Argon plasma, a process hereafter referred to as 'plasma cleaning'. This technique allows a series of materials with different defect concentrations to be produced from the exact same material. The benefit to plasma

cleaning defect generation is isolating the variable of defect concentration. *De novo* defect introduction can also affect other properties, such as material phase and particle size. Isolating the variable of defect concentration through plasma cleaning allows for optimal investigation of defects impact on photocatalysis.

Due to the surface sensitivity of plasma cleaning, powder samples were not investigated (though they were planned pending development of a new powder stirrer in our plasma cleaning chamber). Instead of powders, UiO-66(NH_2) films were created, by dropcasting the material onto a silicon wafer, and exposed to plasma as a thin film to maximise exposure throughout the whole sample.

Ar plasma defect engineering was performed on UiO-66(NH_2) immobilized onto a Si chip through dropcasting. This allowed for focusing of plasma onto a small surface of a very high aspect ratio. Dropcast material was chosen as the medium for ion bombadment due to the surface sensitivty of the technique. Defect generation on an extremely thin sample allows for bulk analysis which is representative of the defect-generated state, rather than a mixture of pristine MOF and MOF which has been exposed to plasma.

Fig. 3.9 shows the PXRD patterns for UiO-66(NH_2) exposed to 50 W Ar plasma for varying durations, with pictures of each sample present. It is clear that the plasma exposure induces a colour change, rather than turning yellow (which would be expected from removal of linkers), the sample starts to turn brown after longer exposure times, indicating there are additional changes in the MOF beside linker removal. I attempted Pawley refinement of peaks in the PXRD patterns, to develop a better understanding of how ion bombardment effects the MOF, however errors were too high to be useful (Appendix Fig. 6.1).

Plasma-cleaned samples were analyzed through XPS to elucidate any chemical changes caused through plasma exposure. The MOFs which were exposed to plasma cleaning treatment show peaks correspond to Au, which is not present in the sample prior to plasma cleaning. Plasma cleaning occurs inside the same chamber as magnetron sputtering, and while the metal targets are covered, there is a thin layer of sputtered metal on every surface in the chamber. The introduction of these elements during the plasma cleaning process indicates that the Ar plasma is sputtering metals in the chamber, without the electromagnet local-

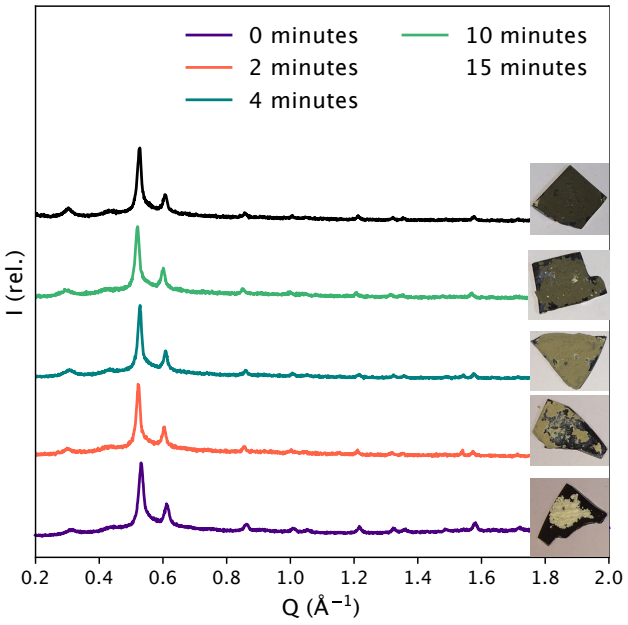

Figure 3.9: PXRD UiO-66(NH_2) (from bottom to top) as-synthesised, and after: 2,4,10 and 15 minutes of plasma exposure at a power of 100 W. Pictures of each sample loaded onto silicon wafers are shown adjacent

ization of the field, large amounts of surface are experiencing plasma exposure. The metals ejected from surfaces near to the MOF powder are being deposited upon the MOF. The introduction of new metals introduces different catalytic properties, and changes the chemical environment of the framework. Deconvolution of defect-specific changes in the MOF from those introduced by metal deposition is impossible, therefore plasma cleaning cannot proceed without a dedicated chamber separate from use in magnetron sputtering. Unfortunately, installation of this chamber was difficult and expensive, therefore I was not able to further research the effect of plasma-induced point defects on UiO-66(NH_2).

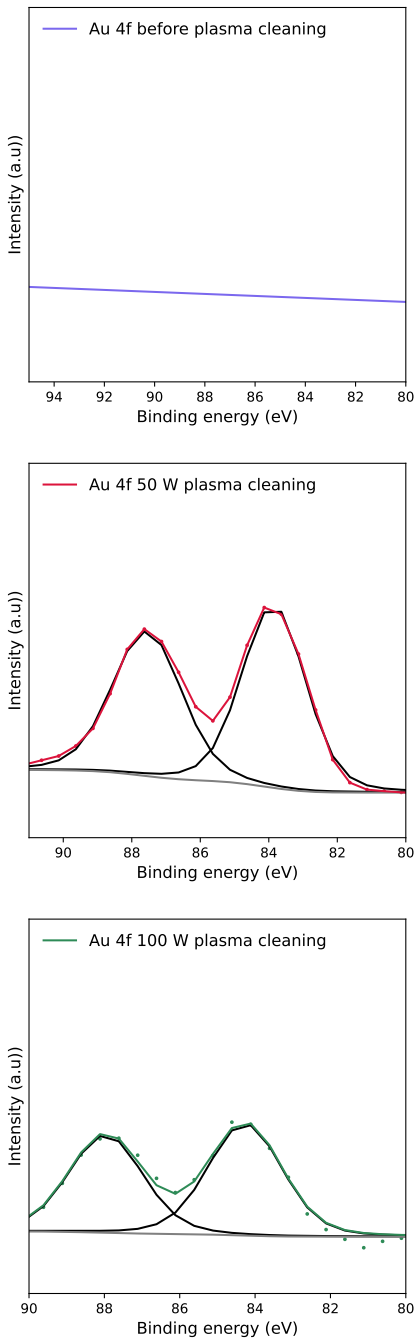

Figure 3.10: Au 4f XPS of UiO-66(NH_2) before exposure to plasma cleaning (top), after 10 minutes of plasma cleaning at 50 W, and after 10 minutes of plasma cleaning at 100 W. Circles correspond to the measured spectrum, and the coloured lines along the measured data correspond to the sum curve of all the components fitted to this data. In this case, the spectrum of the sample before plasma cleaning raw data is plotted as a line, rather than a scatter, as the noise is sparse and the line makes it easier to see. This XPS data shows that plasma cleaning inside a metal chamber can cause sputtering of the surrounding elements, which will effect catalyst performance.

3.2.3 Water-controlled defect series

Firth *et al.*[51] reported that water content in a synthesis can be an important parameter for physical properties of UiO-66, and can be used as an independent variable to dictate the phase of resulting material. Fig.3.11 shows the powder patterns of three UiO-66(NH_2) samples synthesised using water as an independent variable to introduce missing linker defects. These three samples are all phase-pure **fcu**, and higher water content during the synthesis produces broader peaks. The peak broadening was accounted for by Scherrer broadening, and particle size was fit in a Pawley refinement. From refinement of these obtained average crystallite sizes of: 99(1), 32(2) and 15(1) nm for low, med and high defect crystals respectively. The low Q tail for the first peak (111) in the low defect material is attributed to instrumental effects, and is present only in this diffraction pattern due to its increased crystallinity, whereas the med and low defect samples have peak shape much more defined by particle size, therefore the instrumental effects cannot be observed visually. The same peak shapes can be observed in the most crystalline samples from Fig.3.4.

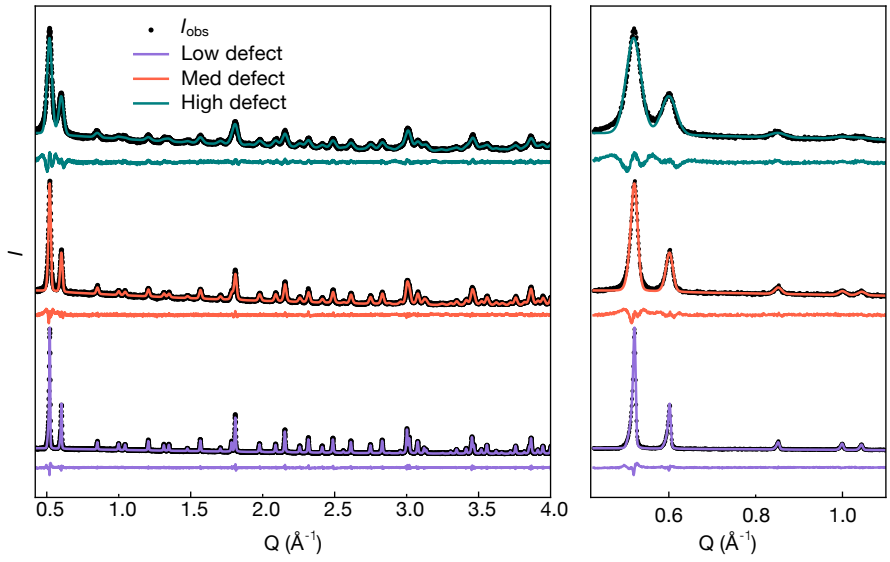

Figure 3.11: PXRD patterns with Pawley refinements of three samples synthesised in varying defect concentrations using water as an independent variable. 0.0 mL water (bottom), 0.1 mL water (middle), 0.2 mL water (top) herein referred to as 'Low defect', 'Med defect' and 'High defect'. Raw data is shown in black, fitted data from Pawley refinements on top, and difference shown below each.

Fit parameters from the Pawley refinement are presented in Table 3.1

The changes in particle size were confirmed with scanning electron mi-

Parameter	Low	Med	High
Crystal system	Cubic	Cubic	Cubic
a (Å)	20.817(1)	20.815(4)	20.808(1)
A (^{o})	90	90	90
Displacement Height	0.016(2)	-0.00721(9)	0.009(2)
Crystallite size	99(1)	32(1)	15(1)
R_{wp}	7.050	6.084	4.962
GOF	1.515	1.276	1.141

Table 3.1: Fit parameters for Pawley refinements of UiO-66(NH2) with different defect concentrations.

croscopy (SEM), and the images are shown in Fig.3.12. The mean UiO-66(NH_2) particle sizes from SEM are 120(10), 45(10) and 15(1) nm for low, med and high defect samples respectively.

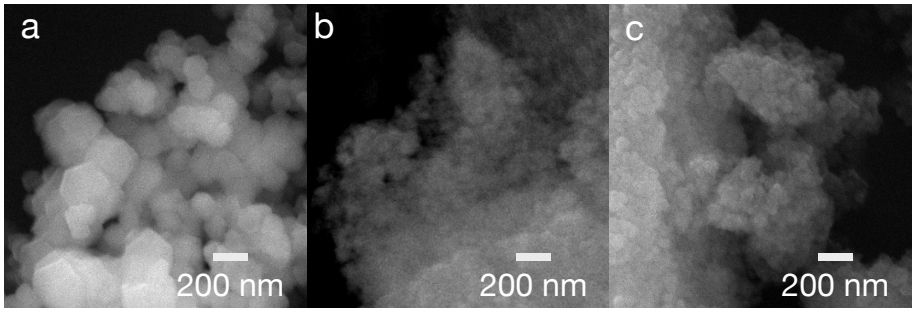

Figure 3.12: SEM images for **low** (a), **med** (b), and **high** (c) defect concentrations of UiO-66(NH_2).

I calculated the defect concentrations for each sample in the defect series using aerobic TGA. TGA plots are shown in Fig. 3.13. All plots are normalised by their final weight, which makes it possible to quantify defect concentrations. The black dashed line relates to the lowest temperature at which surface-adsorbed water has been completely evaporated, where we have an elemental composition of $Zr_6O_4(OH)_4(NH_2BDC)x$ $(OH)_{1-x}(H_2O)_{1-x}$. The inset shows a zoom onto the intercept of data with this temperature, where the vertical lines are their intercepts.

The synthesis controlling water content to incorporate defects provides the desired outcome. This synthesis gives a clear trend: increasing water content in the synthesis incorporates more missing linker defects to the metal organic framework while remaining phase pure. This synthetic procedure was chosen to investigate catalytic properties and the effects on defects on Pt catalysts. Herein, these samples are referred to as 'low defect', 'med defect' and 'high defect', and any further reference to a 'defect series' corresponds to this series of products.

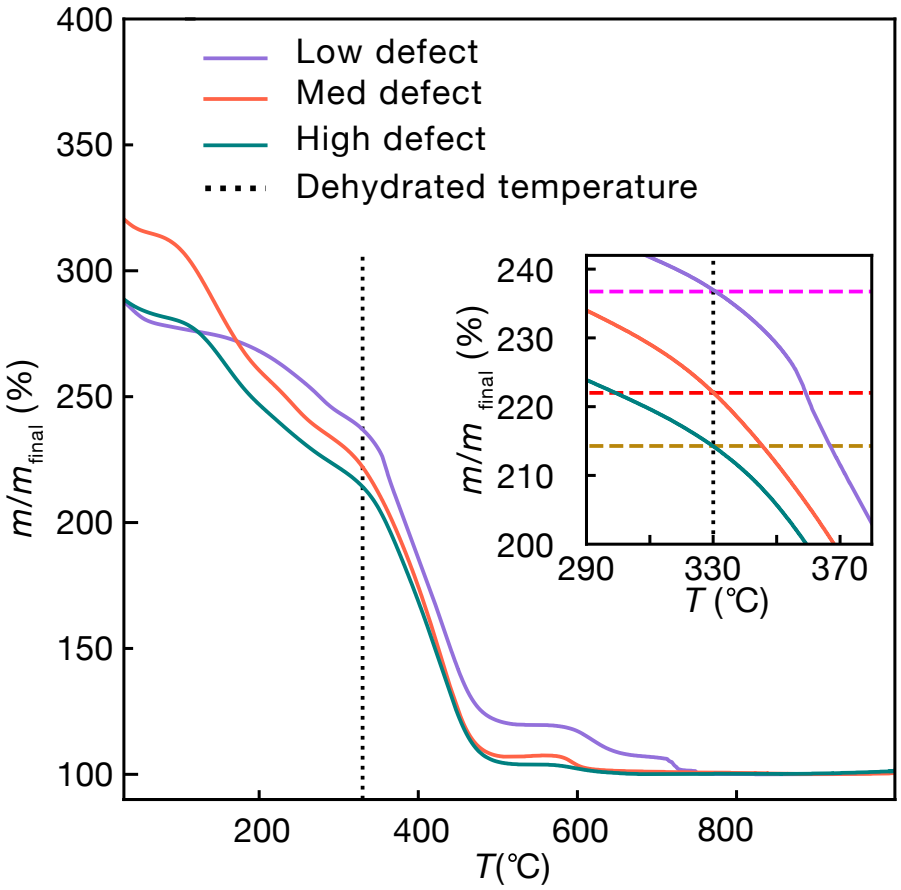

Figure 3.13: TGA measurements for **low** (a), **med** (b), and **high** (c) defect concentrations of UiO-66(NH_2).

The 'dehydrated temperature' is important to quantify, as we require precise mass losses of linker combustion to calculate the stoichiometry of linker:cluster and thus defect concentration. Any water-related mass losses must be discounted, as they would interfere with the defect calculation. Any mass losses before 330°C are non-structural, and mainly water. Evidence of this is shown in Fig.3.14, which shows the TGA gradient as a function of temperature. From RT-330 °C, mass loss is at a slow rate, indicated by the small negative gradient. However, at 330 °C, the gradient becomes more negative (the method to derive this temperature precisely is shown in Fig. 3.14), indicating a new change, which is the structural decomposition. I used the highest temperature before structural decomposition began as the 'dehydrated' temperature, at which the mass is used to calculate defect concentrations. For calculations, we use an elemental composition of $Zr_6O_4(OH)_4(NH_2BDC)x$ for the material at 330 °C.

After water removal, the next mass loss corresponds to the loss of clus-

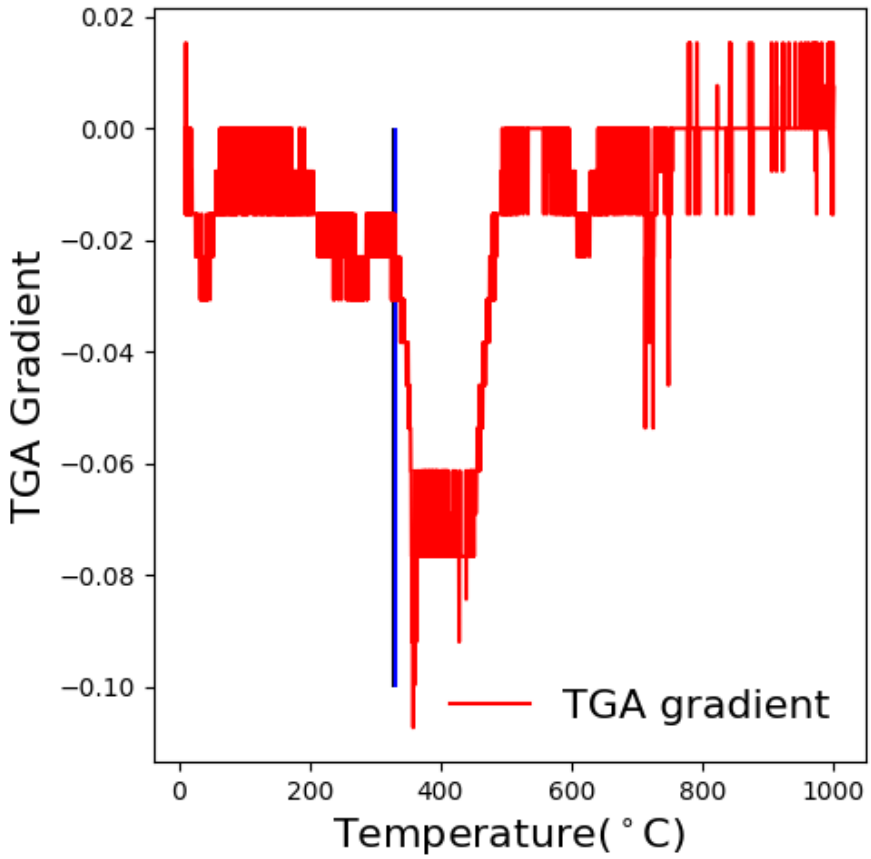

Figure 3.14: The derivative of TGA measurements for the low defect sample as a function of temperature. Increased mass losses after 330 ^{o}C (blue line) indicate this is the temperature at which linker combustion begins for this sample.

ter water, with the following reaction: $Zr_6O_4(OH)_4(NH_2BDC)x \longrightarrow Zr_6O_6(NH_2BDC)x + 2\,H_2O$. In UiO-66, this can be observed as a discrete step in TGA, before ligand combustion, however in UiO-66(NH_2) the ligands are combusted at lower temperatures, so the two steps are observed simultaneously. Above ~350 °C, the lost mass corresponds to combustion of the organic linker. From the knowledge that at the conclusion of a TGA measurment, the only remaining species is ZrO_2, this allows determination of the cluster:linker ratio, and any deviations from the stoichiometric 1:1 ratio can be detected Fig.3.13.[51,54]

Defect calculations are performed as follows:

I assume that:[66]

- All Zr present is in the zirconium-oxo cluster species, $Zr_6O_4(OH)_4$. From pair distribution function data shown later, this is confirmed.
- All defects are capped by one hydroxide and one water.

The material at 1000 °C is ZrO_2, where Mr ZrO_2 = 123 gmol^{-1}.
The material at 330 °C is $Zr_6O_4(OH)_4(NH_2BDC)x\ (OH)_{1-x}(H_2O)_{1-x}$.The hydroxide and water molecules are capping ligands, observed to coordinate at the nodes adjacent to a missing linker defect.

The Mr (relative mass) change of a defect introduction is

$$(\mathrm{Mr_{H2O}} + \mathrm{Mr_{OH}}) - \mathrm{Mr_{linker}}.$$

I use 'adjacent vacancies' (AV) in this calculation, which corresponds to the number of linkers, on average, missing adjacent to a cluster. A non-defective material has six adjacent linkers to each cluster, therefore adjacent vacancies=0. An adjacent vacancy number of one means a total defect fraction of $\frac{1}{6}$.

We can calculate the $\mathrm{Mr}_{defectiveMOF}$ through:

$$\mathrm{Mr_{defective\ MOF}} = [(6 - \mathrm{AV}) \times \mathrm{Mr_{linker}}] + \mathrm{Mr_{cluster}} + \mathrm{AV} \times \mathrm{MrOH} + Mr_{\mathrm{H2O}} \tag{3.1}$$

This $\mathrm{Mr}_{defectiveMOF}$ can be converted to the units of normalised y axis through:

$$\text{Final. wt\%} = (\mathrm{Mr}_{defectiveMOF}/6)/\mathrm{Mr}_{ZrO_2} \tag{3.2}$$

By intercepting the data at 330 °C to obtain the defective final wt. % , we can solve for Mr in (3.3):

$$\mathrm{Mr}_{defectiveMOF} = \text{Final wt.\%} \times \mathrm{Mr}_{ZrO_2} \times 6. \tag{3.3}$$

And by solving (3.1) for AV, we can calulate defect concentration using the previously calculated $\mathrm{Mr}_{defectiveMOF}$:

$$\mathrm{AV} = \frac{\mathrm{Mr}_{DefectiveMOF} - \mathrm{Mr}_{Cluster} - 6\mathrm{Mr}_{linker}}{\mathrm{Mr}_{OH} + \mathrm{Mr}_{H_2O} - \mathrm{Mr}_{linker}}. \tag{3.4}$$

and

$$\text{Defect concentration}(\%) = (AV/6) \times 100\%. \tag{3.5}$$

From these defect calculations, we obtain missing linker concentrations of 0.5(5), 13.3(8) and 20.0(6) % for low, medium and high defect samples respectively. Errors were calculated by assuming that the largest source of error is found in the calculation of dry mass. By over-estimating an error of ± 10 °C in calculating the true temperature at which all moisture is lost, the defect calculations were repeated, and the largest error was used for each sample. This provides clear evidence that introducing water to these synthesis conditions increses the concentration of missing linker defects. A summary of physical properties from the addition of water to the synthesis can be seen in Fig.3.15.

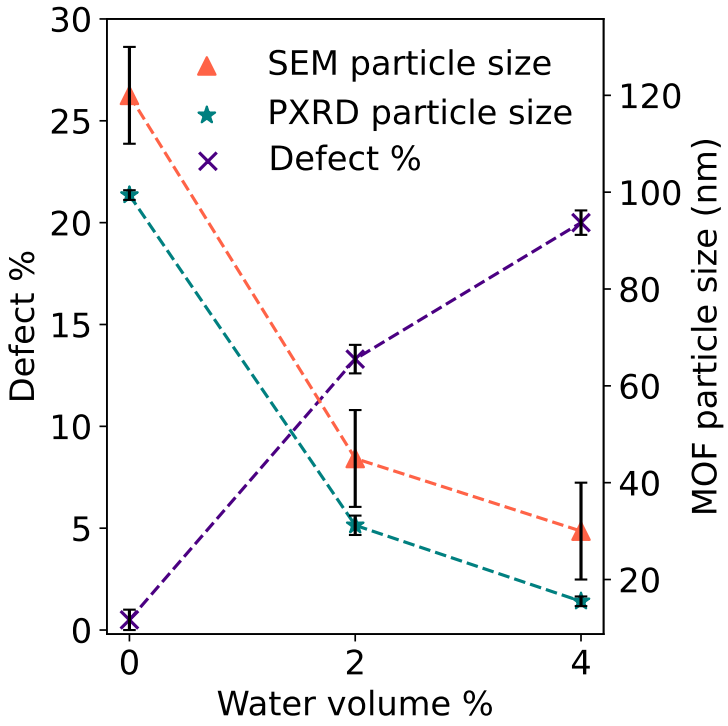

Figure 3.15: A summary of the physical properties of UiO-66(NH_2) with increasing water content in the synthesis reaction.

I then deposited Pt onto each samples in the defect series, using magnetron sputtering, with an aim to achieve ~2.5 wt. % Pt loading. This loading was chosen to generate nanoparticles around 2 nm, which are much easier to image using TEM than smaller, sub-nanometer particles, as TEM is traditionally the technique used to measure catalyst particle sintering. Platinum weight loading was measured using inductively coupled plasma optical emission spectroscopy (ICP-OES). Low defect contains 2.47(5) wt. /% Pt, med defect contains 2.26(3) wt. /% Pt and high defect contains 3.09(4) wt. /% Pt.

Sample	Pt content (wt. %)
Low defect	2.47(5)
Med defect	2.26(3)
High defect	3.09(4)

Table 3.2: Pt loading for each catalyst in the defect series.

Fig. 3.16 shows DRS UV-vis spectra for each Pt @ UiO-66(NH_2) catalyst, with the UV lamp emission profile. Each sample has a strong absorption band from 300 - 400 nm, showing that the sample will absorb energy under UV emission.

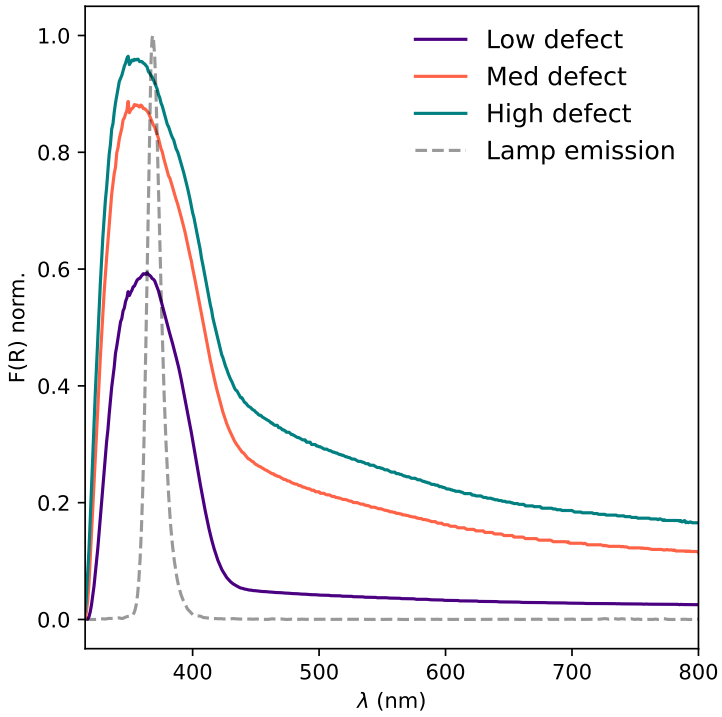

Figure 3.16: Diffuse reflectance UV-vis spectra of the low (purple), med (orange) and high (teal) defect samples after deposition with Pt. The emission profile for the UV lamp used in catalysis is shown in grey.

All Pt @ UiO-66(NH_2) samples were imaged using TEM, and the images are shown in Fig. 3.17. The platinum nanoparticles show a clear tendency to form at the surface of the MOF, and there appear to be none observed below the surface (which has been observed in similar samples).[81] The low electron dose used allows the framework to maintain crystallinity, as observed in all three images. The mean platinum particle sizes are 2.1(2) nm, 2.3(2) nm and 1.8(2) nm for low, med and high defect concentrations respectively. These mean particle sizes indicate that defects do not affect the physical characteristics of directly de-

posited Pt nanoparticles. The particle size distributions are also shown in this figure, where the distribution is fit to a lognormal distribution.

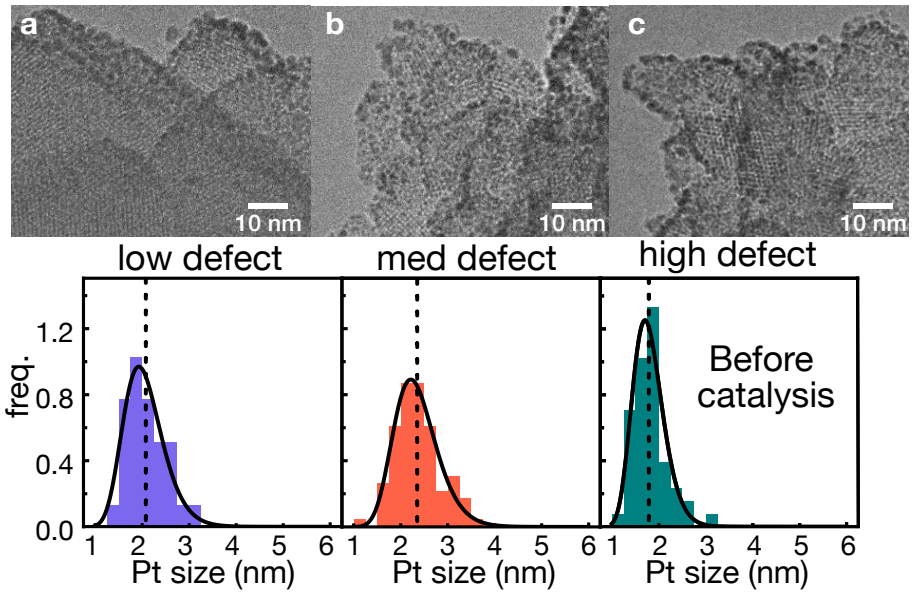

Figure 3.17: TEM images of Pt-deposited low (a), med (b) and high (c) defect concentrations of UiO-66(NH_2) with histograms of particle diameters fit to a lognormal distribution.

To complement the TEM imaging, I also utilize pair distribution function to understand the nanoparticle structure through short range ordering. This technique complements TEM by assessing the structure of Pt throughout the whole sample, rather than localised areas which can be imaged. The techniques are complementary because of the different type of information given by each: TEM probes specific sizes, and allows us to generate histograms of Pt particle sizes, understanding their distribution. Whereas PDF gives an averaged understanding across the whole sample, it is diffraction based, and informs on Pt nanoparticles embedded within MOF particles aswell as those on the surface. Where TEM of these samples presents beam-sensitivity issues, and contrast from the support hiding certain features, PDF can explore without these concerns. For this work it is important to utilise information from both techniques to create an accurate representation of the sample.

PDF of UiO-66(NH_2) was first measured without any Pt co-catalyst present (Fig. 3.18). These analyses are important for two reasons: to gain a better understanding of the underlying MOF in catalyst samples, and to perform subtractions from later measurements to isolate Pt-related correlations. The peak around 1 Å should be ignored, as this is an artefact from measurement, which is present in all PDF data, and

is removed by fitting. Differences between the PDF for each sample are minor, defective samples show slighly broader peaks than the low defect sample at higher distances (> 12), which is expected from more disordered materials.

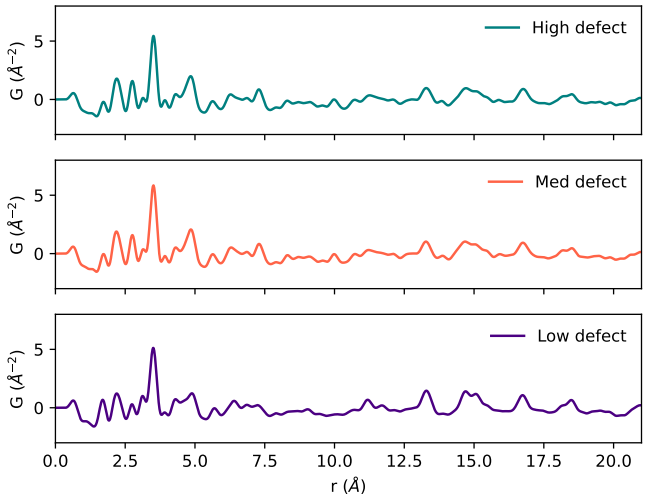

Figure 3.18: PDF measurements for the low, med and high defect samples before Pt deposition

I did not conduct refinements for PDF data for UiO-66(NH_2), as the materials show different defect concentrations and different amounts of disorder. PDF is much more sensitive than PXRD to disorder, as it utilises all X-ray scattering, gaining large amounts of information from diffuse regions and combining this information from that yielded from Bragg peaks. Crystallographic information files (.cifs)for UiO-66 structures represent perfect structures, and there are no generated crystal structures of defective UiO-66 (to my knowledge). Each structure would require a different a different .cif for fitting, and we would be fitting to a speculated structure, where the strain and bond angles have not been properly characterised (therefore there is no guarantee that the calculated data is correct). Fitting the UiO-66(NH_2) and Pt nanoparticles as a multi-phase refinement would be the ideal route, however due to the difficulties of fitting the UiO-66(NH_2) we I instead opt to perform subtractions.

After measuring PDF of the underlying framework, I then analysed the Pt-deposited UiO-66(NH_2) using the same analytic parameters (Fig. 3.19). PDF of Pt-deposited materials show very little difference to those without Pt deposition, due to the very low Pt loading on the sample.

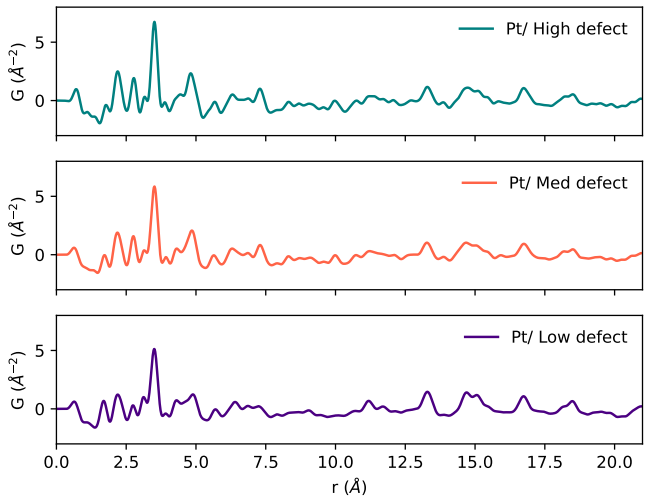

Figure 3.19: PDF measurements for the low, med and high defect samples after Pt deposition

Pair distribution function subtractions were implemented to isolate the Pt-related correlations from the Pt/UiO-66(NH_2). In these subtractions, the Pt/UiO-66(NH_2) PDFs were multiplied by a coefficient, x before subtracting the PDF of UiO-66(NH_2). Fig.3.20 shows the PDF with varying magnitudes of x, in which figure I aim to optimise the magnitude of x to remove all MOF correlations from the resulting subtraction. I use the Zr –Zr intracluster correlation within the zirconium-oxo clusters (at 3.5 Å) as a reference peak to conclude the optimal value of x. As an intracluster correlation, it is subject to the least variation between samples (within the defect series or after Pt deposition), and Zr is strongly X-ray scattering, therefore this common correlation is the strongest correlation in each PDF. From the subtractions in Fig.3.20, I conclude that the optimal subtraction to isolate Pt correlations is where x=1.15, therefore I use the equation:

$$\mathrm{PDF_{Pt}} = 1.15\mathrm{PDF_{Pt/MOF}} - \mathrm{PDF_{MOF}} \tag{3.6}$$

for any PDF subtractions in this chapter.

The subtracted PDFs are shown in Fig.3.21. Pt –Pt correlations of the $Fm\bar{3}m$ structure are shown in grey dashed lines, which clearly align with the remaining correlations in each PDF. These alignments can be observed clearly up to around 10 Å. The broad features observed beyond this distance relate to longer-range ordering imperfections in the

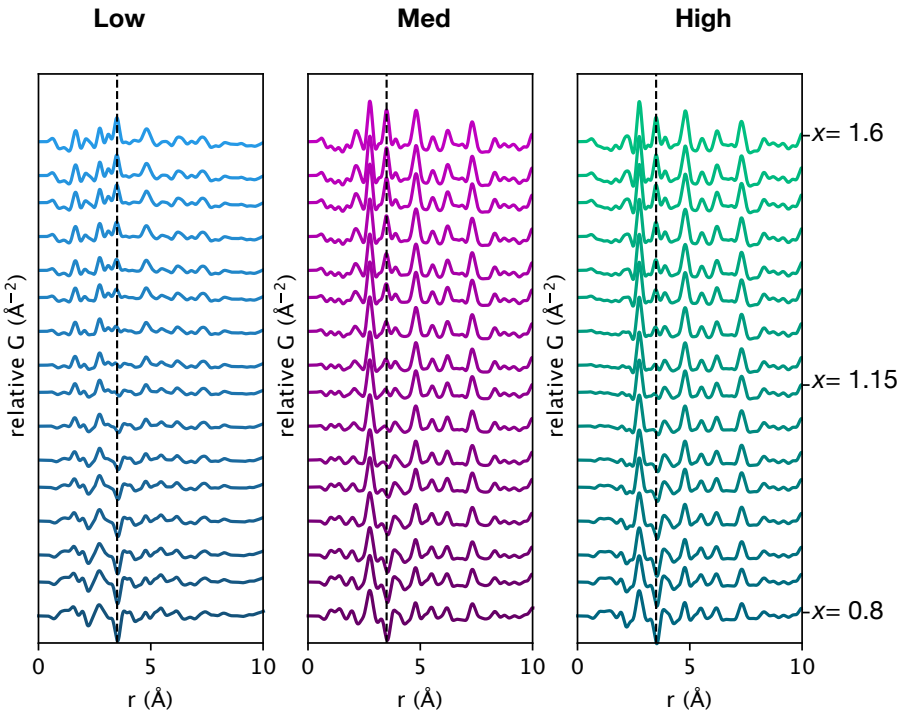

Figure 3.20: Subtracting the PDF of non-deposited MOF from Pt/UiO-66(NH_2) of the respective in the defect series, where the PDF of Pt/UiO-66(NH_2) is multiplied by a varying coefficient, *x*. The intracluster Zr –Zr correlation is shown with the black dashed line.

subtractions, as these correlations are more susceptible to change between samples. The low defect sample clearly shows correlations of a much lower magnitude than the other two samples in the defect series, despite having the comparable Pt contents. All three samples show a clear decay in the intensity of Pt-Pt correlations as a function of r, which is characteristic of nanoparticles.

I fit the subtracted PDFs using TOPAS academic v6.[95] The fitting uses the γ_0 function, a fit parameter which makes possible quantification of nanoparticle diameter, from the decaying peak intensity as r increases.[104] Intensity of correlations follows the function

$$\gamma_0 = 1 - \frac{3}{2} \times \frac{r}{d} + \frac{1}{2} \times \frac{r^3}{d}. \tag{3.7}$$

Fits also incorporated r-dependent broadening of Pt-Pt correlations. PDF fits yielded Pt crystallites of 16.7 ± 1.0, 18.6 ± 0.6 and 18.9 ± 0.5 for the low, med and high defect materials respectively. This is not necessarily the size of the whole particle, rather the metallic Pt component.

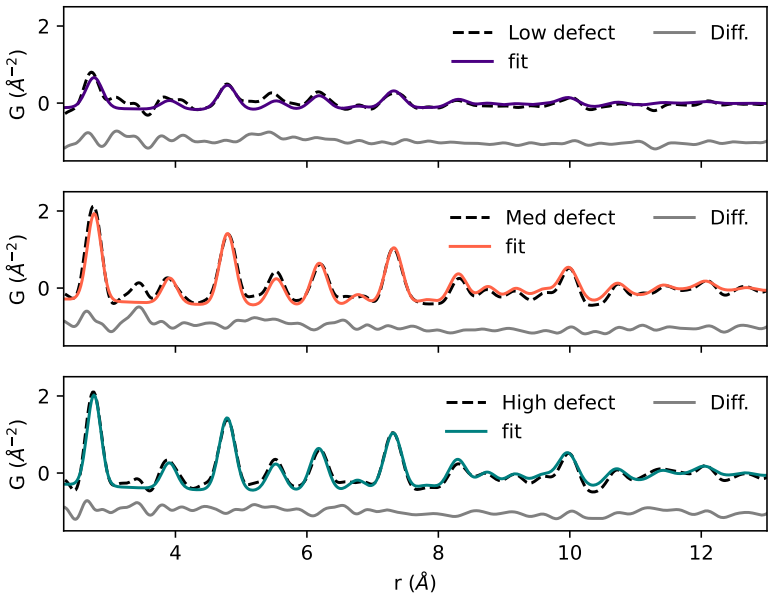

Figure 3.21: Fitting the subtracted data (black) to platinum, using the γ_0 function and r-dependent broadening to account for crystallite size.

XPS spectra for Pt in as-sputtered samples is shown in Fig. 3.22. Pt is the active site for catalytic hydrogen generation, and its chemical environment is important to describe both catalyst stability and activity. The intensity of Pt peaks in the med defect material are lower than those in the low and high defect materials. Inter-sample intensity differences in this analysis are discounted from any physical meaning. ICP-OES data provides precise Pt loadings across the whole material, whereas XPS selectively probes the surface of a small amount of sample. The low Pt signal in med defect likely relates to an area which is sparsely deposited with Pt in magnetron sputtering, likely caused by poor powder mixing during deposition. In the case of Pt, probing a sparse region *could* provide a poor representation of the whole sample (as sparse deposition can lead to smaller Pt particles), however in this case Pt XPS behaves normally according to the other samples. All Pt spectra indicate two oxidation states: Pt^0 and $Pt^{\delta+}$, these two components correspond to the core and surface of nanoparticles respectively. The formal oxidation state is not given for the $Pt^{\delta+}$ as the peaks do not align with expected values from standards, and a nanoparticle surface does not behave identically to a bulk material such as PtO_2.

N1s peaks do not change position, nor are additional peaks observed in any spectra. C1s spectra are composed of C-C bonds (at 284.8 eV by

calibration), C-O bonds at 285.9 eV and O-C=O bonds at 288.8 eV. As the defects are whole linker vacancies, no significant changes in XPS are observed when introducing more defects to the structure. Very small $\pi - \pi^*$ satellite peaks are fit in the defect-containing samples, where none were detected in the low defect material, which indicates extended delocalisation of electrons. Band gap calculations in defective UiO-66 show reductions in band gap, which would account for the increased π delocalisation upon introduction of defects. In the O1s XPS, Zr-O-Zr peak (which is the lowest energy) is 530.59, 530.92 and 530.70 in the low, med and high defect materials respectively.Despite introduction of defects, the μ_2 O/OH do not have different electron densities across samples. These sites are anticipated to contribute significantly to catalysis, as they can adsorb water for hydrogen generation. Upon introducing defects, a second Zr environment is introduced at higher BE, caused by hydroxyl binding or a Pt-Zr interface of NPs binding at defect sites withdrawing electron density(or likely both).

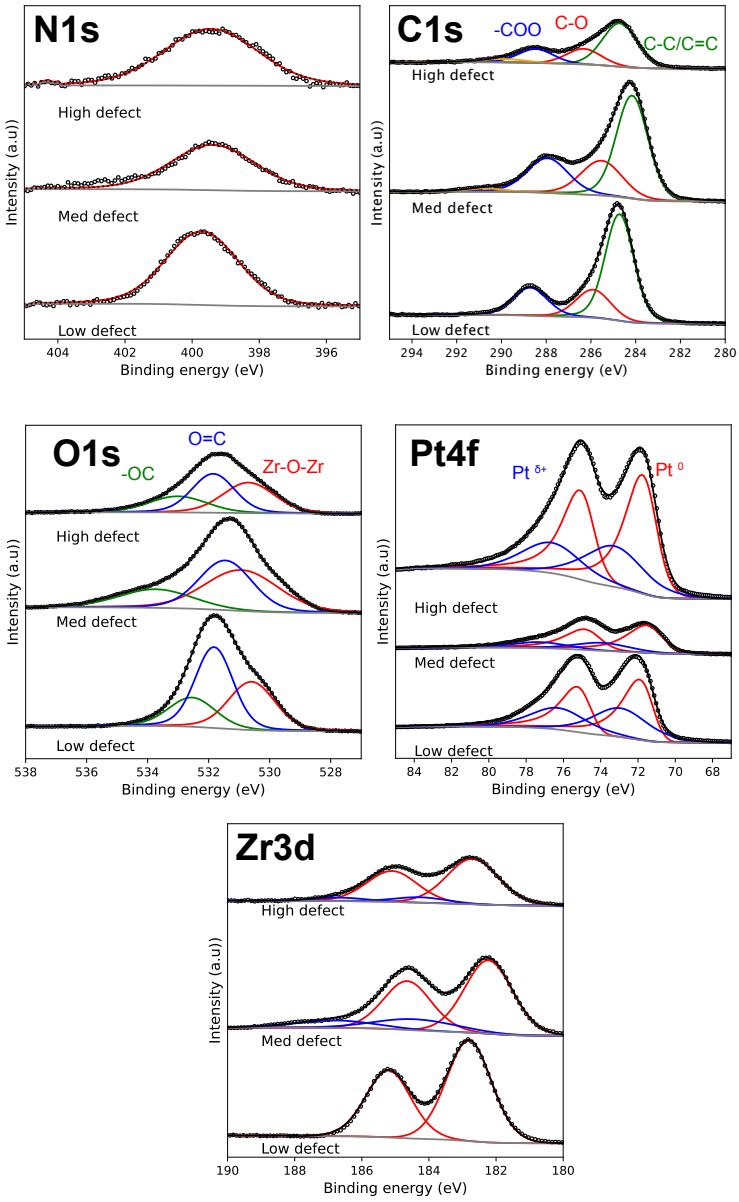

Figure 3.22: XPS spectra for each defect concentration of Pt@UiO-66(NH_2) before catalysis. Circles correspond to the measured spectrum, and the black lines along the measured data correspond to the sum curve of all the components fitted to this data. Individual components of the data are shown in coloured lines, and spin-coupled peaks are the same colour.

I then investigate each of these materials for their efficacy as photocatalysts for H_2 generation. These catalysts are used in thin films to maximise light exposure (this is discussed in the chapter *Photocatalytic reactor design and optimisation*). I created a thin film of mean thickness 0.8 mm by suspending nanoparticulate catalyst in methanol and sonicating for dispersion. This suspension is then dropcast onto a 15 x 25 mm glass slide, left to evaporate and repeated once with any remaining particles from the suspension. This yields a thin, even film across the glass slide with minimal clumps and good repeatability. The film is stable when immersed in 10 % methanol in water.

I assess catalytic activity of the catalyst systems in photocatalytoc hydrogen generation by immersing the thin films in a solution of water with 10% methanol, where methanol is present as an electron donor. The system is then illuminated with a 365 nm Evolchem UV Lamp, and the generation of H_2 assessed with online GC where injections were taken every 14 minutes. Using calibration curves, the output from the GC-TCD was converted to a concentration present in the reactor headspace. Concentrations of hydrogen in the headspace were converted to rates of production using equation (3.8):

$$\text{Rate of } H_2 \text{ generation} = \frac{\text{hydrogen conc.} \times \text{flow rate}}{\text{headspace}} \tag{3.8}$$

Fig. 3.23 shows the rates of hydrogen generation for catalysts of each defect concentration. Error bars are included after 25 injections, where the rates of hydrogen generation begin to plateau.

This figure shows that lower defect concentrations produce higher activity for hydrogen generation, contrary to all reported literature.

After catalysis, the framework remains, and no effects of structural decomposition can be noted from PXRD analysis. Fig. 3.24 shows the PXRD patterns of a UiO-66(NH_2) sample before and after 2.5 hours of photocatalysis under reaction conditions. Peaks do not become more broad, nor are any peaks generated or lost from the catalysis. Signal to noise is much lower in the spent catalyst, however this is attributed to the amount of sample. Catalysis was studied with 3 mg of catalyst, therefore a thin layer of sample must be created and analyzed, and the signal generated is much weaker than that of a PXRD pattern with sufficient material. Due to the limitations in sample quantity affecting

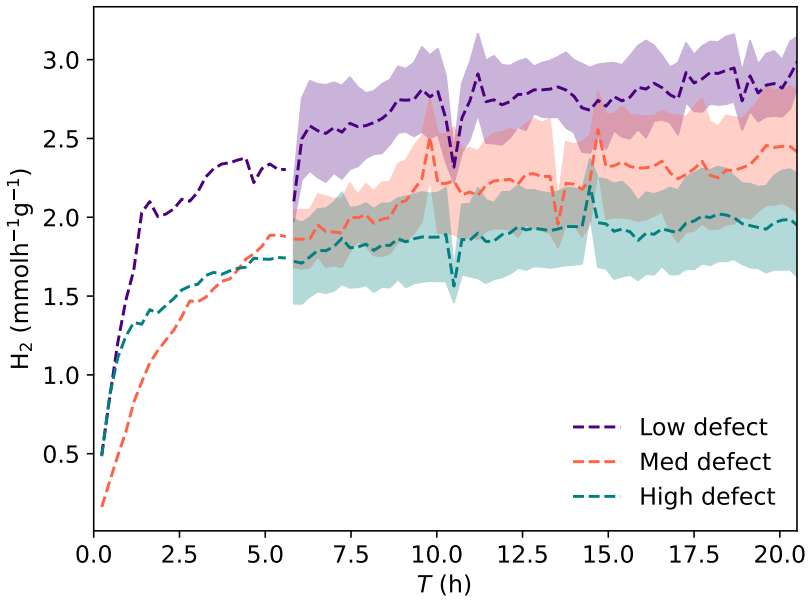

Figure 3.23: Rates of hydrogen generation for the platinum-deposited defect series under 365 nm UV lamp irradiation.

quality of data, I did not perform Pawley refinements on the MOF after catalysis.

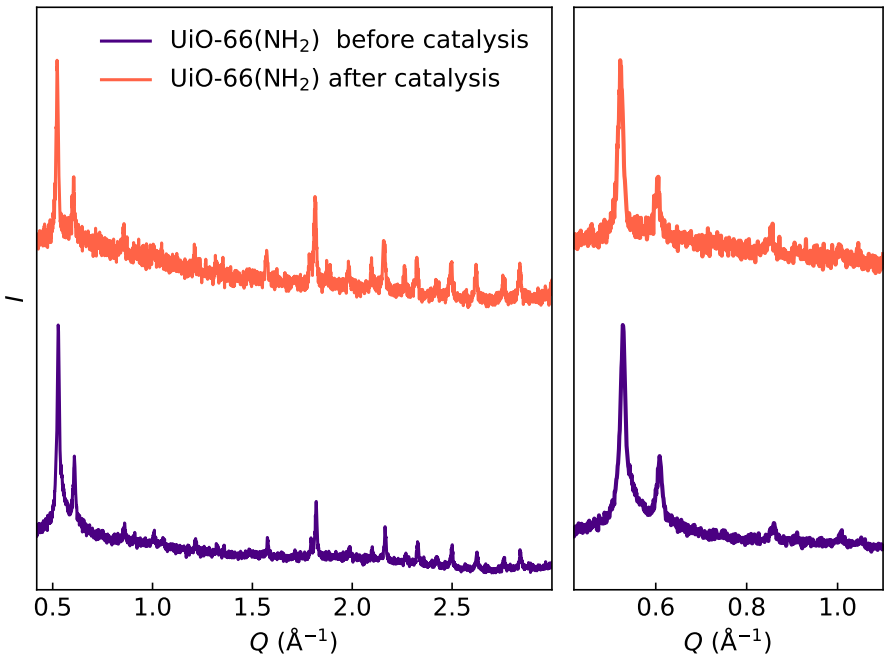

Figure 3.24: Pt/ UiO-66(NH_2) before and after catalysis. The material is stable under reaction conditions, as indicated by the unchanged peak FWHM and presence of the same peaks both before and after catalysis.

After catalysis, I conducted analysis of the catalysts to understand the sintering and character of Pt nanoparticles during catalysis.

TEM images of catalysts in as-synthesised form, after 2.5 hours and after 24 hours of catalysis are shown in Fig.3.25. During the course of catalysis, it can be observed that platinum particles are mobile, and have an affinity for surface binding in all three defect concentrations, as all samples show a Pt migration towards the surface. There are almost no visible nanoparticles over 5 nm from the surface for any of the defect concentrations after 24 hours.

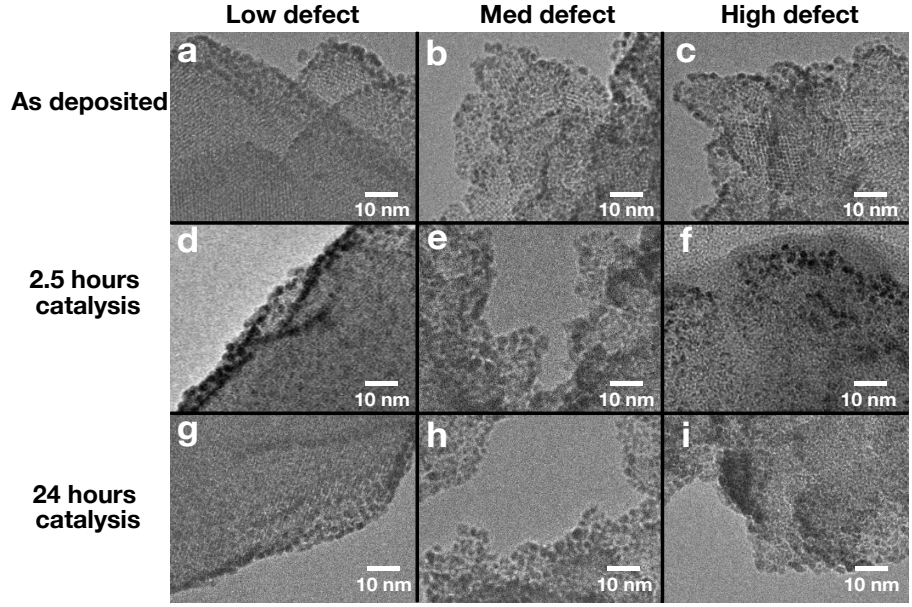

Figure 3.25: TEM of the Pt-deposited UiO-66(NH_2) defect series as-deposited, after 2.5 hours and 24 hours of catalysis.

The nanoparticle size fitting for each sample gave the particle size distributions shown in Fig.3.26. Mean particle diameters obtained from fitting the lognormal distributions of particle size distributions are shown in Table 3.3.

Sample	As- synthesised d	2.5 hour d	24 hour d
Low defect	2.1(2)	3.0(2)	2.6(3)
Med defect	2.3(3)	2.6(3)	2.6(1)
High defect	1.8(2)	2.1(1)	2.2(1)

Table 3.3: Pt nanoparticle sizes (nm) before and after catalysis

All samples show Pt particle growth in the first 2.5 h of catalysis, where the defective samples show a much increased stability. In the low-defect material, Pt particles show growth of 0.9 nm, whereas in the med- and high-defect samples the increase is 0.3 nm each. This indicates that defect sites, as expected, are anchoring nanoparticles, reducing mobility

and reducing sintering. After 24 hours, the Pt particles on low and med defect materials show no changes from those measured after 2.5 h within error, demonstrating the efficacy of missing linker defects on imparting stability to deposited Pt. Pt particles on low defect materials shows a reduction in particle size of 0.4 nm in mean particle diameter between 2.5 h and 24 h.

Particle size distribution measurements in the low defect material from 2.5 h to 24 h after catalysis show a large increase in the proportion of Pt nanoparticles below 2 nm, and relative increases in the 2.75 - 3.00 nm range. Ostwald ripening sintering mechanics can explain the increased concentration of Pt nanoparticles below 2 nm, where smaller Pt particles transfer adatoms to other larger particles.[105] This mean particle size decrease cannot be accounted for through Oswald ripening, however, as this does not create a mean smaller particle size. The mean decrease in particle size could be accounted for by leaching of Pt into solution during catalysis, however stability towards leaching was not measured in this thesis.

In TEM particle size measurements, it is important to be aware of bias in both the process of image capturing and particle size measurements. Particularly in this material, where contrast is poor and small nanoparticles are poorly resolved. To reduce bias as much as possible we took a few measures: TEM imaging was kindly carried out by a colleague at the University of Nottingham, particle sizing was measured using line profiles which remove subjectivity from start and end points, and measurement outputs were hidden during measurement.

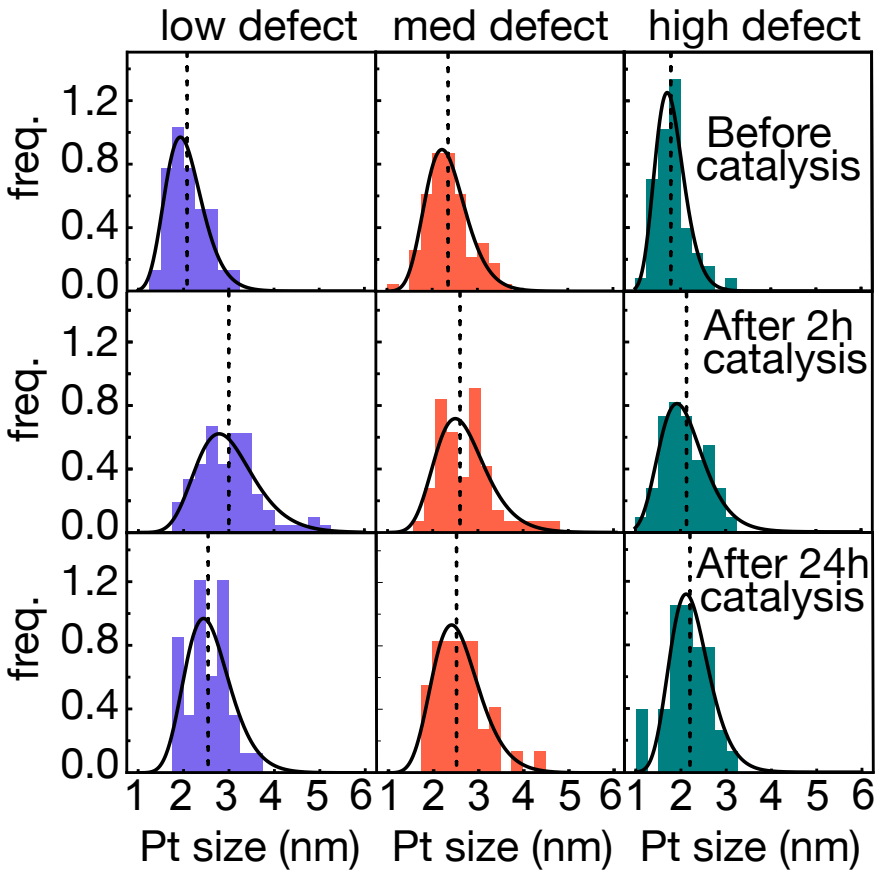

Figure 3.26: Histograms showing the relative frequency of measured nanoparticle sizes in each sample. These histograms are fit to a lognormal distribution, from which the mean particle size can be calculated.

Pair distribution function of the Pt @ UiO-66(NH_2) was measured after 2.5 and 24 hours of catalysis, shown in Figures 3.27 and 3.28 respectively. The PDF for each sample before photocatalysis is plotted against each measurement for comparison. The PDF of the high defect material after 2.5 h was measured with the beam centered incorrectly, measuring almost exclusively the glass capillary instead of the MOF inside, therefore this data does not provide any useful information. The PDF data shows that MOF structure remains broadly unchanged from before exposure to catalysis (the PDF of which is shown in grey for the material of each defect concentration.)

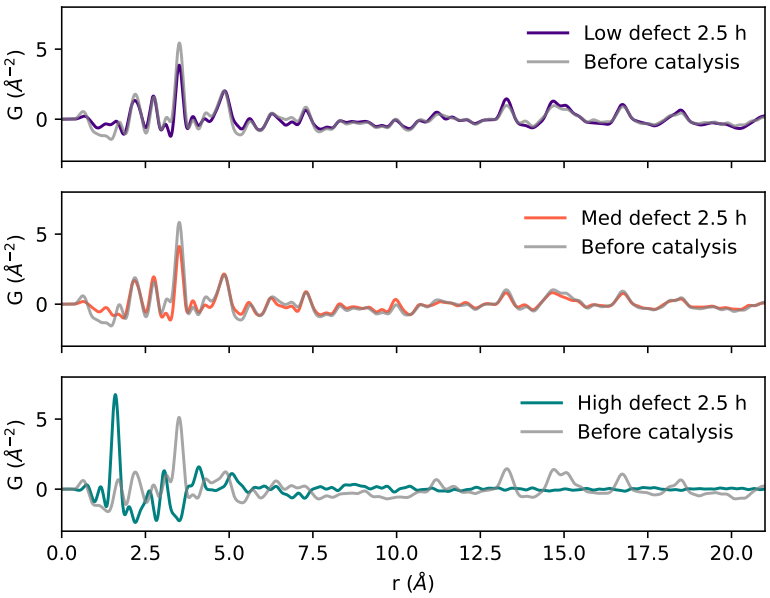

Figure 3.27: PDF analysis of each catalyst in the defect series after 2.5 hours of photocatalysis. The PDF of the high defect material is erroneous, caused by beam centering on the capillary instead of the MOF inside.

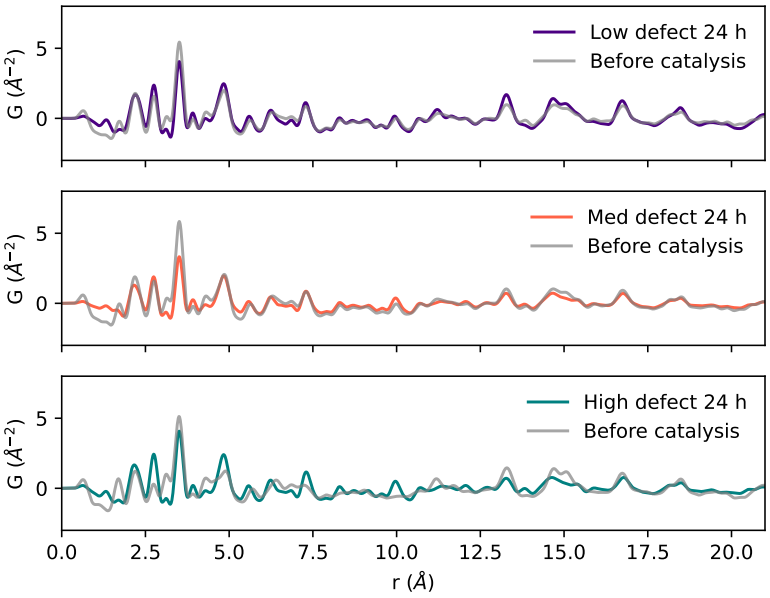

Figure 3.28: PDF analysis of each catalyst in the defect series after 24 hours of photocatalysis.

A d-PDF was generated for each measurement by subtracting the PDF signal of UiO-66(NH_2) for each defect concentration. Subtractions were normalised according to the Zr-Zr intracluster bond at 3.5 Å, and calculations of this subtraction can be seen in the appendix (Fig. 6.10).

Because the PDF of high defect material was measured incorrectly, this is excluded from subtractions. MOF contributions subtracted from PDF of Pt@UiO-66(NH_2) after 2.5 hours are show in Fig. 3.29.

MOF contributions subtracted from PDF of Pt@UiO-66(NH_2) after 24 hours are show in Fig. 3.30.

As these materials were exposed to catalysis (and were approximately 18 months older when analysed by PDF after catalysis), the d-PDF shows more 'noise' beyond Pt-Pt correlations. While not reported in literature, it is noted that the colour of UiO-66(NH_2) slowly changes to a darker yellow over time under air. I speculate that this change is related to NH_2 oxidation, as UiO-66 exhibits no such changes, though this was not investigated nor has this been reported elsewhere. There are very large negative peaks, which indicate an imperfect subtraction rather than physical changes. Fits were performed from 3.6 Å to negate large amounts of subtraction error. The Pt crystallite sizes calculated using the γ_0 function for each sample are shown in Table 3.4. These crystallites are smaller than those measured in TEM, as nanoparticle outer layer is not Pt^0, and therefore does not contribute to the Pt-Pt correlations. The size of Pt crystallites changes very little when a sample is exposed to catalysis, whereas when measured in TEM the particles change size much more. This indicates that the sintering of particles is likely the $Pt^{\delta+}$ surface getting thicker.

Sample	Pt d before cat. (nm)	Pt d 2.5 h (nm)	Pt d 24 h (nm)
Low	1.7(10)	1.7(8)	1.6(4)
Med	1.9(6)	2.0(8)	2.1(12)
High	1.9(5)	NA	2.0(6)

Table 3.4: Mean metallic Pt crystallite sizes in as-sputtered Pt@UiO-66(NH_2), after 2.5 and 24 hours photocatalysis. These values are measured by PDF the d-PDF fitting using γ_0 function.

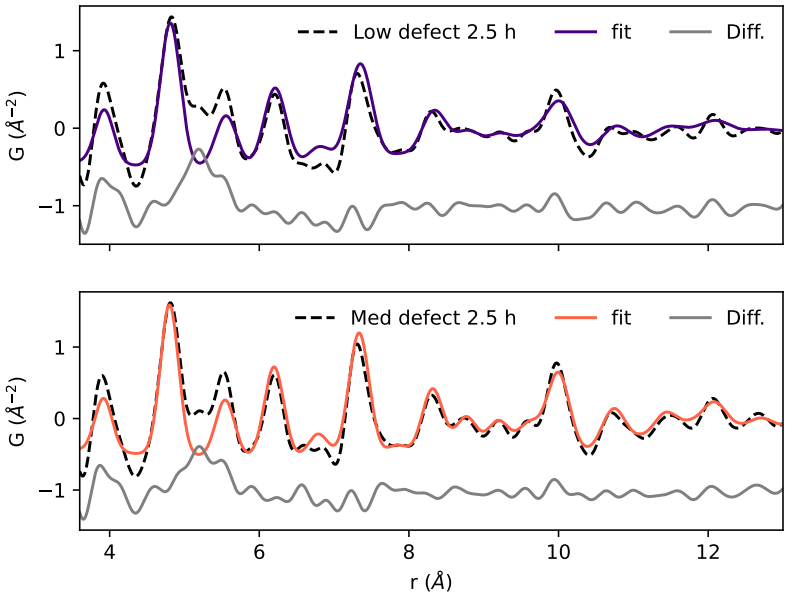

Figure 3.29: d-PDF data for Pt@UiO-66(NH_2) catalysts after 2.5 hours of catalysis.

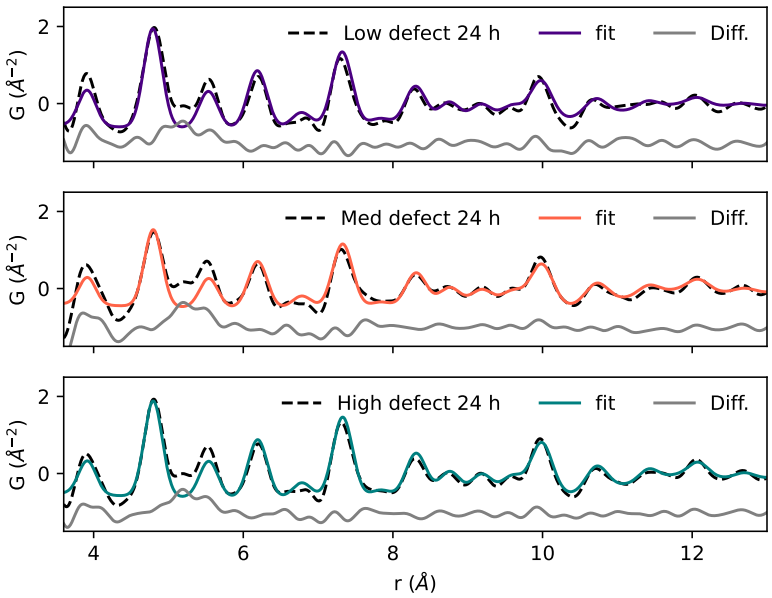

Figure 3.30: d-PDF data for Pt@UiO-66(NH_2) catalysts after 24 hours of catalysis.

XPS analysis was conducted of the samples after 24 hours of catalysis. The XPS spectra after catalysis are shown in Fig. 3.31. The XPS spectra for Pt after catalysis show significant growth in the $Pt^{\delta+}$ component in all samples. Prior to catalysis, the low defect sample showed no $Pt^{\delta+}$ presence. An additional component was required in the high defect Pt spectra for sufficient fits, with only 0.4 eV shift from the previously identified $Pt^{\delta+}$ component.

Prior to catalysis, both high and med defect materials show two Zr components, the expected Zr^{4+} of the MOF, and minor additional components at higher binding energies. After catalysis, the med defect material no longer shows an additional component (previously identified as a Pt-Zr interface), while this component grows significantly in the high defect material. Both materials are defective UiO-66(NH_2), therefore it is unexpected for them to show opposite effects. A repeat experiment is desired for this result, as XPS measures a small area of the surface, and this anomalous result may not be indicative of the whole sample.

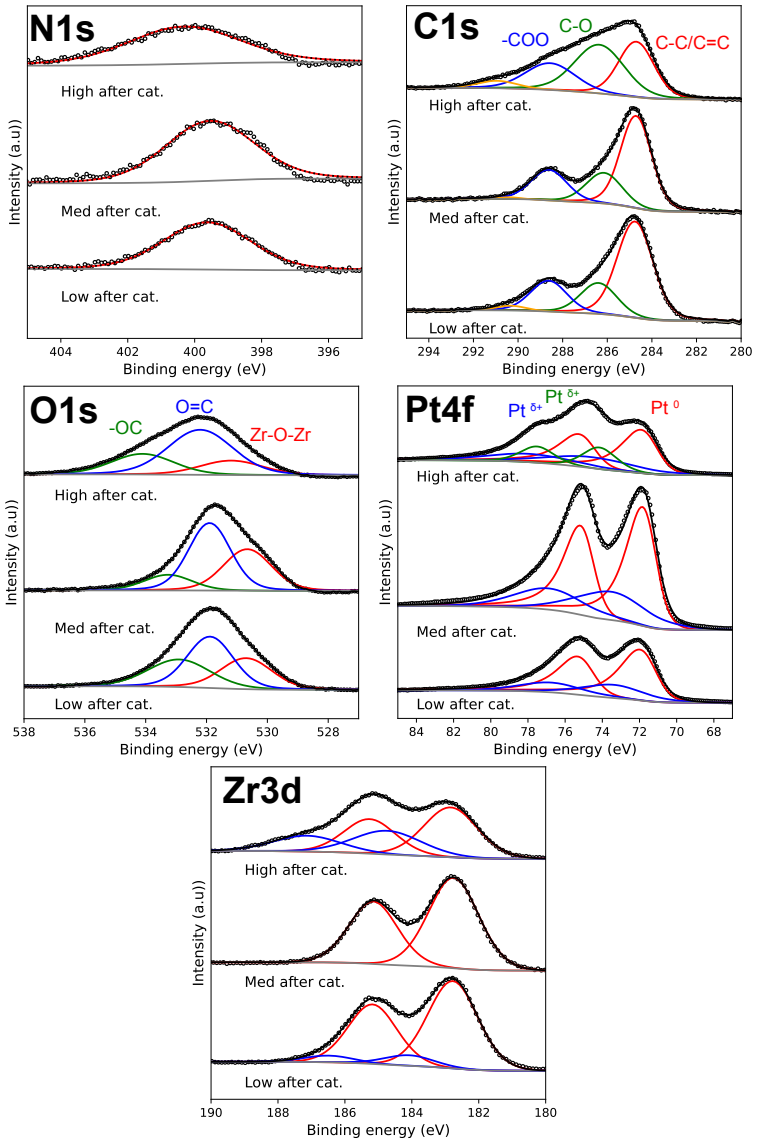

Figure 3.31: XPS spectrum for Pt @ UiO-66(NH_2) after exposure to 24 hours of photocatalytic hydrogen generation.

Peak positions and intensities for each Pt component are shown in Table 3.5. The most noteworthy feature from Pt XPS data is the shift in $Pt^{\delta+}$ BE for med and high defect materials. The position of $Pt^{\delta+}$ is better described by its distance from Pt^0, as the calibration to adventitious carbon is not ideal for describing absolute values. In the low defect material, $Pt^{\delta+}$ BE shifts only 0.03 eV higher after catalysis, whereas the medium and high defect materials' $Pt^{\delta+}$ BE shifts -0.73 and 0.72 eV respectively. This indicates that the Pt in medium and high defect concentration materials is at a different chemical environment after catalysis, whereas the Pt in the low defect material is in a similar chemical environment.

Sample	Pt^0, $Pt^{\delta+}$ $4f_{7/2}$ BE (eV)	Pt^0:$Pt^{\delta+}$ Area	Pt^0–$Pt^{\delta+}$ ΔBE
Low before	71.42, 72.95	1.35	1.53
Med before	71.40, 73.95	2.69	2.55
High before	71.64, 73.30	1.83	1.66
Low after	71.85, 73.41	2.63	1.56
Med after	71.72, 73.54	2.16	1.82
High after	71.78, 74.53	1.01	2.75, 2.38

Table 3.5: Peak positions and relative areas for Pt^0 and $Pt^{\delta+}$ components measured in Pt @UiO-66(NH_2) catalysts with XPS. The Pt in the high defect material after catalysis shows a third distinctive environment with peaks at: 74.16 and 77.51 , these peak positions are not included in the table, although their peak area is included in the calculation of Pt^0:$Pt^{\delta+}$.

3.3 Discussion

Addition of water to the reaction mixture has been shown to create defects and decrease MOF particle size, a mechanistic study for which has not been conducted. Similar research can be seen in work by Firth *et al.*, showing that water content in a sythesis can dictate the phase of UiO-66(Hf).[51] There are many potential mechanisms by which defect generation could be controlled by the content of water.

For syntheses conducted in DMF, $ZrCl_4$ has been shown to form $Zr_6O_4(OH)_4$ clusters spontaneously with or without the addition of ligand; the formation of these clusters has been established as the first step in UiO-66 synthesis.[55,56] As DMF is hygroscopic and hydrophillic, it is likely that this cluster formation involves the presence of water, as there were no drying procedures reported during the study of this cluster formation.[56] Water is an essential consituent of the reaction

for zirconium-oxo cluster formation from $ZrCl_4$, required as an oxygen source, and the role of water in this cluster formation will likely be the key variable dictating the observed particle size and defect changes presented in this chapter. Water (and hydroxides) have been shown to be prevalent capping ligands of defects through DFT and diffraction experiments.[65,66] Increasing the amount of water present in a reaction will therefore aid the formation and stabilisation of missing linker sites, as some co-ordination is required at these defect sites.

$ZrCl_4$ reacts with water, evolving HCl and producing a $[Zr_4(OH)_8(H_2O)_6]_8{}^{8+}Cl_8{}^{-}$ cluster containing bridging hydroxyl ligands which is stable in a range of reaction media.[106]

If formation of the $[Zr_4(OH)_8(H_2O)_6]^{8+}Cl_8^-$ cluster acts as an intermediate, providing faster zirconium-oxo cluster formation, it could enable faster framework co-ordination, and thus crystallisation during the synthesis of UiO-66(NH_2). Faster crystallisation explains the trend in decreasing particle size with water addition. The faster crystal growth would allow modulator effects in defect generation to be increased, where the modulator occupies co-ordination sites while the crystal grows around the occupied sites more quickly, and the surrounding extended framework would sterically hinder any linkers diffusing into pores for node - linker co-ordination at the defect site.

The final effect of water addition is the generation of HCl by the reaction of $ZrCl_4 + 2\,H_2O \rightarrow ZrO_2 + 4HCl$ or during the $[Zr_4(OH)_8(H_2O)_6]^{8+}Cl_8^-$ cluster formation. HCl is a common modulator for UiO-66 synthesis, and addition of water would increase HCl concentration, indirectly increasing the modulator concentration by introducing more HCl, which would modulate the synthesis with the intended formic acid.

From these potential mechanisms, it is unclear which individual or subset of interactions cause the defect generation through water presence. To properly elucidate the mechanisms, an in-situ pair distribution function study would be required, similar to that reported by Firth *et al.*[55] Synthesis using $ZrOCl_2$ rather than $ZrCl_4$ could also provide insight on the role of water as an oxygen source during cluster formation. Mechanistic studies are beyond the scope of this research project, as the interactions are complex and potentially numerous, and the focus of this research is the materials applications in catalysis.

Attempts to create a range of defect concentration by varying the metal:linker concentrations were unsuccessful, after numerous iterations of synthesis with different conditions. The hypothesis that increased ligand concentrations would reduce the effective competition from modulators did not materialize as a trend in defect concentrations. H2NH2BDC is very poorly soluble in all solvents, as it forms strong intermolecular hydrogen bonds with other molecules of H2NH2BDC. This poor solubility limits the concentrations of ligand that can be achieved during a synthesis, therefore making this approach difficult to use in reducing the defect concentrations due to the limit of linker:modulator which can be achieved. Reducing the quantity of modulator is a possibility to avoid this problem of linker solubility, but experiments proved that changing modulator amount was unpredictable with respect to the effect on framework physical properties. The defect concentrations varied within a reasonably tight range for metal:linker ratio. As mentioned earlier, when the framework forms around a point defect, large amounts of steric hindrance is produced, potentially isolating a defect from any sterically bulky linkers in solution. These isolated defects are impossible to form linker co-ordinate bonds, meaning the defect can not be removed, therefore limiting how much linker concentration will affect defect concentration. It has been shown that the **reo** phase, which contains missing clusters and linkers, can be converted to the **fcu** phase which contains no missing cluster defects and many fewer (or no) missing linker defects.[107] This is possible in the **reo** structure, but difficult for missing linker point defects, as the **reo** structure is much more porous and therefore less sterically hindered, exposing the defect sites to dissolved SBUs.

Varying modulator concentrations produced unexpected defect concentrations, with an unclear trend. As mentioned earlier, this can be largely attributed to the water content inevitably present in formic acid. Therefore, introducing large amounts of modulator also introduces water, which effects the synthesis in multiple potential mechanisms.

Defects in UiO-66 have been established to increase the rates of its catalysis in thermal and photocatalysis for many reactions[56,108]. The most notable effect on catalysis for defects is that 'open sites' are created on a defect, where labile surface bound water gives increased Bronsted acidity.

PXRD and TGA data have shown that increased water concentration in a reaction mixture increases missing linker concentration, while retaining crystallinity. The highest concentration of missing linker defects, 20.0% is significantly below the critical point after which the framework has been shown to begin collapse, 35.8%.[109] The defect concentration of the med defect and high defect materials allows for the positive influence of defects on catalyst stability, while low enough to retain framework stability. Using TGA to quantify defect concentration provides us with a ratio of clusters: linkers by completely oxidising the framework. This method cannot detect any missing clusters present in the framework, which are not present in large amounts as shown by the lack of 100 and 110 diffuse peaks in PXRD, but there may still be some missing clusters in small amounts. The concentration of missing linker defects will be slightly higher than the calculated quantites when also accounting for any possible missing clusters, but this cannot be quantified without neutron diffraction.[110]

The increased missing linker concentration gives rise to open sites on metal clusters, capped by water molecules and hydroxide ions (one of each for every defect for charge balancing). Considering that each cluster is connected to 12 linkers, it is likely that both med defect and high defect materials have defects present on the vast majority of clusters, meaning that they should both have an increased stabilising capability for nanocatalysts compared to low defect. The presence of defects at every cluster would account for the very similar shift in Pt particle sizes shown in Fig. 3.26.

Across all defect concentrations the size and distribution of Pt NPs is similar: Pt NPs are disproportionately located at the surface of MOF particles, which is shown in TEM images (Fig. 3.25). After catalysis Pt NPs still occupy the surface of MOF particles preferentially. There are two reasons for Pt NP distribution preferentially at the surface of MOF particles. Depositing nanoparticles using magnetron sputtering means that Pt first comes into contact with the MOF at the surface. It is possible for Pt to diffuse through the pores beneath the surface by anomalous diffusion, however the opportunity is limited to particles small enough to fit through the pores (sub-nanometer in the ideal crystal structure of UiO-66(NH_2)).[111] Slower deposition speeds, or higher temperatures during sputtering could provide opportunity for the Pt to more uniformly diffuse through the MOF in future work. The second

reason for preferential Pt distribution at the surface, is that the surface itself is undercoordinated, and higher energy, similar to the defect sites. A nanoparticle at the surface of the MOF is lower energy than one deeper within the lattice. XPS quantification provides an indication of the atomic presence at the surface, and 5-10 nm beneath the surface (it should be noted that XPS atomic quantification does not provide exact values, but an estimate, as the analysis is of a very small surface region). In the low, med and high defect materials, Pt atomic % from XPS is 15.46, 1.68 and 10.57 % respectively. These values correspond to 66, 15 and 55 wt% Pt at the surface of MOF particles, and ICP-OES shows that no material is deposited with more than 3.1 wt% Pt.

d-PDF measurements of each samples in the defect series in Fig.3.21 show a clear difference in the magnitude of the Pt–Pt correlations, with the low defect material showing much smaller peaks than med and high defect materials. This data was all collected with the same parameters, therefore it is not expected to have such variation, considering the Pt loadings are similar (the low defect material has a higher Pt loading than the med defect material). This lower intensity signal cannot be attributed to the subtractions, as all subtractions are precisely calculated according to a consistent, strong peak in the MOF cluster which does not change according to defects or particle size (intracluster Zr–Zr), therefore the subtractions are all normalized to each-other. The peak intensities are therefore representative of the Pt distributions within the sample.

The Pt in the low defect material therefore has far fewer measurable Pt-Pt correlations, however the Pt is still present, as shown in the ICP-OES data. This 'missing' Pt could be in amorphous or poorly ordered Pt nanoparticles, but this cannot exclusively explain the intensity change. With poor ordering in a nanoparticle, the atomic correlations would still exist, the peaks would be broader, but approximately of the same total area in different samples. Poor ordering would be represented crystallographically by higher U_{iso} values, which cause PDF peaks to broaden but maintain the same area.[112] Due to the similar width of the first Pt–Pt correlation in each catalyst, it is unlikely that much of the Pt is in a disordered metallic species. The low defect material has the highest proportion of $Pt^{\delta+}$ from XPS analysis, which likely relates a to platinum oxide species. Oxygen's weak X-ray scattering causes smaller peak intensity for Pt-O than Pt-Pt in XPDF, therefore this species accounts for some of the missing intensity.

Some of the Pt present in the low defect material is likely in the single-atom species, at the zirconium-oxo clusters. This would cause Zr Pt correlations, which are 2.9 Å in Pt/ ZrO_2.[113] The data in the low defect material shows a discrete peak at 3.05 Å, which is not present in med or high defect materials. The only UiO-66 correlation at this distance within ± 0.2 Å is a weakly scattering C-O correlation, which will not contribute greatly to the PDF. This correlation indicates that the low defect sample contains a significant amount of Pt –Zr, which is not present in other defect concentrations. This unique correlation shows evidence that the low defect material has a much larger proportion of small Pt clusters or single atoms present than the more defective samples, and the more defective samples have a larger proportion of Pt nanoparticles. These small particles are likely the cause for the increased activity in the low defect material.

The structure of Pt nanoparticles deposited onto materials of every defect concentration are similar before catalysis. d-PDF for these materials shows pure *fcc* Pt nanoparticles for all materials, with no secondary phase detected by PDF analysis. While no Pt oxide is detected through PDF, some may still be present at the surface, Pt-O correlations are weaker than Pt-Pt when probed with X-rays due to the weaker X-ray scattering factors of O than Pt. Also the Pt-O at the surface of NPs is likely poorly ordered, and a minor phase, where the surface of nanoparticles has only been extracted once using d-PDF.[114] XPS analysis of Pt indicates that there are two platinum components, a metallic core Pt and an oxidised surface species, of which the surface species constitutes a lower proportion than the core. If Pt^0 and PtO_2 nanoparticles were both present, the PtO_2 would be detected in PDF measurements. The $Pt^{\delta+}$ component is present in significant proportions, and if it were caused only by formation of an interface with the MOF, there would be a clear correlation in the PDF. The platinum oxide species at the surface of nanoparticles is confirmed by comparing PDF and TEM particle size analysis, as the Pt particle size calculated through PDF fitting is always smaller than those measured in TEM, indicating that the particles are not pure metallic Pt. This complementary data shows that the surface of Pt nanoparticles is poorly ordered, the surface is a distinctly different chemical environment to the core and the surface structure cannot be extracted using X-ray PDF measurements.

Pair distribution and TEM are important complementary techniques in

the analysis of these catalysts for Pt characterisation. For UiO-66 TEM imaging is limited, as the material is highly beam-sensitive under the electron beam, and scatters electrons strongly due to the heavy Zr nodes. The beam sensitivity demands low dose imaging to preserve the material. Lower energy electrons (<200 kV) produced poor resolution for these samples (Fig. 6.11), and attempts to image using AC-STEM produced large amounts of beam damage therefore did not produce useful images (Fig. 6.8). The low dose of electrons with a strongly scattering support material makes for difficult imaging of the small particles of platinum. Nanoparticles which are either below the surface of the MOF, or less than 1 nm in diameter are not visible in a laboratory TEM. While limited in these areas, TEM is capable of clearly imaging particles above 2 nm, and allows for determination of a particle size distribution, which is useful to measure particle sintering. TEM and PDF are complementary for particle analysis, as PDF gives a view of the whole sample, including single atoms, nanoclusters and Pt below the surface, while TEM provides accurate particle distributions to analyse how sintering occurs for the most prevalent species.

The Pt species measured in XPS are supported nanoparticles, and their chemical environment is not uniform throughout the sample, particularly surface species of nanoparticles. The neighbours of each atom, and their proximity to the surface dictate the signal observed in XPS. Because of this inhomogeneity, the observed XPS peaks for oxidised platinum species are very broad, and often of binding energies which are not convincing of a distinct oxidation state or environment. This has been acknowledged in previous work, and the practice of δ oxidation states has been used to describe SACs.[115] δ oxidation states can be formally assigned values by calculating using precise references measured on the same instrument, which are unavailable for this work, so I do not calculate exact δ oxidation states to avoid potentially spurious results. Rather we acknowledge that these peaks are not discrete BEs for any Pt material, but rather peaks corresponding to $Pt^{\delta+}$ at the interface of nanoparticles and MOF.

Pt XPS for all materials shows presence of both Pt ^{0} and $Pt^{\delta+}$. Which relates to the core and surface of nanoparticles respectively. The presence of Pt ^{0} in all samples is expected, substantial proportions of Pt atoms in ~2 nm particles are below the surface, and these sub-surface atoms are resistant to chemical change by interface formation with Zr

or O atoms.

XPS analysis of Zr in the low defect sample shows a good fit with Zr^{4+} at 182.81 and 185.21 eV, which is expected in UiO-66(NH_2). Med defect also shows Zr^{4+} peaks at 182.22 and 184.64 eV, but a second pair of peaks was required to fit the data sufficiently (at 184.40 and 186.80 eV). The second set of peaks are very broad, however clearly required in the data. Given the established interaction between Pt and defect sites, it is reasonable to attribute these extra peaks to a minor Zr species generated at defect sites where Pt nanoparticles and hydroxyl ions are bound. The high defect sample also requires 2 sets of spin-orbit coupled Zr peaks to adequately fit the observed data. One set of peaks are measured at 182.70 and 185.09 eV, while the second set are measured at 184.32 and 186.72 eV.

The interface of Pt NP and MOF in med and high defect materials is primarily the crystallographically challenged $Pt^{\delta+}$ oxide species in contact with the MOF (particularly at the surface of the MOF) with no distinct ordering between MOF and Pt NP. This surface Pt species is highly likely to be a Pt oxide. The low defect material contains large amounts of the same poorly defined interface as med and high defect materials, but also a Zr-Pt correlation detected in d-PDF, which I attribute to Pt SACs or small NCs.

The differences in Pt loading between low defect, med defect and high defect materials can be attributed to differences in the mass of each sample deposited with Pt. Removing water by vacuum heating is imperative for hygroscopic, porous samples such as these MOFs. Without removing all of the water from the surface, it is difficult to reach a pressure low enough for magnetron sputtering deposition. During the vacuum drying, some of the MOF adheres to the vessel in which they are stored, hence not all of it can be retrieved after drying. The variation in mass of the MOF when deposited can affect the loading of Pt on a support, as all samples were exposed to the same current, power and time under magnetron sputtering deposition, therefore all samples are deposited with the same amount of Pt.

Pt-deposited samples low–high defect in photocatalytic hydrogen generation show that increasing defect concentrations reduce the rate of hydrogen generation in Fig. 3.23. This is contrary to the current understanding, where defects have only been a positive influence on the rates

of catalysis.[80,108]

The enhanced activity from the low defect sample can be attributed to the presence of single atoms/nanocluster catalysts which were observed in d-PDF. These species of catalysts have an effectively 100 % atom utilization, whereas the observed Pt nanoparticles of 2 nm have only ~60 % utilization due to atoms below the surface.[11] These SACs provide a great increase in activity, as they provide a greater activity to the low defect sample than to more defective ones, despite the enhanced MLCT open sites at defects, which both aid photocatalysis. These catalysis results are unique with respect to defective UiO-66 catalysts in literature, because defects most often impart benefitial catalytic activity. I attribute this behavior to the increased porosity introduced with missing linker defects. In a defect-free UiO-66 framework, there are no cavities capable of fitting a Pt particle of over 1 nm, however removing one ligand increases the cavities to house 1.5 nm particles comfortably. The larger pores within the catalyst allow larger particles to be created beneath the surface during deposition through anomalous diffusion, which is driven by porosity.[111] By contrast, a defect-free sample only allows very small particles beneath the surface, due to the steric bulk, therefore sub-nanometre catalysts are the upper size limit beneath the surface. This effect is particularly important, as Pt below the surface of UiO-66(NH_2)has been shown to be more active than Pt at the surface of the MOF.[81] This is the first published instance of defects reducing the rate of catalysis in a UiO-66 family catalyst.

After 2.5 hours of catalysis, defective samples particle size changes are within error, while the low defect material shows great nanoparticle growth. This can be attributed to the anchoring effect of the missing linker defects, creating kinetically stable nanoparticles on the clusters adjacent to a vacancy, whereas the low defect material has no such sites, therefore nanoparticles are much more mobile. While the particles in the low defect material grow significantly, the size of Pt crystallites does not increase much, indicating that the sintering observed is growth of the $Pt^{\delta+}$ shell. This sintering observation is supported by the increase in proportion of $Pt^{\delta+}$ measured in XPS after catalysis. The low defect material has the largest MOF particles, and therefore the accessible specific surface area for Pt NPs is lowest in the low defect material, which will contribute to particle sintering through particle mobility.

After 24 hours, both med and high defect materials remain largely unchanged in their nanoparticle size distribution, while the low defect material shows a decrease in the mean nanoparticle size. The decrease in the low defect material is derived largely from the loss of nanoparticle presence above 4 nm. This loss of nanoparticle size is likely caused by dissolution of surface nanoparticles through leaching, as there are very few stable co-ordination sites for the large nanoparticles. The presence of defects in med and high defect materials prevent sintering significantly, and appear to provide 'anchor sites' at which catalyst nanoparticles can bind.

The Pt deposited low defect material is the best catalyst for hydrogen generation in this thesis, producing hydrogen at a rate of 2.7 $mmolh^{-1}g^{-1}$ under photocatalytic conditions. Xiao *et al.* report Pt @ UiO-66(NH_2) photocatalysts, producing H_2 at a rate of 257.38 $\mu molh^{-1}g^{-1}$, however this uses visible light catalysts which is lower energy and less readily absorbed by UiO-66(NH_2).[81] Wang *et al.* report Ti decorated Pt @ UiO-66(NH_2) photocatalysts which produces H_2 at a rate of 0.6 $mmolh^{-1}g^{-1}$ under photocatalytic conditions. Addition of Ti shows a marked improvement on photocatalytic performance by reducing the MOF 'band gap'.[116] Wang *et al.* report a novel method for improving MOF photocatalysis, by depositing Pt at the UiO-66(NH_2), and coating with an outer layer of ~20 nm UiO-66(NH_2). This takes advantage of the superior performance of Pt deposited below the surface of UiO-66(NH_2) when compared to those deposited at the surface.[81,117] With this technique, H_2 is produced at a rate of 2.7 $mmolh^{-1}g^{-1}$. Despite similar materials, rates of hydrogen generation for Pt@ UiO-66(NH_2) range from 0.6 to 2.7 $mmolh^{-1}g^{-1}$. The low defect material produced in this thesis matches the highest rates reported, however the photocatalytic setup must be considered. Not all photocatalytic reactors produce equal rates of photocatalysis with the same material, therefore results from different reactors are not directly comparable, as is demonstrated in depth in the following chapter. Absolute rates of photocatalytic hydrogen generation using UiO-66(NH_2)are not vital, as TiO_2 is cheaper, easier to make and a better photocatalyst for hydrogen generation (which is demonstrated in the following chapter). Pushing the rates of hydrogen generation beyond previous authors is not the goal. Research such as this thesis, and the papers mentioned in this paragraph, demonstrate techniques to develop better photocatalysts which can be transferrable to other MOFs

and materials, where the principles build knowledge of what creates an effective photocatalyst.

3.4 Conclusions

I have generated a series of phase-pure *fcu* UiO-66(NH_2) with missing linker defect concentrations of 0.5, 13.3 and 20.0 %. When deposited with Pt using magnetron sputtering, these Pt catalysts show similar particle size distributions and mean particle sizes. After 2.5 hours of photocatalysis under UV irradiation, the material with the lowest defect concentration shows significantly more sintering than the other catalysts. After 24 hours of photocatalysis, the material with the lowest defect concentration shows a decrease in mean catalyst particle size from the 2.5 hour value, although this is still larger than those of the medium and highest defect concentrations. These platinum particle sizes confirm the stabilising effect of missing linker defets on Pt nanoparticles supported onto UiO-66(NH_2).

Materials with lower defect concentrations show higher rates of photocatalysis for photocatalytic H_2 generation. The lowest defect concentration material is the only sample to show Pt - Zr correlations in PDF data, which indicates the presence of single-atom catalysts. The presence of these single-atom catalysts is the cause for its higher relative activity, and their formation is enabled by the lack of defects, rather than a property of the defects to intrinsically reduce photocatalytic activity.

The crystallographically challenged surfaces of nanoparticles make elucidating exact interfaces between MOF and NPs difficult. I identify distinct surface and core Pt components through XPS, and conclude through d-PDF that the surface of NPs and MOF do not interact in an ordered manner (due to the disorder at NP surface). Interfaces between Pt SACs/ NCs were identified in the low defect material using XPDF analysis. I have identified that sintering of the co-catalyst is caused by increasing the Pt $^{\delta+}$ surface species, and the size of core Pt^0 does not increase.

Chapter 4

Photocatalytic reactor design and optimisation

4.1 Introduction

Any catalytic reactor has a number of important considerations: Stirring, dimensions, catalyst material and so forth. While photocatalytic reactors share many of the same considerations, there are a number of additional parameters to be considered. In this chapter, I review the optimsation and experimentation with said parameters, over the course of my PhD, from which a newly implemented photocatalytic reactor was optimised and refined for UiO-66(NH_2) photocatalysis.

Some considerations for a photocatalytic reactor on the laboratory research scale in this thesis are trivial, such as: Catalyst removal and scale, therefore they will not be discussed in this chapter, though they are important when considering the difficult task of scaling up photocatalytic reactors.

A number of considerations and decisions must be made for a photocatalytic reactor, Table 4.1 shows a number of important parameters considered in this chapter.

Illumination	Flow	Materials	Reactor type	Geometry
Solar Sim.	Batch	Chemical resistance	Suspension	Dimensions
UV	Continuous	Transparent window	Thin-film	Light penetration
LED	Flow	Photosensitivity		Headspace
Lamp				
Distance				

Table 4.1: Some of the important considerations when designing a photocatalytic reactor

UiO-66(NH_2) photocatalysts have used both visible and UV light in literature, due to the absorption bands in the visible and UV regions (absorption peaks at 250-300 nm and 320 –410 nm). Visible light is the preferred choice whenever possible, as discussed in *Photocatalysis*, with to the ultimate goal of solar light harnessing to power photocatalytic reactions. UV light provides higher energy photons, producing more photoexcitations to the CB, therefore giving a higher activity in photocatalysis (assuming absoprtion is equal in both regions). It is most common for UiO-66(NH_2) catalysts to utilise visible light in photocatalystic hydrogen production, as titania provides higher UV activity, and research aims to improve visible light photocatalysis.[81,118,119]

A suspension reactorn is the most common choice for UiO-66(NH_2) photocatalytic reactors, requiring minimal preparation and providing replicable preparation procedures. In a suspension reactor, powdered photocatalyst is stirred and exposed to photons while in a suspension. This is particularly common for reactions using electron donors such as methanol or triethanolamine. Immobilized catalysts are an alternative to suspensions, where the photocatalyst is anchored to a non-reactive material to create a dispersed thin film.[120] Immobilized catalysts are less replicable in research applications, any macroscopic inhomogeniety or film damage affects catalyst performance. Immobilized catalysts also allow for a thin film of catalyst, maximising catalyst illumination using a small amount across a wide area. Light penetration is a key concern for photocatalytic scaleup, making immobilised catalysts promising for scale-up, with the thin films and ease of catalyst removal compared to suspensions.[22,120]

An immobilizing material should provide a strong adherenace to the photocatalyst and not degrade catalyst reactivity, and be not exhibit photosensitivity, commonly borosilicate glass is used.[120] Catalysts can be immobilized through many methods, such as the sol-gel approach, ALD, sputtering or drop-casting.[120,121]

In a catalyst system assessing catalyst activity with continuous carrier gas flow and iterative GC measurements of product activity, such as in this thesis, headspace should also be considered. A GC injection measures the concentration of gases at the time of injection, used with a calibration this provides the concentration in mmol. With a continuous flow of carrier gas, an equilibrium concentration is reached, such that

the flow of hydrogen out of the reactor is equal to that produced by the catalyst (indicated by a plateau in the concentration). To convert the concentration of hydrogen into a rate of hydrogen generation, I use equation (4.1):

$$\text{Rate of } H_2 \text{ generation} = \frac{\text{hydrogen conc.} \times \text{flow rate}}{\text{headspace}} \tag{4.1}$$

4.2 Methods

4.2.1 Gas Chromatography

I used an Agilent 5890B gas chromatogram, with a thermal conductivity detector (TCD) used to measure the concentrations of H_2, N_2 and O_2. The TCD was connected to a molecular sieve column, separating gases on their molecular radius, such that the smallest molecules pass are measured first. I used a flame ionisation detector (FID) which is connected to a silica column, and mass spectrometer attached to the same column, such that any species detected in FID are also analyzed by mass spectrometry.

4.2.2 Photocatalysis in suspension reactor

Suspensions were created by mixing 30 mg ground Pt @ UiO-66(NH_2) with 20 mL 10% methanol in water, and stirred using a magnetic stirrer bar.

Photocatalytic experiments were purged with argon flow of 100 sccm, and GC injections were taken every 14 minutes, with the TCD detector measuring the presence of N_2 and O_2. Purging continues until these peaks are removed, typically this occurs after 40-60 minutes.

After purging, argon gas flow is reduced to 0.1 sccm, the chosen lamp illuminates the suspension and GC injections occur every 14 minutes thereafter. The TCD detector is used to monitor N_2, O_2 and H_2 peaks. H_2 peaks are converted to molar concentrations using a calibration curve.

4.2.3 Photocatalysis in PEEK reactor

Suspensions were created by mixing ground Pt @ UiO-66(NH_2) with 0.7 mL 10% methanol in water, and stirred using a magnetic stirrer bar.

Photocatalytic experiments were purged with argon flow of 100 sccm, and GC injections were taken every 14 minutes, with the TCD detector measuring the presence of N_2 and O_2. Purging continues until these peaks are removed, typically this occurs after 40-60 minutes.

After purging, argon gas flow is reduced to 1.0 sccm, a 365 nm UV lamp illuminates the suspension and GC injections occur every 14 minutes thereafter. The TCD detector is used to monitor N_2, O_2 and H_2 peaks. H_2 peaks are converted to molar concentrations using a calibration curve.

4.2.4 Photocatalysis in glass flat cell reactor

Suspensions were created by mixing ground Pt @ UiO-66(NH_2) 1 mL methanol in water, sonicated for 30 seconds. This mixture was then dropcast onto a 15 x 25 mm glass slide and allowed to evaporate at room temperature.

The dropcast glass slide was immersed completely in 10 mL of 10% methanol in water, and purged with argon flow of 30 sccm and GC injections were taken every 14 minutes, with the TCD detector measuring the presence of N_2 and O_2. Purging continues until these peaks are removed, typically this occurs after 40-60 minutes.

After purging, argon gas flow is reduced to 1.0 sccm, a 365 nm UV lamp illuminates the immobilised catalyst and GC injections occur every 14 minutes thereafter.The TCD detector is used to monitor N_2, O_2 and H_2 peaks. H_2 peaks are converted to molar concentrations using a calibration curve.

4.3 Results

In this chapter, I explore various designs of photoreactor on the same GC with the same detectors throughout. Throughout the optimsation, quantitative results are used only to optimise the catalytic activity to-

wards hydrogen generation. As some reactors generated extremely low concentrations of hydrogen it is impractical to provide a catalytic activity in $mmolh^{-1}g^{-1}$. These low concentrations of hydrogen are below the calibration curve, and calibrating to lower concentrations would require additional mass flow controllers to dilute our calibrant. It is more comparable to use the arbitrary units of the GC for peak area to compare concentrations (and by extension relative rates of hydrogen generation).

Experiments for photocatalytic hydrogen production used both a solar simulator light source, and UV a lamp. The λ dependent intensity emission profiles are shown in Fig.4.1. These emission profiles are overlapped with the UV DRS profile of UiO-66(NH_2), the photocatalyst for which reaction optimisations were performed. A solar simulator was investigated, despite its poor emission overlap with the absorption of UiO-66(NH_2), as a photocatalyst for hydrogen generation using visible photons is highly desirable to harness sunlight for renewable fuel sources.

The overlap between the strong absorption band of UiO-66(NH_2) and the emission spectra of a solar simulation is relatively small. This poor overlap leads to very low rates of hydrogen generation, as only a small proportion of the emitted photons are absorbed for catalysis. The low efficiency and catalytic activity under solar simulated emissions led to my transition towards UV light exposure for catalysis, utilising the absorption band from 380 –420 nm of UiO-66(NH_2). The 50 W 365 nm Evolchem UV lamp more effectively overlaps its emission profile with the absorption bands of UiO-66(NH_2), as seen in Fig. 4.1. This creates a much higher photonic efficiency, as every photon emitted by this lamp is within the absorption band for UiO-66(NH_2).

The first photocatalytic experiments were performed using 2.5 wt% stirred suspension of UiO-66(NH_2)in 20 mL 10% methanol in water. The suspension was illuminated with visible light. The suspension reactor is depicted in Fig. 4.2.

Under visible irradiation, the H_2 peaks are extremely small, such that their area is affected by noise in the gas chromatogram and far below the quantifiable limit. To give a context for the peak areas discussed, approximate H_2 peak areas after 1 hour of irradiation are shown in Fig.4.3 for UiO-66(NH_2) and TiO_2 with varying light sources and co-catalysts. The H_2 peak sizes of Pt/UiO-66(NH_2) using visible light are 30 $\times$ lower than those generated by the same catalyst with UV irradiation. The

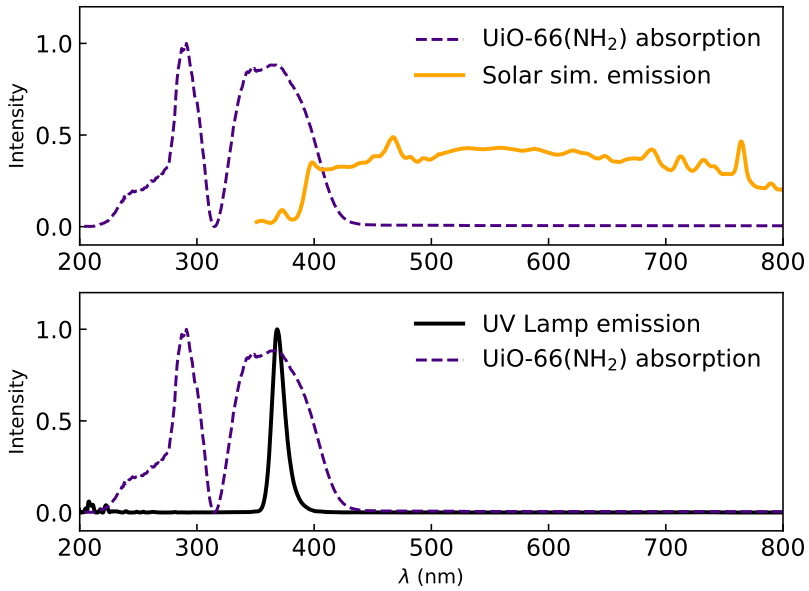

Figure 4.1: 365 nm UV lamp emission profile (black) overlayed with the UV-vis DRS spectrum of defect-free UiO-66(NH_2).

low catalyst activity with visible irradiation is caused by poor overlap between solar emission λ and photon absoprtion in UiO-66(NH_2).

Before each reaction, the system must be purged of air, as oxygen can quench photoelectrons through energy transfer from the co-catalyst or support material in a process like that of fluorescence quenching.[122] The presence of oxygen in the reaction will significantly reduce the activity for (the already kinetically sluggish) proton reduction half reaction. After purging all oxygen from this reactor, flow rate was decreased to 0.1 sccm and it could be observed that oxygen and nitrogen were generated over time, as observed by GC measurements (Fig. 4.4)

In Fig. 4.4, t=0 is the time at which flow rate was reduced from 100 sccm (purging) to 0.1 sccm (reaction flow rate), and illumination of the suspension begins. It can be observed that air peaks grow for approximately 1 hour after the reduction of flow rate and suspension illumination, which is attributed to equilibriation of gas concentrations between solution and headspace . The ratio of N_2:O_2 increases as time passes, with oxygen concentrations not detected after 2 hours indicating that oxygen is being consumed during the photoelectron quenching. Oxygen and nitrogen presence was caused by gases dissolved in the liquid equilibrating their concentration with that of the headspace. Dissolved gases make purging the system completely very time consuming, therefore the reac-

Figure 4.2: A suspension reactor, in which the suspension of photocatalyst in water and methanol (yellow)is stirred and irradiated from the side. The lid is fitted with 3 Swagelok joints for 2 inputs of carrier gas, and one output to carry products to the GC. The lid is screwed on and sealed by 2 rubber toric joints.

tion vessel was altered to purge the system directly, as shown in Fig.4.5. This adjustment makes purging much more efficient, and removes the dissolved gases completely. It should be noted that the concentrations of N_2 and O_2 here are very low, therefore will not affect the reaction too significantly. Our calibrations include N_2, not O_2, and the lowest calibration for this peak is an area of 107,000 (over double what was measured here), and this is calibrated to 2.23×10^{-4} moldm^{-3}, using atmospheric ratios, a leak creating a nitrogen peak of this area would have an associated 5.59×10^{-5} moldm^{-3} of O_2. While these concentrations are not detrimental to catalytic activity, any reaction alterations to minimise oxygen presence are made to obtain the most precise catalytic activity. To remove these gases from solution more effectively, the solution was purged directly by bubbling carrier gas through the solution (Fig. 4.5) through a PTFE tube, rather than passing carrier gas through the headspace.

The suspension reactor provides replicable catalyst activity, although consumes 30 mg of Pt @ UiO-66(NH_2) per reaction. This is problematic when considering that a 200 mL teflon-lined autoclave (the largest available) produces approximately 500 mg UiO-66(NH_2), and requires 4 days of laboratory time for each synthesis. In this reactor, catalyst activity was much lower than anticipated, even when the light source was optimised to a 365 nm lamp. The slower than expected hydrogen

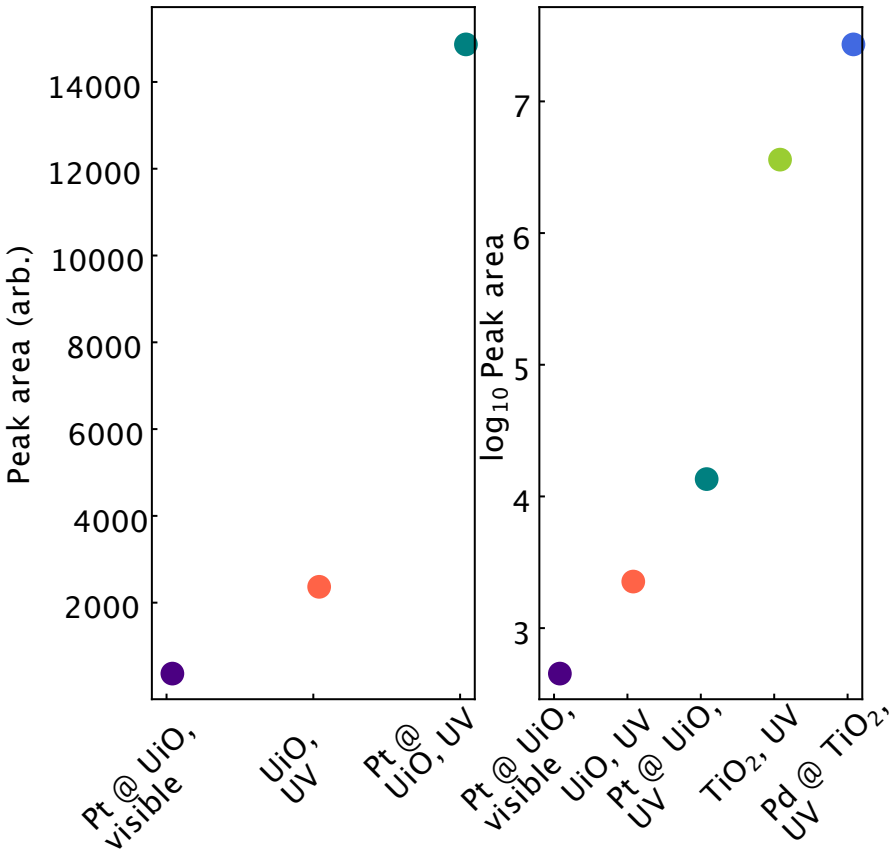

Figure 4.3: Approximate peak sizes for H_2 (left) after 1 hour of catalysis for the respective catalysts and irradiation types in UiO-66(NH_2). Visible light induces negligible hydrogen, and UV induces significantly more. (Right) Approximate peak sizes for H_2 after 1 hour of catalysis for the respective catalysts and irradiation types, including TiO_2 and Pd @ TiO_2 (logarithmic scale).

generation is attributed mainly to light penetration. The dimensions of this reactior are such that photocatalyst is suspended with a depth of 40 mm, a suspension which both scatters and absorbs incoming photons, therefore has large amounts of non-illuminated particles further from the light source. Light penetration is a key challenge in scaling up photocatalysis, and therefore suspension type reactions at larger scales occur in flow, or using microreactors, to reduce the internal diameter.[121]

Due to the difficulty in illuminating all of the catalyst inside the suspension reactor, I made attempts to create thinner catalyst suspensions in a high aspect ratio. By creating a thinner suspension across a wider area, it is possible to illuminate a higher proportion of the catalyst, obtaining an activity which is more limited by the photocatalysts themselves, rather than the reactor design. A bespoke design reactor (Designed by A. Lanterna and R. Wilson, and produced by R. Wilson, University of Nottingham, School of Chemistry) was created which allows thinner catalyst

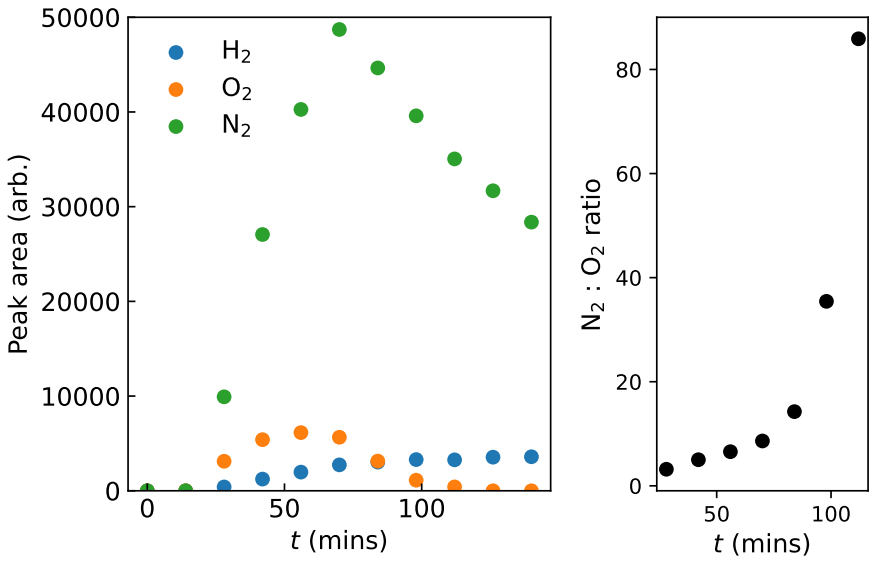

Figure 4.4: (left) Peak sizes of TCD response for H_2, N_2 and O_2 during photocatalysis, in the suspension reactor, where increasing N_2 and O_2 is caused by dissolved gases in solution. (right) Ratio of N_2 to O_2 peak sizes during photocatalysis.

suspensions (Fig. 4.6). This reactor houses the suspension inside an shallow insert of polyether ether ketone (PEEK), which is highly chemically and thermally stable.[123] While PTFE is highly popular for chemical applications, in this reaction, PEEK was preferred, due to PTFE porosity, which would allow nanoparticle diffusion, making complete removal of catalyst difficult and giving imprecise results. By using a shallow, wider reactor, the headspace in this reactor is much lower also, creating higher concentrations of H_2 present from an equally active catalyst in a larger headspace reactor , as shown in eq. (3.8). This allows a smaller catalyst quantity to be used (3 mg), and the flow rate of carrier gas can be increased (to 1.0 sccm), which makes the reactor more resillient to small leaks (and dissolved gases equilibriating), providing more accurate H_2 concentrations. This reactor is herein referred to as 'PEEK reactor'.

In this reactor, a suspension is created within the PEEK insert, and stirred while irradiated through the glass window. Concentrations of hydrogen obtained are typically higher than those in the suspension reactor, as the light penetration is not limited here, and the headspace is smaller.

In this reactor, illuminating photocatalyst through the window causes UV illumination of the surrounding reactor stainless steel lid and screws. When illuminated for extended periods, this causes heating of the reac-

Figure 4.5: The suspension reactor, fitted with PTFE tubing from the carrier gas input into the solution, leading to the solution to decrease purging time.

tor, and the stainless steel thermally expands. Thermal expansion of the screws causes significant leaks, as shown by the O_2 and N_2 peak sizes in Fig.4.7.

The PEEK reactor maintains no O_2 or N_2 presence detectable through GC for the first 42 minutes, and after 56 minutes the concentrations of O_2 and N_2 become very high (10× those generated in the suspension reactor in Fig. 4.4), indicating that this leak is induced during the reaction, and is therefore attributed to thermal expansion induced leaking from the screws.

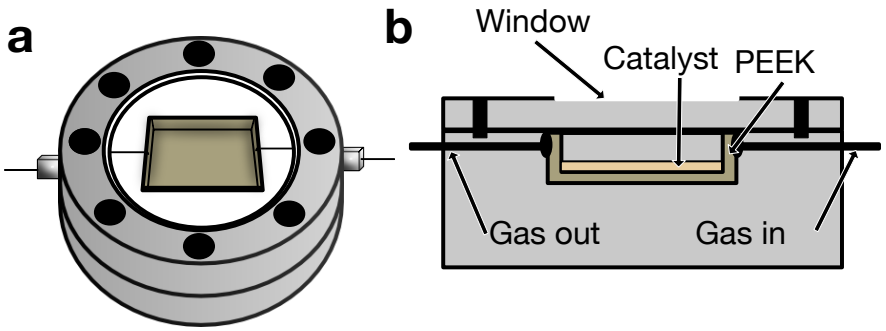

Figure 4.6: The PEEK reactor, viewed from the top (a) and a cross section side view (b). This reactor consists a PEEK insert, held beneath a glass window, which is sealed between two stainless steel plates by screws in the top of the reactor. Photocatalysts are illuminated from above, and carrier gas flows through the reactor through two diametrically opposed valves.

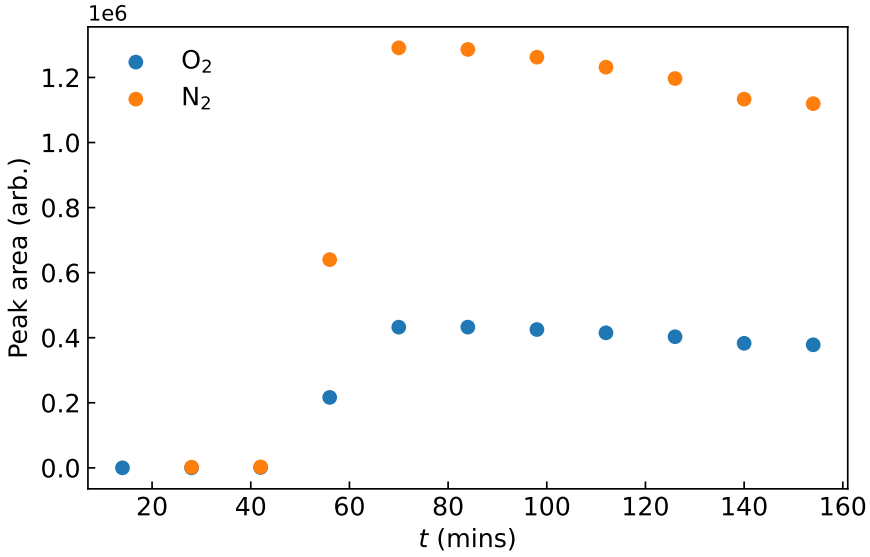

Figure 4.7: Peak sizes of TCD response for O_2 and N_2 in the PEEK reactor during photocatalysis. Increases in the presence of these gases is caused by thermal expansion of the stainless steel reactor assembly, causing leaks.

By submerging the reactor in a water bath (later our workshop engineering team installed a Peltier cooler below the reactor) and installing a cap to cover the screws, the reactor heating and leaking were remediated(Fig. 4.8).

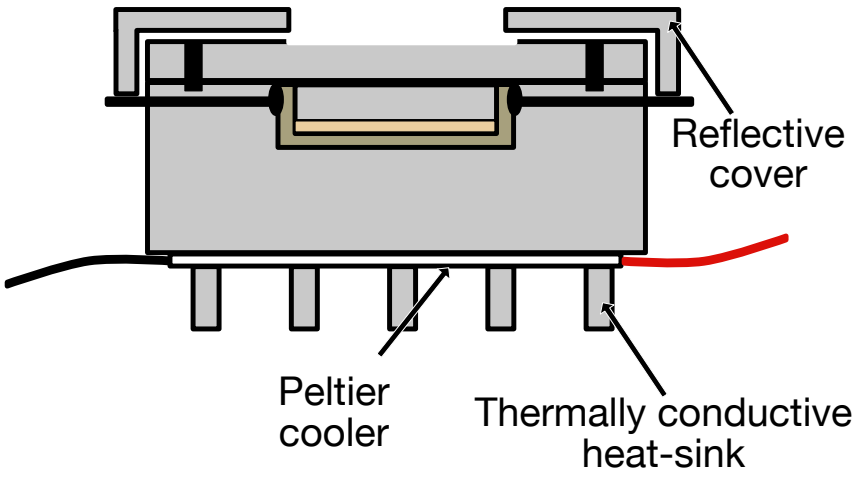

Figure 4.8: A cross section side view of the PEEK reactor, with adjustments to remediate irradiation induced leaking.

Hydrogen concentrations generated through photocatalytic hydrogen generation in the amended, leak-free PEEK reactor were higher than those obtained in the suspension reactor, even with an increased carrier gas was increased from 0.1 to 1.0 sccm. The increased flow rate of carrier gas is desirable, as the products are more consistently flushed from the

reactor headspace, causing lower error between each GC injection, therefore more accurate results. With the increased flow rate of 1.0 sccm, and 10× less catalyst the H_2 peaks from the PEEK reactor were still larger than those obtained in the suspension reactor (Fig.4.9). The reduced headspace contributes largely to these increased peak sizes (from 10 cm^3 in the suspension reactor to 1cm^3 in the PEEK reactor). The primary variable increasing peak sizes is the light penetration, as a much larger proportion of the catalyst is illuminated in this thin suspension. The reactors physical parameters (headspace, flow rate, amount of catalyst) would cause a decrease in peak size for an equally active photocatalyst.

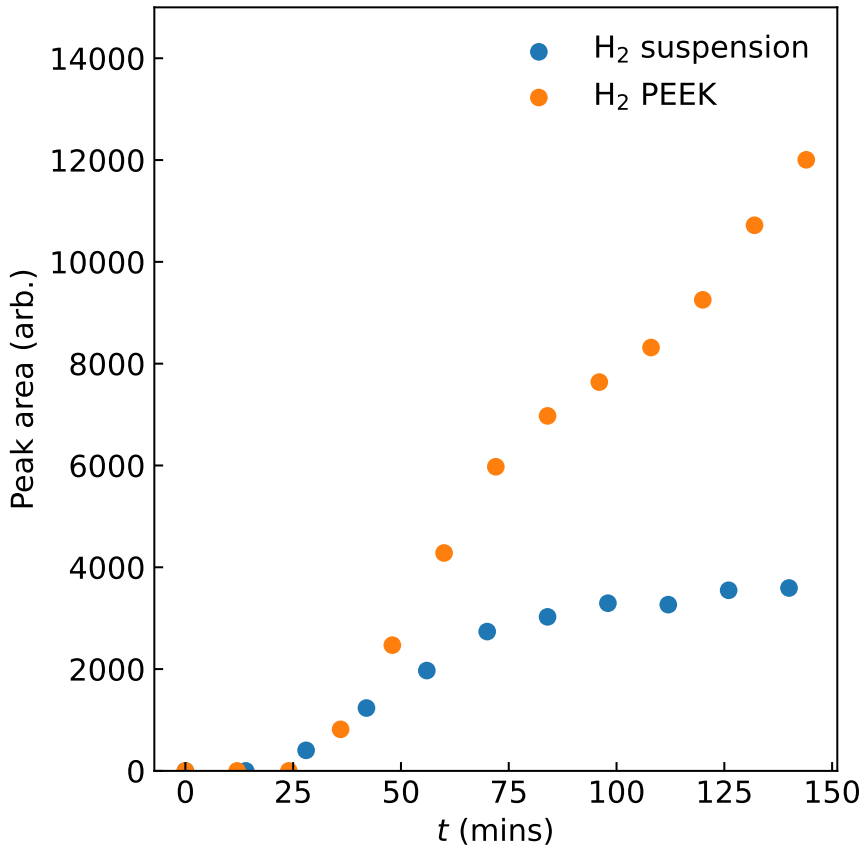

Figure 4.9: Hydrogen peak sizes measusred in the peek reactor(orange) during photocatalysis, compared to peak sizes observed in the suspension reactor using the same lamp(blue).

Over the course of approximately 10 photocatalytic experiments, the PEEK inserts to this reactor can be observed to discolor. After cleaning with soap, sonication and a range of polarity organic solvents, the discoloration remains, indicating this is not an adsorbate, rather the PEEK itself reacting during photocatalysis (Fig. 4.10). As the insert discolors, under the same reaction conditions as previous experiments, new peaks

are detected corresponding to CH_4 and CO (confirmed by GC-MS).

Figure 4.10: The PEEK insert after approximately 10 photocatalytic reactions (20 - 30 hours UV exposure) on the top (left), which is exposed to UV and houses the photocatalyst. This picture is taken after washing with soapy water, acetone, hexane, petroleum ether and sonication to ensure discoloration is not an adsorbate. Rear and side view (right), which is not exposed to any UV, due to being housed inside a stainless steel cavity. The top side shows color change indicating UV induced degradation.

To identify the source of the generated species and discoloration, GC injections are taken of the reactor and empty insert while exposed to UV irradiation, and shown in Fig.4.11, and compared to the catalysts from *Chapter 3*. From these measurements, it can be observed that when exposed to UV irradiation, PEEK degrades to produce significant amounts of H_2. The quantites of H_2 generated without catalyst present are more than an equivalent experiment with the catalyst present. This can be attributed to its ability to absorb almost the whole UV region, which can induce photoxidation reactions of the polymer.[124] This photodegradation is the cause of CO, CH_4 and H_2 which are detected by GC, and makes the reactor results unreliable. The time invested in this reactor exemplifies the phrase 'A day in the library saves a week in the lab'.

One approach to fix the reactor would be through changing the PEEK insert to another plastic, one which is UV- reflective, and stable. However, more optimisations for this reactor would also be desirable. The gas-in and gas-out lines are very close to the reaction suspension, due to the small headspace, which makes it prone to the highly problematic prospect of catalyst suspension flowing towards the GC, ruining the individual experiment and potentially the GC column. Such a small reaction vessel only houses 0.7 mL of methanol/H_2O solution, which over

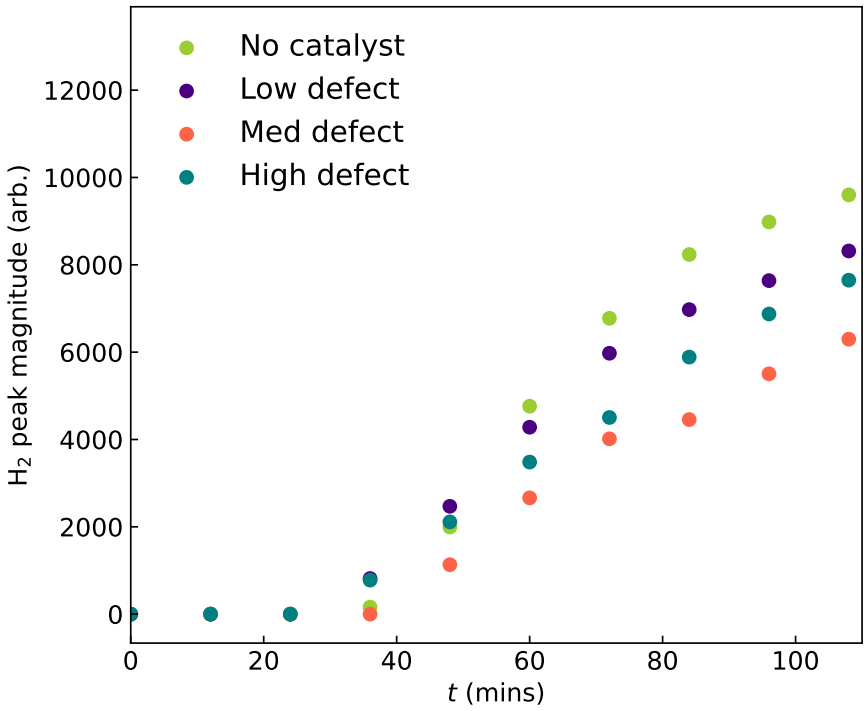

Figure 4.11: Hydrogen peak sizes in the peek reactor for the three platinum-deposited catalysts within the defect series from *Chapter 3*, suspended with 10% methanol in water. These hydrogen peak sizes are smaller than those detected from catalyst-free, blank experiment of PEEK UV irradiation.

the course of a long experiment, under gas flow and slight heating from the UV lamp will evaporate. While some liquid remains by the end of the experiment, the presence of electron donor and reactant of course effects catalyst activity.[125]

From the multiple iterations of reactor, the ideal reaction vessel was developed, taking all of these difficulties into account. The 'glass flat cell reactor' is depicted in Fig. 4.12, is designed to alleviate the previously described problems, while maintaining the thin film of catalyst and a relatively small headspace.

In this reactor, made of borosilicate glass (which is UV stable and tranparent in the region of the lamps emission) thin films of catalyst are immobilised onto glass slide with width=15mm and length=25 mm. 3 mg of catalyst is dispersed in methanol by sonication, and dropcast a single face of the glass slide and allowed to evaporate fully. This produces a thin film robust enough to maintain its structure through the whole process of catalysis, even with the catalysts submerged in 10% methanol for the reaction. 3 mg of catalyst on this glass slide produces a mean thickness of approximately 800 μm. Immobilisation ensures that

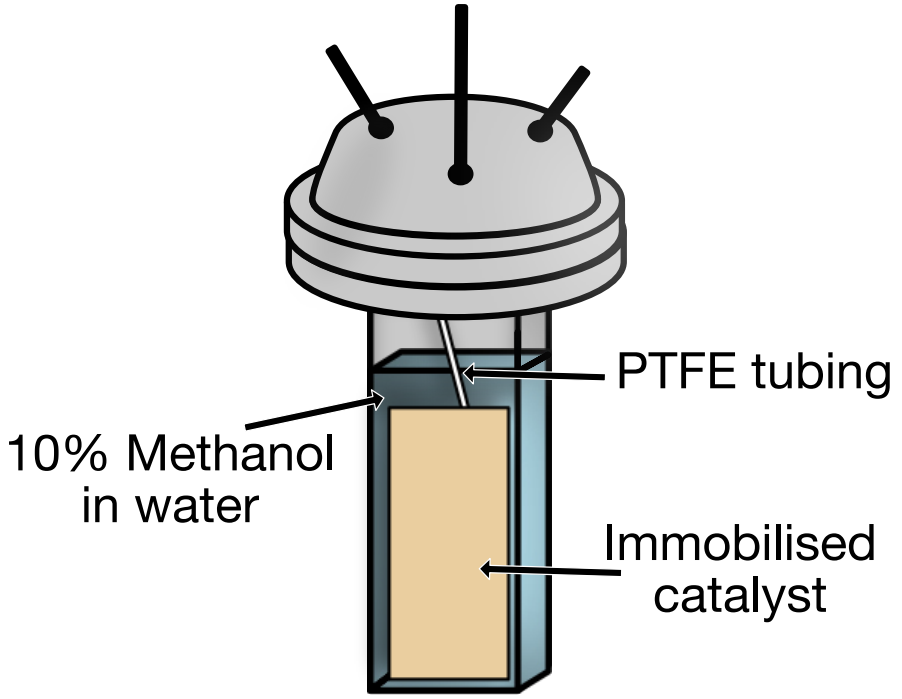

Figure 4.12: A diagram of the flat cell reactor, with catalyst dropcast onto a glass slide and exposed to UV from the side.

the thin film is retained, and light penetration is maximised, and with such thicknesses, UV light will illuminate all of the catalyst present. PTFE tubing to purge the reactor directly ensures that gases are efficienly removed from the solution, maintaining an oxygen-free atomsphere throughout the reaction. Finally, the catalysts are submerged in 20 mL 10% methanol, so that the very small amounts of evaporation observed do not affect product peak intensities.

This reactor yield increases the H_2 peak sizes from the same catalysts when compared to the PEEK reactor (even counting the hydrogen generated by PEEK photodegradation). This reactor has significantly larger headspace than the PEEK reactor (9 cm^3 compared to 1 cm^3), which would induce smaller peaks for the glass flat cell for identical activity catalysts. The increased photocatalytic activity observed is attributed the thin film generated when the catalyst is immobilised, and the ability for light to completely illuminate all of the catalyt present. The H_2 peak sizes are shown in Fig.4.13 for the PEEK reactor and glass flat cell, with identical flow rates and catalyst loadings of 2.8 –3.5 mg.

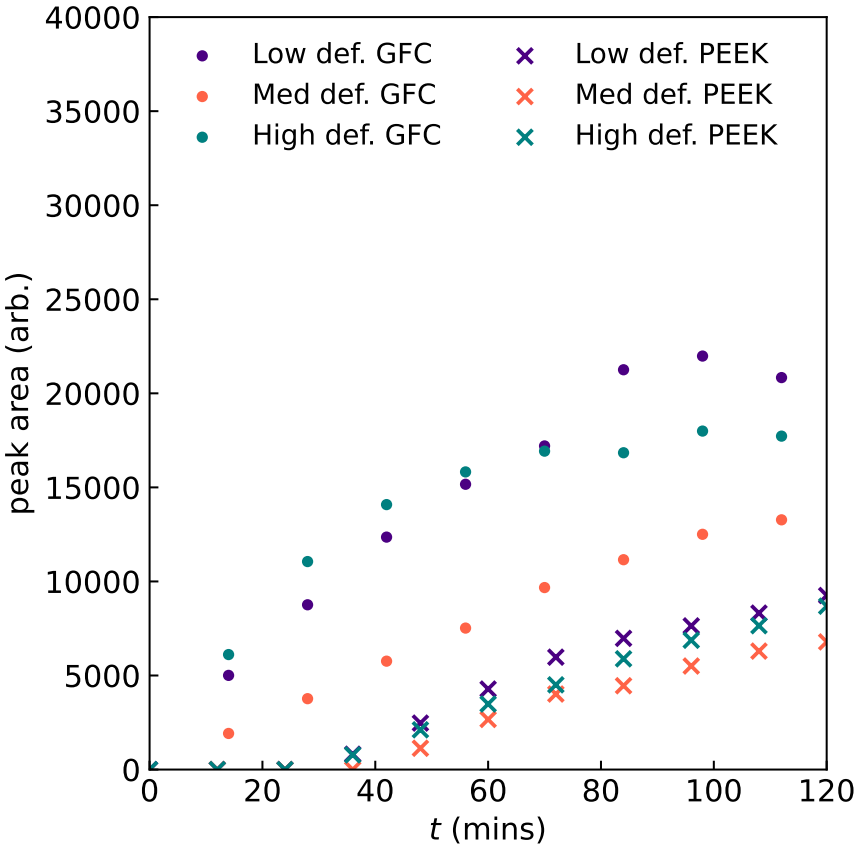

Figure 4.13: Hydrogen peak sizes in the glass flat cell reactor for the three platinum-deposited catalysts within the defect series from *Chapter 3*, suspended with 10% methanol in water. The same catalysts exposed in the PEEK reactor show significantly lower peak sizes.

4.4 Discussion

During the development of photocatalytic reactors, I discovered that the most influential paramter for hydrogen generation is light penetration, and maximising catalyst illumination throughout the whole reactor. Light penetration is limited by absorption and scattering. In the described suspension reactor, molar concentrations of the 2-aminoterephthalate linker (which is the chromophore) is of 1.78×10^{-4} mol dm^{-3}. The molar absoptivity (ϵ) of 2-aminoterephtalate is not listed in literature, but the 365 nm absorption band can be approximated by its intensity in a framework to similar to that of the 245 nm absorption band in terephtalic acid, which has a molar absoptivity of 12500 $M^{-1}cm^{-1}$. Through use of the Beer-Lambert law, this absorptivity is used to estimate the absoprtion from the photocatalyst as a function of path length into the catalyst. Fig.4.14 shows approximated transmittance through the reactor. For this approximation, the molar absoptivity was estimated at 12500 $M^{-1}cm^{-1}$, no missing linkers were included and scattering was not accounted for.

The transmission has inverse logarithmic correlation with path length, and is very low after path lengths of 1 cm, which is only a quarter of the full diameter of the suspension reactor. With scattering, the transmittance will be even lower. This shows that in the suspension reactor there is far more catalyst than is required, therefore the measured catalytic activity is lower than the catalyst can achieve. The catalyst is limited by the number of photons it can absorb, and to isolate the effects of chemical change on rates of photocatalysis, the catalyst should be limited by its rate, not the availability of photons. When reducing the amount of catalyst by a factor of 10 (from the suspension reactor to the glass flat cell), each chromophore has more photons available to induce photocatalysis.

This poor light penetration shows that large amounts of catalyst in this reactor will not be illuminated, therefore not catalytically active. The reactor types with much lower path lengths, such as the PEEK and glass flat cell are much better optimised to ensure that all catalyst is illuminated properly, while using less catalyst and the same amount of light.

While in these results suspension reactors produced reduced catalyst

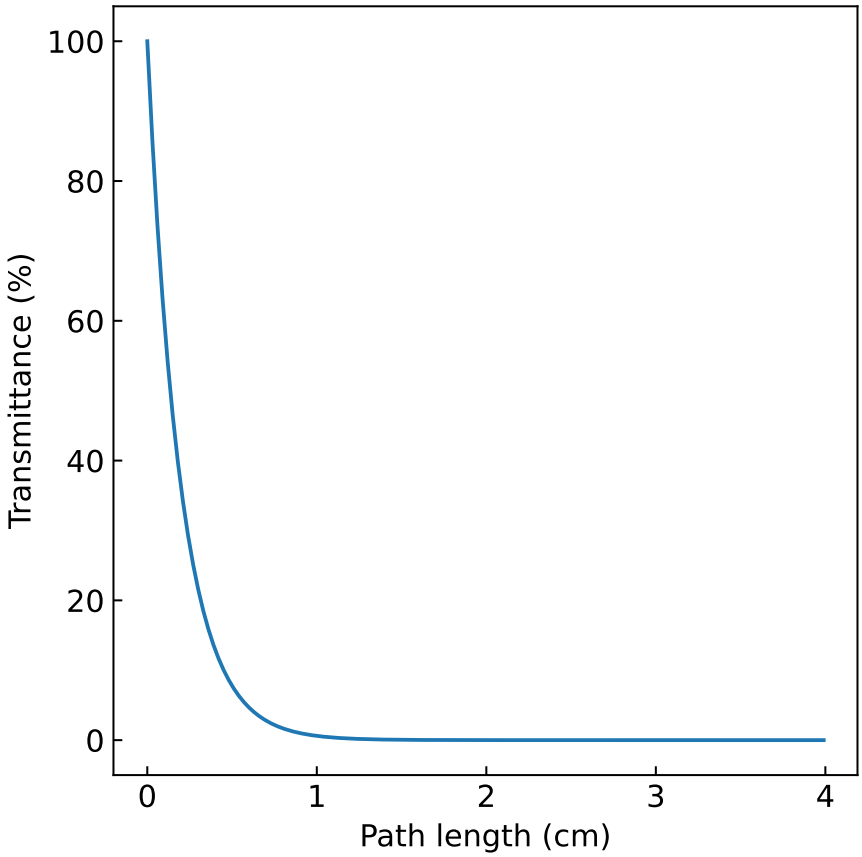

Figure 4.14: An approximation of the transmittance throughout the suspension reactor, using the molar absorptivity of terephtalic acid.

activity compared to immobilised catalysts, suspension reactors are still commonly used, reporting rates comparable to those achieved in this thesis with Pt @ UiO-66(NH_2) catalysts.[81] Using suspension reactors with lower concentrations of catalyst may improve the specific activity of a catalyst, as all of the light will still be absorbed.

The reduced catalytic activity for photocatalytic hydrogen generation in UiO-66(NH_2) using visible light is in agreement with most literature reports. Xiao *et al.* use a 300 W (6 times higher than that used in this research) Xe lamp, with a UV cutoff from 380 nm, where hydrogen generation rates are approximately 10 times slower than those reported in *Chapter 3*.[81] Similar rates of hydrogen generation are reported in a platinum-free UiO-66 @ $ZnIn_2S_4$ heterojunction catalyst under visible irradiation.[126]

Sui *et al.*[99] achieve rates of 4.5 $mmolg^{-1}$ of H_2 after 2 hours using a Pt/SnO_2/UiO-66(NH_2) composite under 300 W irradiation with a UV cutoff from 380 nm, rates which are higher than those achieved in *Chap-*

ter 3.[99] This lamp is used with a commercial suspension photoreactor, which (as-purchased) are with fitted measures to maximise photocatalytic activity, such as reflective cups for maximal irradiation. Sui *et al.* do not not have catalytic measurements for Pt @ UiO-66(NH_2), therefore it is difficult to conclude the improvements provided by the reactor design, and the catalyst improvements of SnO_2 addition to the catalyst; however they do show the ability to create UiO-66(NH_2) photocatalysts which generate appreciable amounts of hydrogen using visible light.[99]

The difference in H_2 peak magnitudes, and therefore the catalyst activity is very large in this chapter, which highlights the impact of reactor design on the reported rates of catalyst activity. Photocatalysis is very susceptible reactor changes, and results reported for each reactor type in this chapter exemplify the need for directly comparable photcatalysis results. It is impossible to deconvolve the impacts of catalyst and reactor in 2 separate photocatalysis procedures. With the wide range of photoreactors, lamps and specialised catalysts, it is very difficult to perform a replicate experiment of another in literature to precisely compare the results of a novel catalyst to those already reported. For reliable catalyst activity improvements independent of the reaction setup, comparisons to known, commercially available photocatalytic standards using the same method is the easiest way to have robust comparisons to other literature photocatlysts.

4.5 Conclusion

In this chapter, I optimised the photocatalytic reactor setup from one which produces almost no H_2, to one which reproducibly produces large, easily quantified and accurate H_2 peaks for quantification.

I established that this catalyst system benefits greatly from being immobilised, compared to suspended, and established the largest factor in original reactor iterations poor performance is the limited light penetration.

To create efficient photocatalytic reactors, it is clear from these experiments that the photocatalyst must be of a high aspect ratio, efficiently spreading the material across a thin layer to maximise the exposure of

catalyst to photons. This is why immobilised catalysts exhibited significantly higher specific rates of hydrogen generation when compared to suspended catalysts.

Minimising reactor headspace is a key parameter when aiming to maximise the amount of hydrogen detected in gas chromatography. This is useful when optimising the reactor for catalysts with poor activity, or when calibrations are not measured at particularly low concentrations, but headspace does not affect the rate of photocatalysis.

To further optimise this reactor, an important parameter is the delivery of photons from the lamp to the catalyst. This can be achieved through lamps with a lower angular divergence, focusing the beam more directly onto the catalyst to maximise exposure, or through use of reflective material focusing the beam onto the photocatalyst. UV exposure caused heating of the PEEK reactor, and will heat the reaction mixture, installing a water jacket to dissipate heat would ensure catalysis is only powered by photons.

We observe heating of the PEEK reactor, which caused leaks, however another consideration for heating is that it will provide energy to the catalyst, and will aid the rates of photocatalysis. Measures to reduce heating of the catalyst and reaction mixture would be beneficial to measure photocatalysis at room temperature. This could be achieved by increasing distance from the lamp (in unison with measures to maximise catalyst photon exposure), or by implementing a cooling system similarly to the Peltier cooler used in the PEEK reactor.

Chapter 5

Nickel-Platinum mixed-metal catalysts at UiO-66(NH_2) for photocatalytic hydrogen generation

5.1 Introduction

Chapter 3 investigated the path of cocatalyst size control for more sustainable catalysis, by reducing the amount of PGM required in photocatalytic hydrogen generation. Platinum is the most effective co-catalyst for photocatalytic hydrogen generation, however it is desirable to develop more sustainable and cost-effective co-catalysts for industrial viability.

In this Chapter, I present research aiming to replace, or partially replace platinum cocatalysts with nickel cocatalysts. Nickel is the fifth most common element in the earths crust, occuring naturally in soil and water, therefore is an ideal metal for catalysis, with little sustainability issues.[127] Nickel resources are also widespread around the world, making the price and availability less susceptible to geopolitical issues (but not immune), unlike other abundant catalysts such as cobalt.[128,129]

Mining one kilogram of platinum consumes 494,563 MJ energy and 297,006 kg blue water[8]. Mining one kilogram of nickel consumes 181.2 MJ energy and 103 kg total water.[130] To produce hydrogen in suitable quantities for hydrogen generation very large amounts of co-catalyst are

required. While eventually this co-catalyst would be recycled, large scale industrial processes using platinum will continue to motivate mining, and we must consider the life cycle of rare materials which we propose to use. Aside from the statistics for energy consumption, water consumption and so on, there is also the responsibility to maintain our sparse elements, reducing strain whenever possible.

Efficacy of cocatalysts for hydrogen generation is largely governed by their work function, as this controls how the band structure bends at interfaces, and how photoelectrons flow to the cocatalyst. Platinum has the highest work function of the PGMs.[40] The work function of platinum is 5.75 $\pm$0.06 eV, and the work function of nickel is 4.96 $\pm$ 0.10 eV, which is higher than comparably abundant metals such as iron (4.64 $\pm$0.05 eV) and aluminium (4.28 $\pm$ 0.05).[131] This makes nickel an attractive sustainable replacement for platinum in photocatalytic hydrogen generation. As such it has received attention in this application.

Ni cocatalysts have commonly been deposited onto perovskite supports for photocatalytic hydrogen generation, with the first instance of Ni cocatalysts in hydrogen generation using $SrTiO_3$ support.[132] A catalytic system 3 wt % Ni @ $NaTaO_3$ under UV irradiation achieved hydrogen generation rates of 9 $mmolh^{-1}g^{-1}$.[133] Other supports such as TiO_2 and CdS have been reported in multiple instances with Ni cocatalysts.

Studies on the crystal phases of nanoparticulate Ni revealed that the *hcp* phase provides a higher activity for photocatalysis than the more prevalent *fcc* phase.[134] This information can be deciphered on the relatively large suspended nanoparticles <20 nm in this research using TEM. The modern approach to heterogeneous catalysis typically involves supported nanoparticles of a smaller size. Between the often difficult to observe crystallinity of small nanoparticles and relatively weak electron scattering of Ni, local structure probing through EXAFS or PDF may be required to decipher the phase in smaller supported nanoparticles. Fig.5.1 shows the comparative rates for photocatalytic hydrogen generation of *hcp* and *fcc* nanoparticles of various diameters.

Research using Ni @ CdS nanorods analyzes the effect Ni nanoparticle size on photocatalytic activity towards hydrogen generation.[135] Decreasing particle size to the minimum reported (6 nm) induces higher rates of hydrogen generation (Fig.5.2), displaying clearly the atomic utilization principal, and showing the importance of reduced particle size for

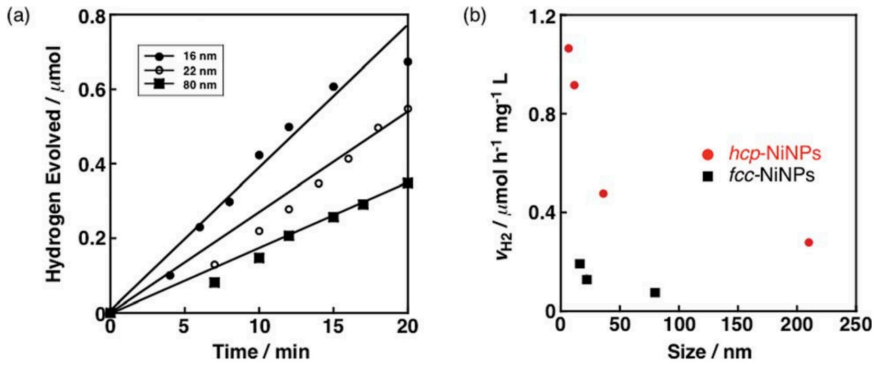

Figure 5.1: Activity of *hcp* and *fcc* Ni nanoparticles for photocatalytic hydrogen generation. Reproduced from ref [134]

sustainable catalysis.

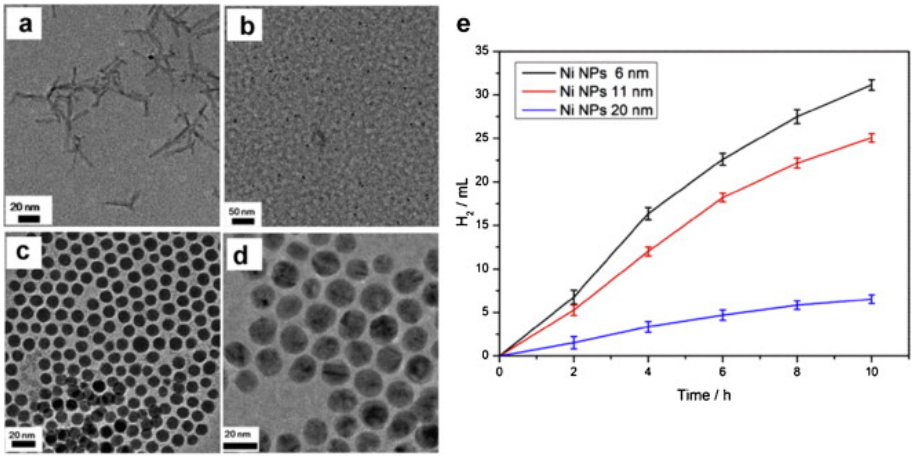

Figure 5.2: Hydrogen generation rates for nickel nanoparticles of different diamaters. Reproduced from ref. [135]

Nickel cocatalysts are reported for hydrogen generation in Ni (0) and Ni(II), with beneficial effects observed by applying both oxidation states simultaneously. Where a drawback of photocatalysts using only Ni(0) is that they have been observed to poorly utilize photoexcited holes, and addition of NiO enhanced the oxidative reaction to increase catalytic activity.[136]

The nickel based MOF Nickel phosponate (IEF-13) was designed and synthesised to generate catalytic activity in water splitting. The structure is shown in Fig. 5.3, with Ni-based nodes co-ordinated to water, which can provide Bronsted acidity similarly to hydrated UiO-66.[137]

Nickel and platinum have been used to create alloys for catalysis in hydrogen generation and other applications.[138,139] These alloys have shown high activity towards hydrogen generation in multiple phases, while reducing the amount of platinum needed in this reaction.[140]

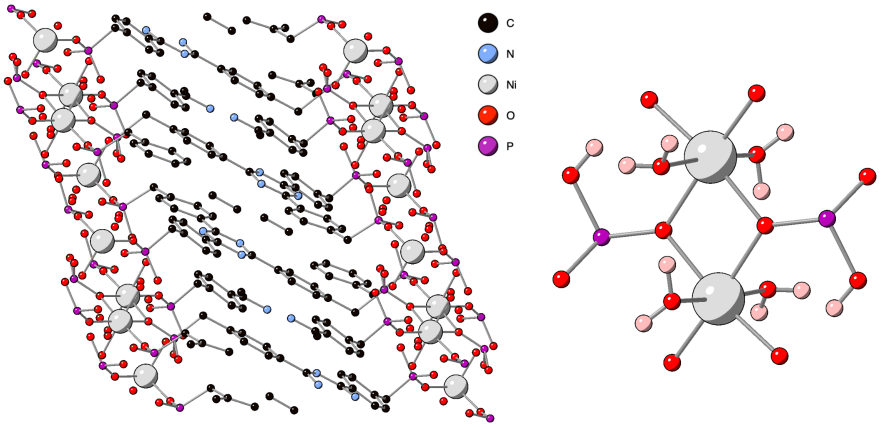

Figure 5.3: (left) the structure of IEF-13, a Ni containing MOF designed for photocatalytic hydrogen generation.(right) The co-ordination of the Ni nodes for IEF-13. Reproduced from ref. [137]

The support material which gave the highest catalytic activity in *Chapter 3* was low defect UiO-66(NH_2). In this chapter, low defect UiO-66(NH_2) is applied to photocatalytic hydrogen generation using Ni, Pt and various ratios of these metals as co-catalysts to assess the feasability of Pt replacement with Ni.

5.2 Results

The catalyst support used in this chapter is the low defect UiO-66(NH_2) reported in *Chapter 3*. This support material was deposited co catalysts using magnetron sputtering. A series of catalysts were created, with deposition of Ni, Pt and simultaneous sputtering of both metals in the ratios 1:3, 1:1 and 3:1 Ni:Pt. Simultaneous deposition is chosen to provide mixing of these metals at the support material, and minimising the quantity of monometallic domains, maximising the synergic effects of the bimetallic cocatalyst system.

PXRD patterns of the catalyst series, and the non-deposited UiO-66(NH_2) are shown in Fig.5.4, with the high Q region zoomed on the right. The support crystal structure remains unchanged after deposition, and there are no reflections present related to Pt, Ni or their oxides.

Energy dispersive X-ray spectroscopy (EDX) mapping of the Ni and Pt in bimetallic catalysts are shown in Fig. 5.5. Ni and Pt are deposited with effective mixing of metals, with no indiciation of monometallic do-

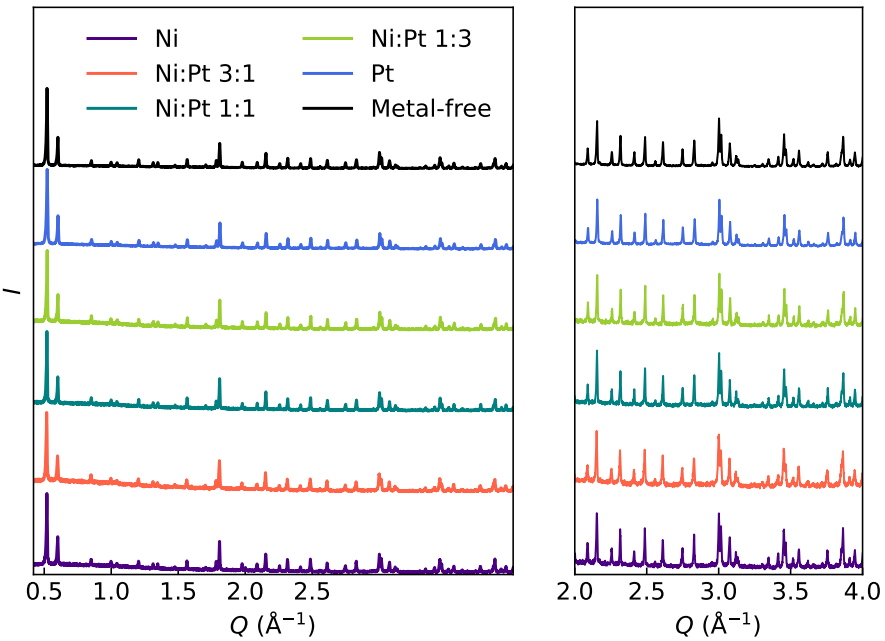

Figure 5.4: PXRD patterns for UiO-66(NH_2) deposited with each platinum: nickel ratio and a pattern for the non-deposited UiO-66(NH_2). On the right, the high angle region is zoomed (and intensity multiplied by three) to highlight the non-existence of any reflections from Pt, Ni or alloys thereof.

mains, maximising any chances of synergistic catalysis between metals. Effective mixing of Pt and Ni was achieved by simultaneous deposition in magnetron sputtering, and through thorough powder stirring, using a more effective technique than deposition in *Chapter 3*.

TEM imaging of the catalysts and particle size fitting of the visible particles was conducted, TEM images of each catalyst is shown in Fig. 5.6, with additional images provided in the appendix for this chapter. All samples show nanoparticles uniform size distribution, localized on the surface of UiO-66(NH_2).

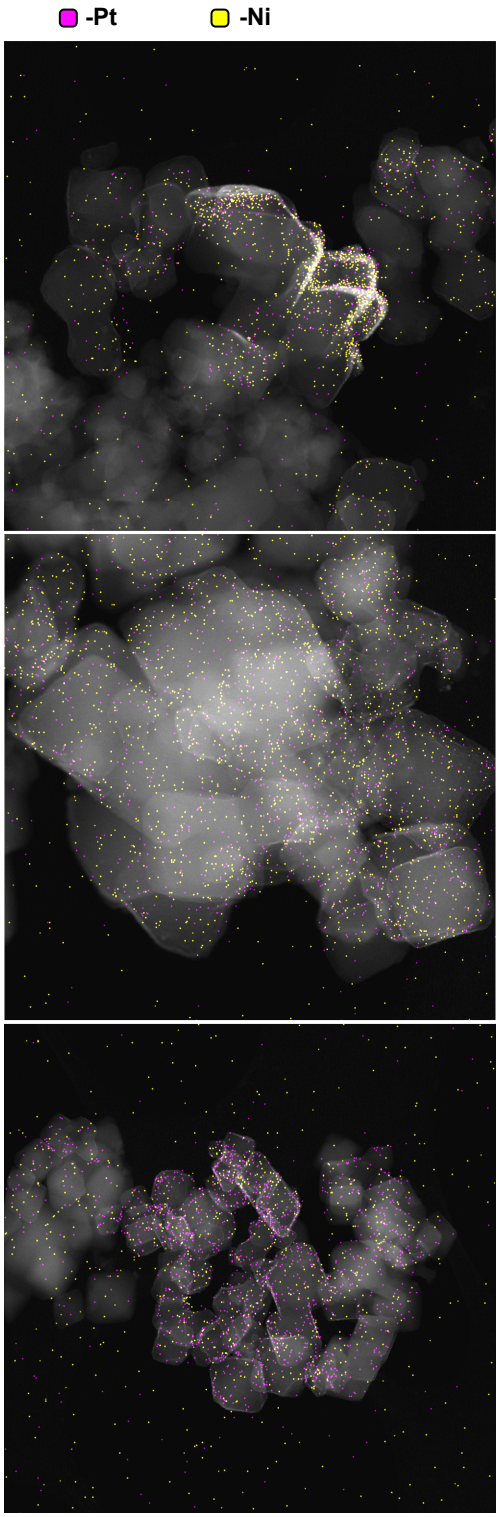

Figure 5.5: EDX mapping images of UiO-66(NH_2) deposited with (top to bottom) , Ni:Pt 3:1, Ni:Pt 1:1, Ni:Pt 1:3. Purple indicates Pt, and yellow indicates Ni.

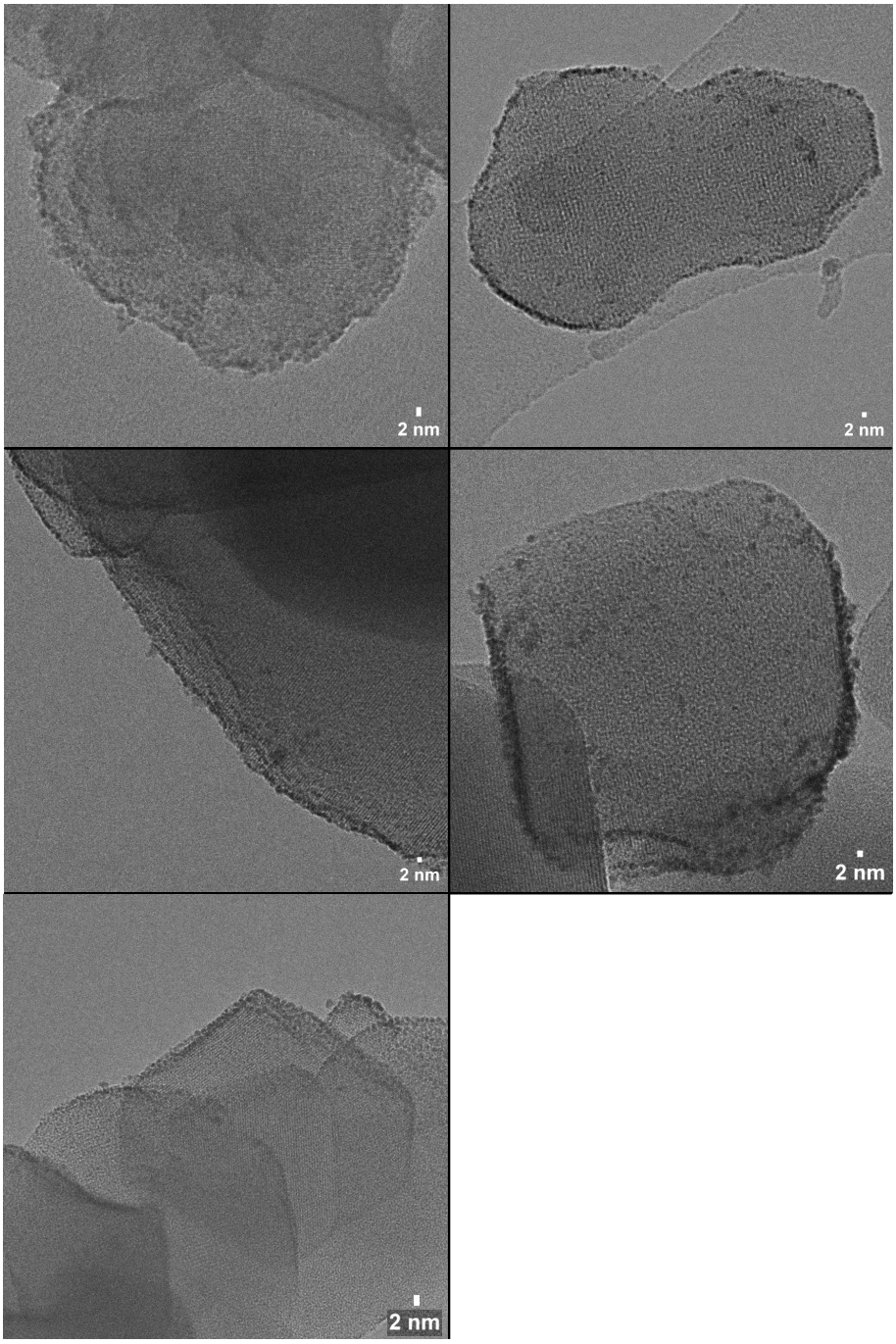

Figure 5.6: TEM images of UiO-66(NH_2) deposited with Ni (top left) , Ni:Pt 3:1 (top right), Ni:Pt 1:1 (middle left), Ni:Pt 1:3 (middle right) and Pt (bottom left).

Histograms for the particle size measurements are shown in Fig. 5.7. Each catalyst was fitted with only one lognormal distribution. While it is possible the bimetallic systems contain distinct particle types (Ni, Pt or alloys thereof), the particle size measurements do not provide evidence for multiple distinct particle sizes. The resolution of TEM, and errors introduced when measuring against strongly electron-scattering support materials mean that I cannot confidently fit bimodal distributions here. The mean particle sizes for each catalyst are listed in Table 5.1.

Sample	Mean particle diameter (nm)
Ni	3.0(3)
Ni:Pt 3:1	2.5(2)
Ni:Pt 1:1	2.3(2)
Ni:Pt 1:3	2.6(2)
Pt	2.1(2)

Table 5.1: Mean particle sizes measured by TEM and calculated through fitting to a lognormal curve.

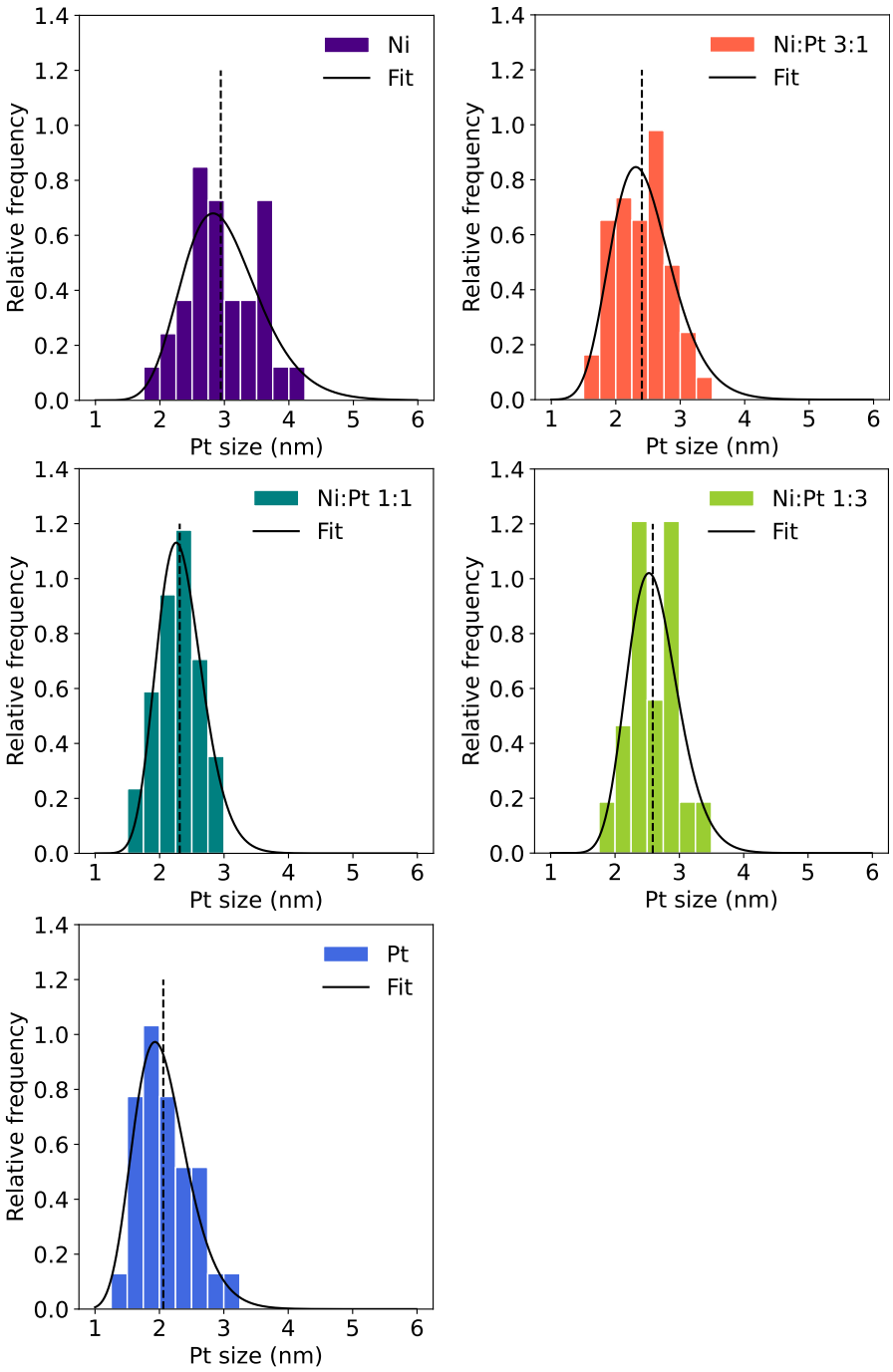

Figure 5.7: TEM particle size histograms of UiO-66(NH_2) deposited with Ni (top left) , Ni:Pt 3:1 (top right), Ni:Pt 1:1 (middle left), Ni:Pt 1:3 (middle right) and Pt (bottom left).

The particle sizes are notably larger for those measured in the pure Ni sample than all others. This may not be a true representation of the real particle distribution. As established in *Chapter 3*, strong scattering of UiO-66(NH_2) and low dose electron microscopy makes small particles difficult to observe in TEM. This effect is more pronounced with Ni particles than Pt, due to the weaker electron scattering of Ni. TEM images clearly show this phenomenon (Ni NPs show similar little contrast to the MOF background, while Pt and Pt-containing NPs are darker). With Ni weaker scattering than Pt, it is possible that smaller particles of Ni are less frequently observed.

UV-vis DRS shows that all samples absorb similarly in the low energy UV region, which is the required absorption for use with the 365 nm UV lamp in photocatalysis. Increasing quantities of Pt show small increases in absorption in the desired range, likely caused by surface plasmon resonance from the Pt nanoparticles.[141]

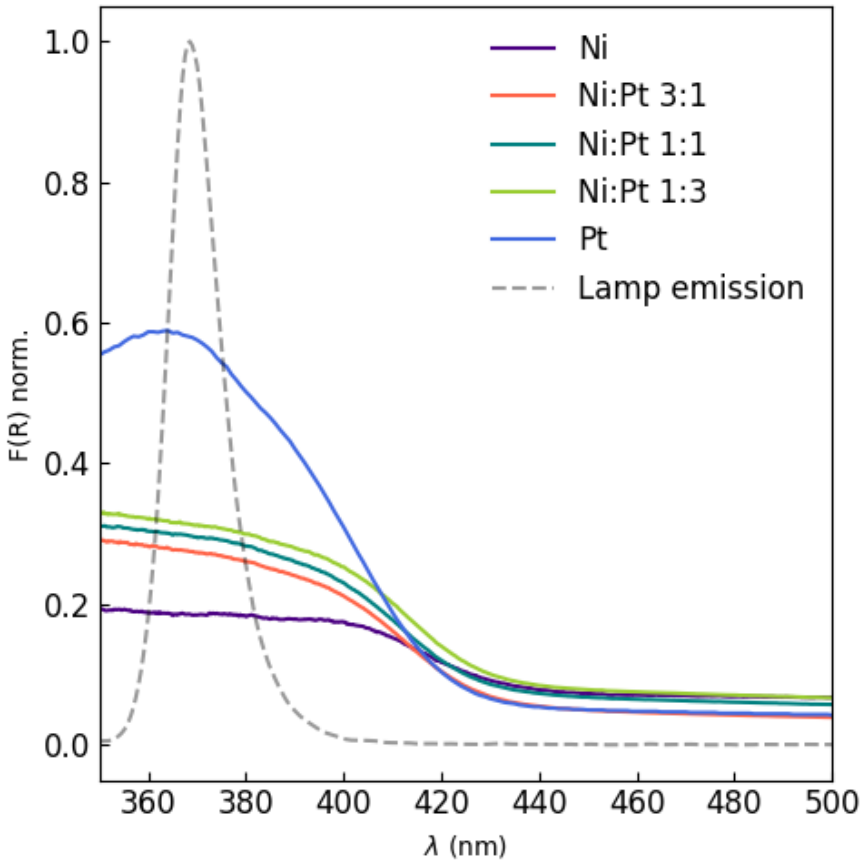

Figure 5.8: UV visible spectra for the Ni:Pt @ UiO-66(NH_2) catalyst series.

To better characterise the size and character of cocatalyst nanoparticles, each catalyst was analysed using PDF, with the PDF data for each

shown in Fig. 5.9

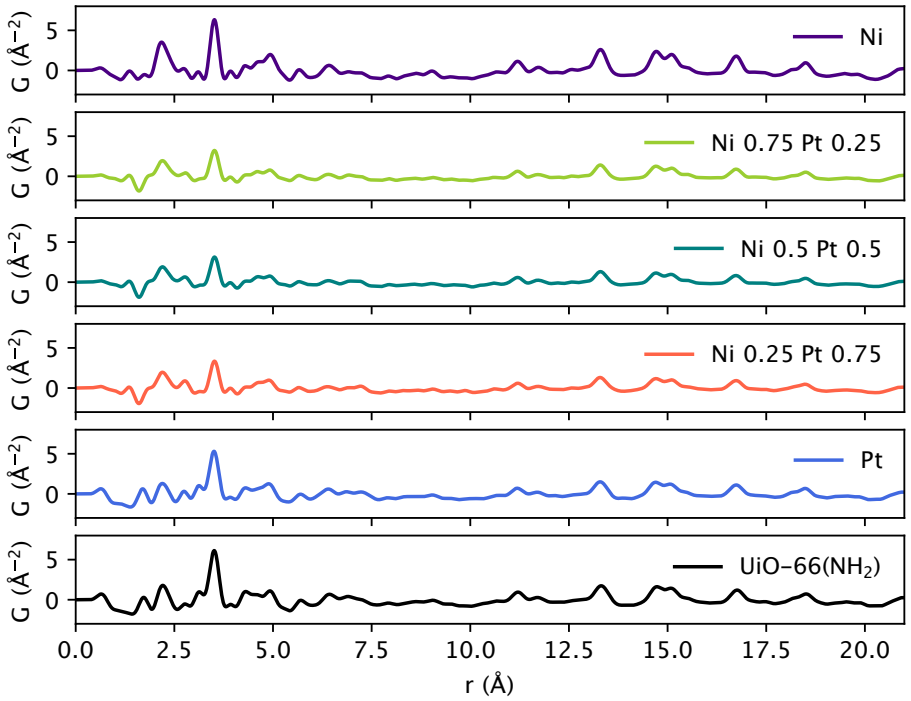

Figure 5.9: PDF data for UiO-66(NH_2) deposited with (top to bottom) pure Ni , ratios of Ni 0.75 Pt 0.25, Ni 0.5 Pt 0.5, Ni 0.25 Pt 0.75 ratios and Pure Pt.

This data is composed of analysis from two different experiments at Diamond Light Source, one measuring Pt @ UiO-66(NH_2) and UiO-66(NH_2), the other experiment measures Ni containing samples on the same support material. In the experiment for Ni - containing catalysts, the synchrotron current was lower (200 mA) than that of the non-deposited UiO-66(NH_2) and Pt @ UiO-66(NH_2) (300 mA). The synchrotron current is a factor which cannot be controlled by visitors or beamline scientists, and will dictate the intensity of scattering obtained. The glass for each experiment is also physically slightly different (even though they are both borosilicate), background signal for which is a great contributor to PDF analysis at low r. These factors together produce some minor differences between the PDF of Ni containing samples and the others, such as the negative peak observed in UiO-66(NH_2) and Pt @ UiO-66(NH_2) at 1 - 1.5. A significant difference caused by experimental changes is the peak at 3.14 Å (on the left shoulder of the Zr - Zr peak, which is the largest.) These changes in the PDF, which are caused by small changes in the reaction setup mean that subtraction of the non-deposited UiO-66(NH_2) to generated d-PDF is impossible, as these (relatively) small changes are significantly larger than the catalyst-related correlations.

Using the equation:

$$\mathrm{PDF}_{\mathrm{Pt}} = x\mathrm{PDF}_{\mathrm{Pt/MOF}} - \mathrm{PDF}_{\mathrm{MOF}}, \tag{5.1}$$

subtractions to isolate cocatalyst-related correlations were attempted, with the results in Fig.5.10.

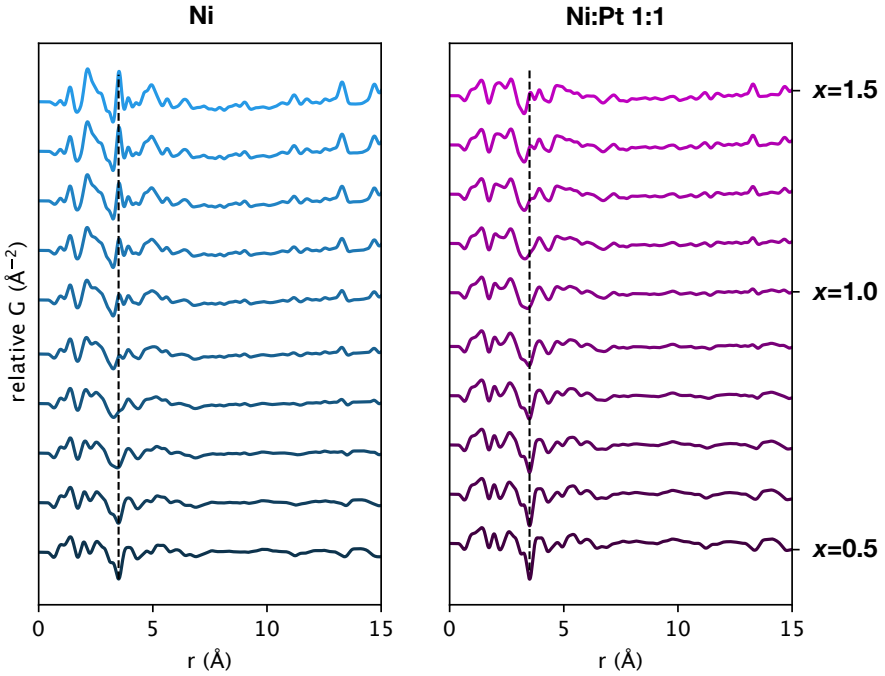

Figure 5.10: Subtractions of the UiO-66(NH_2) PDF from Ni @ UiO-66(NH_2) (left) and Pt:Ni 1:1 @ UiO-66(NH_2) (right) with varying values of x.

In *Chapter 3*, the low defect support material showed significant sintering in the early stages of catalysis under UV irradiation. In an attempt to replicate this sintering, and characterise the nanoparticle growth, 2 PDF experiments were conducted with in-situ PDF analysis while exposing the catalysts to elevated temperatures of 150 °C. This temperature was chosen, as it is one where the framework is stable for long periods, but the thermal energy is sufficient to provide nanoparticle mobility so that nanoparticle sintering (or dispersion) can occur. Specifically, this experiment would provide information on the rate of sintering, its magnitude, information on the phases of metals produced, and the nature of Ni and Pt in the mixed metal systems.

Ni @ UiO-66(NH_2) and 1:1 Ni:Pt @ UiO-66(NH_2) were heated from RT to 150 °C over the course of 60 minutes, then held at 150 °C for 2 hours. During ramping and heating, PDF measurements taken continuously, binned into 1 minute datasets throughout. Fig. 5.11 shows a heat map

for each measurement, where color represents the intensity of peaks at a given r. From the PDF measurements, no observable changes can be noted. The peaks relating to UiO-66(NH_2), particularly Zr related correlations, are too intense, drowning out any potential signal from nanoparticles.

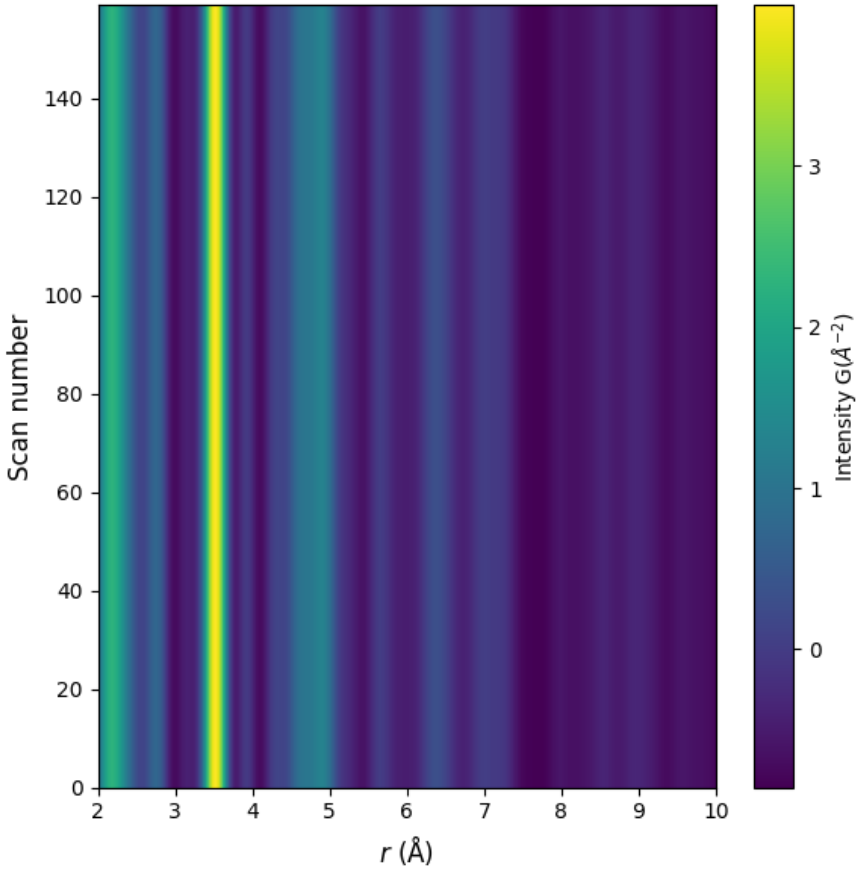

Figure 5.11: Pair distributions functions of Ni UiO-66(NH_2), taken every minute at 150 ^{o}C, and the peak intensities are translated to colours.

When a material is heated, its thermal parameters increase, which causes broadened peaks in XPDF. We might also expect to observe thermal effects on lattice parameters for both the MOF and nanoparticles. I create a d-PDF heat map to isolate any changes in PDF data when held under temperature. Each PDF was normalised to its maximum intensity (always at 3.5 Å), and the normalised mean for the first 5 scans at 150 °C was subtracted from every normalised scan, this ignores any changes which could occur in the ramping period, but avoids errors from temperature change.

d-PDF heat maps for Ni and NiPt1:1 @ UiO-66(NH_2) are shown in Fig.5.12. This shows any changes in the PDF that evolve from being

held at 150 °C. A different color scheme is for this purpose, where white represents little to no change, red indicates increased intensity and blue indicates decreased intensity when compared to the first 5 scans at 150 °C. In this d-PDF heat map, we expect the only changes to be due to mobile NPs, which would produce vertical lines of changing intensity where peaks grow/ reduce. Sintering forms larger crystallites, which produce larger peaks relating to nanoparticle correlations. Any sintering would cause the r of their correlations to increase with scan number. No such changes can be observed, indicating almost no sintering. The data in these heat maps is clearly quite noisy, there is no physical basis for red streaks moving diagonally (no new peaks appear), also at a constant r value the d-PDF can be negative or positive.

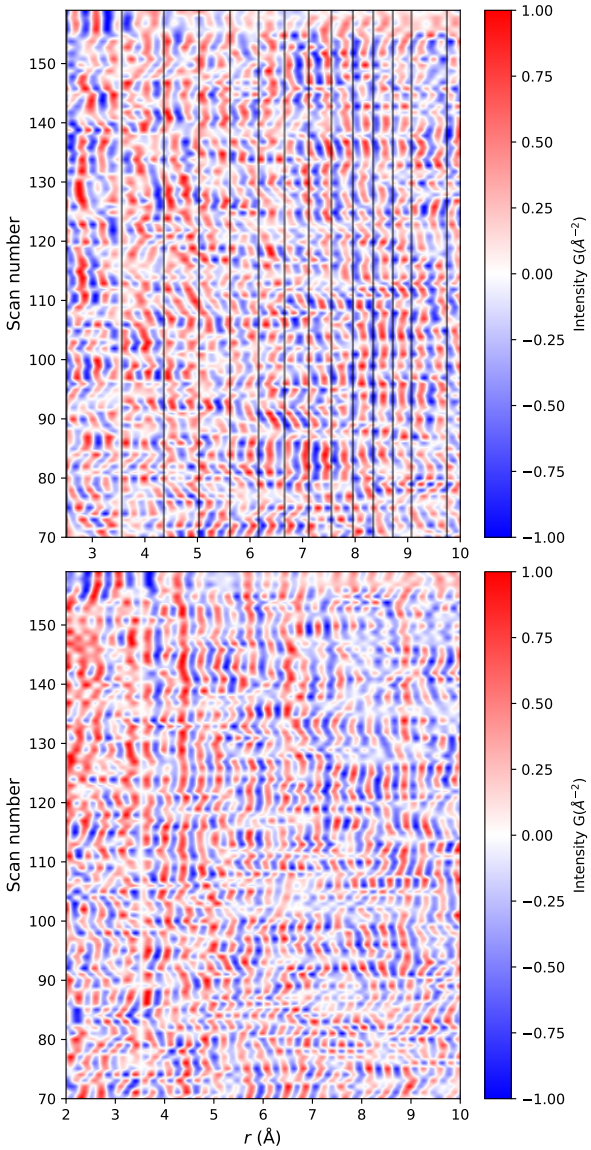

Figure 5.12: d-PDF heat maps of Ni@ UiO-66(NH_2) (upper), and Ni:Pt 1:1 @ UiO-66(NH_2) (lower).

When applying the Ni and Ni:Pt catalysts to photocatalytic hydrogen evolution, it is clear that replacement of Pt with Ni reduces the photocatalytic activity of the catalysts. Ni:Pt 1:1 and 1:3 show very similar activity towards hydrogen generation. When considering the trend from Ni and Ni 3:1 , Ni:Pt 1:1 is approximately where it would be expected, it is the Ni:Pt 1:3 that shows lower activity than would be expected.

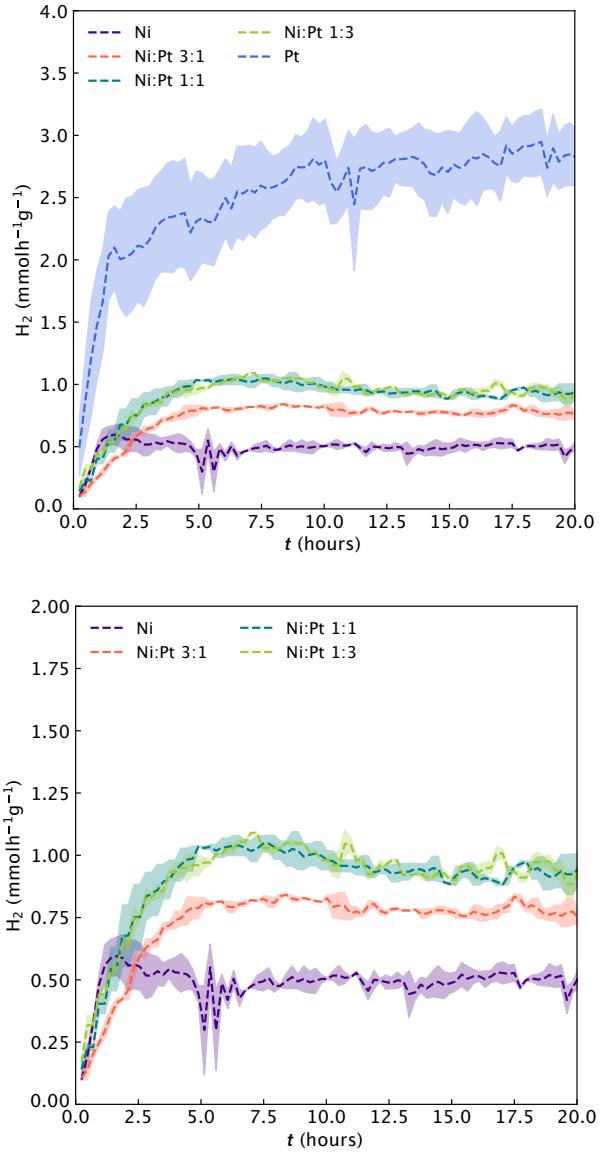

Figure 5.13: Rates of hydrogen generation for the PtNi-deposited series of catalysts under 365 nm UV lamp irradiation.

5.3 Discussion

Simultaneous deposition of Pt and Ni shows a good distribution of metals from the EDS maps. The lack of mono-metallic regions maximises the opportunity for alloy formation and synergic effects.

Pair distribution function analysis of these materials was anticipated to be difficult. The potential for a mixture of phases of nanoparticles present means that any individual phase has proportionally lower scattering, therefore is harder to observe. The lower scattering factors of Ni compared to Pt also contribute a weaker signal than those observed for the nanoparticles in *Chapter 3*. The subtractions of UiO-66(NH_2) from each catalyst in this series were not possible to isolate the co-catalyst related correlations. While glass has its most prominent PDF peak at 1.6 Å, the Si-O bond length, there are more diffuse features at longer range which are not easily noticeable until subtractions are performed.[142] These diffuse features vary greatly between different glasses of the same kind, and in this case the difference was so great that subtractions could not be performed, as the correlations in each glass did not align. As such, the nanoparticle structure cannot be observed, and the phase(s) of Ni and Pt in the sample were not discovered.

The PDF studies of Ni and 1:1 Ni:Pt at 150 °C showed no change in any peaks for 2 hours of heating. The 1 minute scans produce well defined PDF patterns, and the MOF related peaks are clearly observed. Despite the extensive sintering observed in *Chapter 3* using this support material, none was observed in PDF measurements. This raises many questions and opportunities for future work with these kinds of experiments. The sintering was observed under UV light, immersed in solvent and while actively catalysing a reaction, but under only heat, no sintering is observed. 1 minute PDF scans are relative short, even in a third-generation synchrotron such as Diamond Light Source, and while the PDF data is well resolved, most of the PDF is MOF. With d-PDF analysis of nanoparticles, one must extract as much information from the sample as possible, and longer scan times can achieve better signal:noise, which is necessary for in-situ d-PDF. The noisy data is particularly clear in the earlier scans, where the is little time for the sample to change, and the heat map should be mostly white, but blue and red spots appears throughout.

It is established that co-catalysts can contribute light absorption through SPR.[141] The photons absorbed directly to co-catalysts during photocatalysis could be the observed mechanism for sintering with this support material. Alternatively, sintering could be aided by the present solvent, as commonly observed in Pd catalysts.[143]

The Ni, and Ni:Pt catalyst series generally follows a linear trend for activity towards hydrogen generation correlated with the proportion of Ni present. Ni:Pt 1:3 is the exception to this trend. There are 2 alloys reported for Ni:Pt in 1:1 ratios on Inorganic Crystal Structure Database, and one each for the ratios Ni:Pt 1:3 and 3:1[144] The linear trend observed in Ni, Ni:Pt 3:1 and Ni:Pt 1:1 would lead to the assumption that these show samples have little to no alloy present, and synergic effects between co-catalyst metals is minimal. Ni:Pt 1:3 not fitting the same trend could be a sign that an alloy is present, and its catalytic activity towards hydrogen generation is less active than the sum of its parts. Unfortunately, the PDF subtractions were not possible, therefore the phases cannot be characterised with any certainty.

5.4 Conclusion

In this chapter, I have investigated the catalytic properties, and nanoparticle characteristics of Ni, Pt and their mixed metal co-catalysts on low defect UiO-66(NH_2). PDF to elucidate the character of nanoparticles was unsucessful, due to small experimental differences between experiments investigating the support material and its metal-deposited analogues. Under 2 hours of heating at 150 °C, PDF experiments revealed no sintering, despite significant sintering being observed after 2.5 hours of photocatalysis on the same support material. The in-situ experiments to measure particle sintering are limited by the duration of each scan (60 seconds), which produces noisier data than is required. When investigating diffraction of Ni NPs on a Zr-based support, the Ni will always be hard to detect due to its weaker X-ray scattering. Increasing the length of each individual scan would help to better resolve the co-catalyst NPs, and any structural changes could become more significant than noise in the data.

Conclusions and future work

This thesis presents a synthetic procedure to systematically control the concentrations missing linkers in UiO-66(NH_2), which is not present in literature. The application of these defects to reduce sintering in catalysis was sucessful for catalyst nanoparticles, and shows promise as a technique to make longer-lived catalysts. The introduction of point defects to state-of-the-art support materials is an opportunity to make highly active catalysts more sustainable, through the possibility for longer lifetimes and therefore less common recycling.

Nanoparticle analysis presented highlights the use of PDF as a synergistic tool with TEM for their characterisation. The use of PDF for nanoparticle analysis is rarely seen, and most commonly TEM is relied upon as the sole technique for particle size analysis. TEM gives a real view of the nanoparticle distribution, and often that of SACs, which makes it often enough data. The approach using both techniques is beneficial for many reasons, removal of (or data which challenges) bias in TEM, accessibility to beam-sensitive and strongly electron scattering supports, information on phases of nanoparticles, crystallinity, local structure and an overall view of the whole catalyst is all information which can complement particle size distributions. Complementary analysis for NP structure elucidation between XPS, PDF and TEM provides evidence that Pt NPs @ UiO-66(NH_2) are composed of Pt^0 core material, and an oxidised, highly disordered Pt outer shell. The research in this thesis established that there is no interface between Pt NPs and UiO-66(NH_2) that can be crystallographically defined. XPS data before and after catalysis and TEM particle sizing shows that defects do provide anchor sites at which the Pt NPs interact, and the defects do stabilise Pt NPs.

d-PDF works well for Pt NPs, because Pt is so strongly X-ray scattering. Zr atoms scatter X-rays more strongly than most metals used as

MOF nodes, therefore the PDF from UiO-66(NH_2) is intense. Intense MOF scattering creates more challenging d-PDF methods. Using this approach to understanding defects and interfaces, more information may be extracted from MOFs with lower atomic number metal nodes. UiO-66(NH_2) was chosen for its stability, however there are many MOFs stable with respect to water and light. A material with larger pores could allow for better co-catalyst integration with the internal surface area. An ideal candiadate (which has already been used in photocatalysis) with good stability, relatively low atomic number nodes, favourable band structure for photocatalytic hydrogen generation and larger pores than UiO-66(NH_2) is MIL-101(Fe), which contains the same UV absorption band as UiO-66 family MOFs, and a wide range across the visible spectrum.[145]

Chapter 6

Appendix

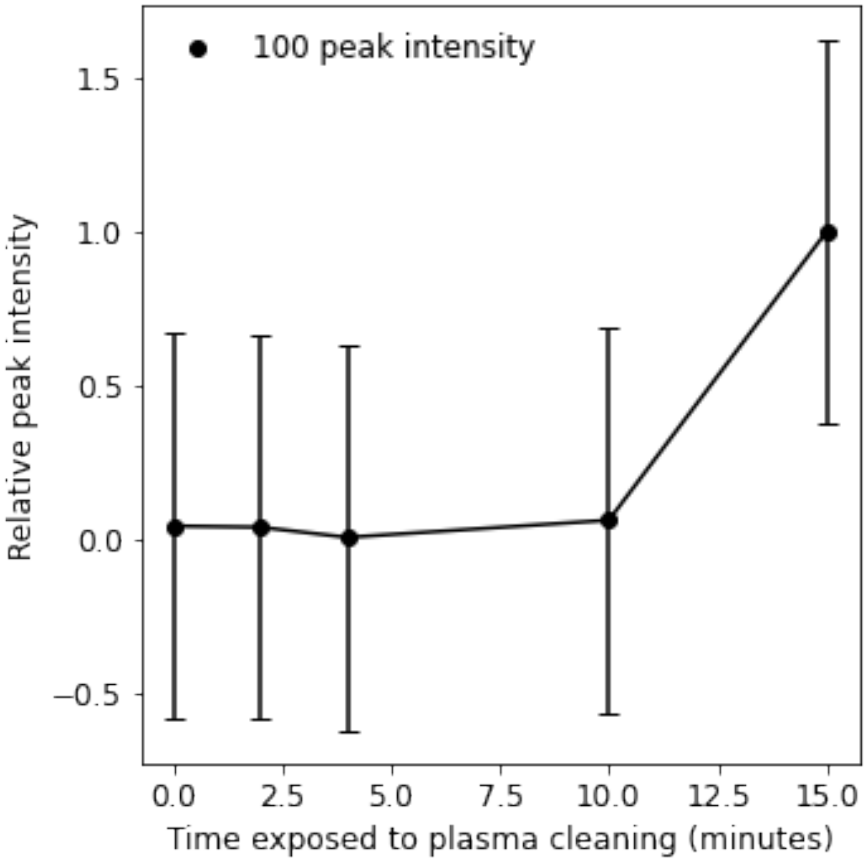

Figure 6.1: Peak intensity for *100* peaks of UiO-66(NH_2) when exposed to plasma cleaning for different durations. Peak intensity calculated through peak phase Pawley refinement, errors calculated through TOPAS Academic.

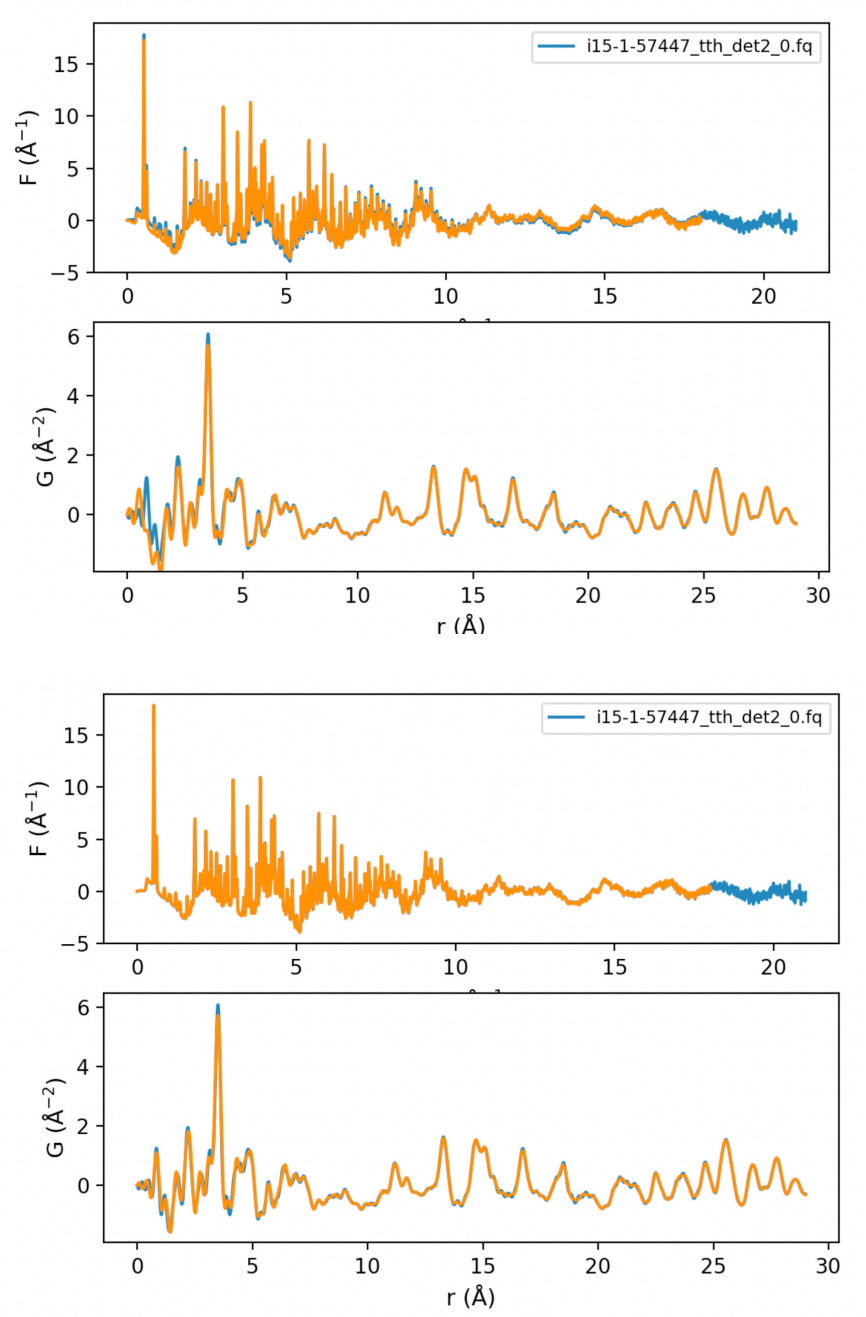

Figure 6.2: Data processing of PDF data, where blue is non-adjusted data and orange is after applying processing parameters: Both samples are processed with Q_{max}=18 (upper) The F(Q) and G(R) for a sample processed with rpoly=0.8. (lower) The F(Q) and G(R) for a sample processed with rpoly=1.0.

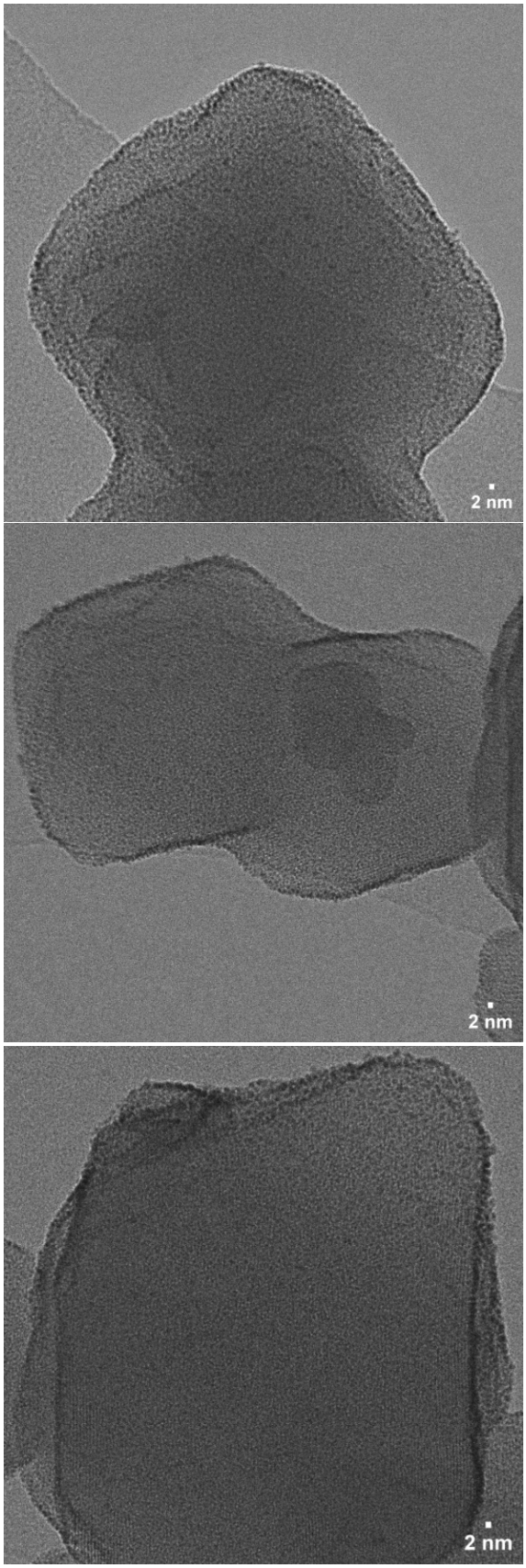

Figure 6.3: Supplementary TEM micrographs of Ni:Pt 0.25:0.75 @ UiO-66(NH_2), which images were used to measure particle sizes.

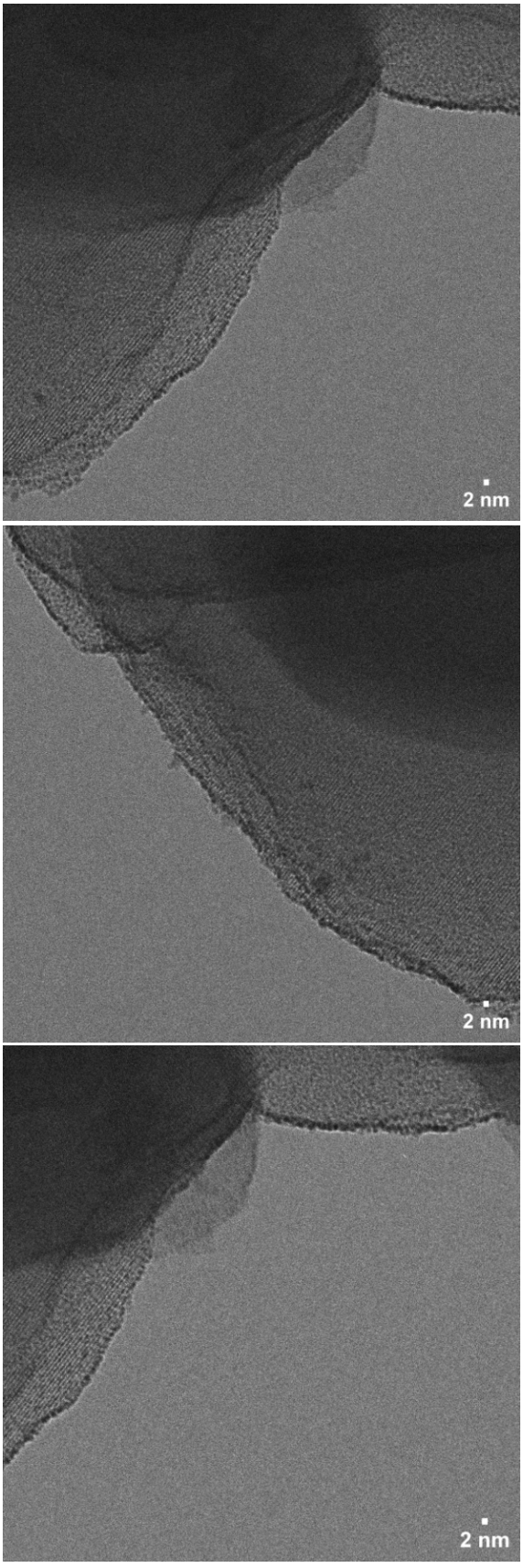

Figure 6.4: Supplementary TEM micrographs of Ni:Pt 0.5:0.5 @ UiO-66(NH_2), which images were used to measure particle sizes.

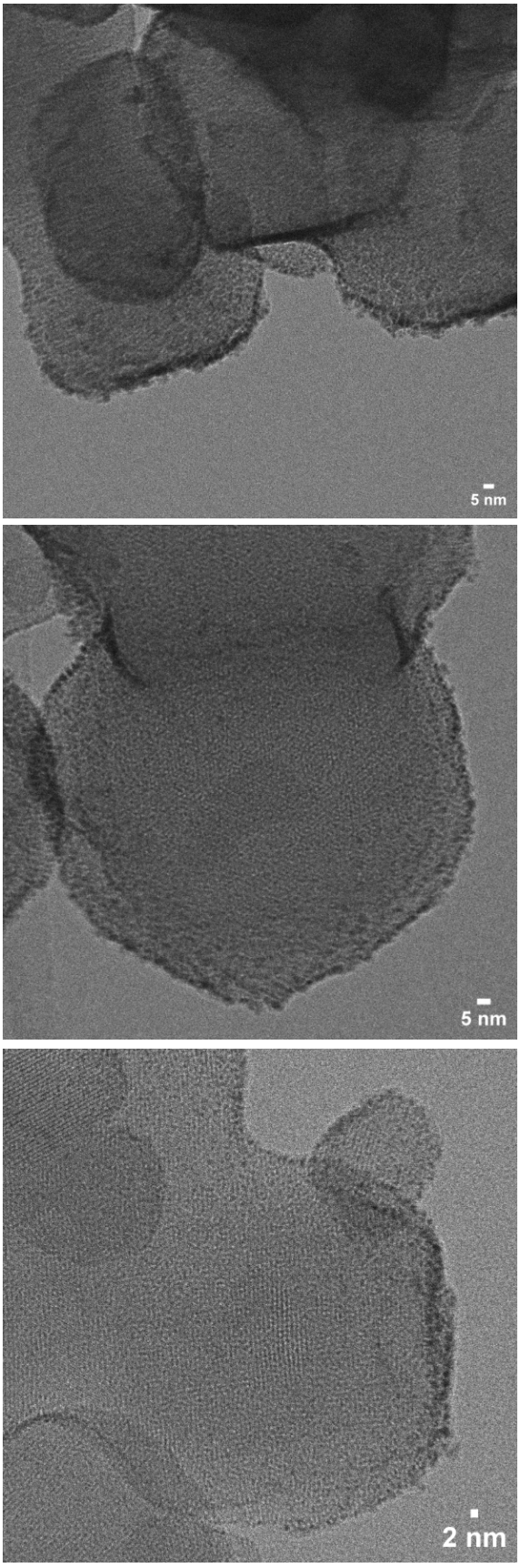

Figure 6.5: Supplementary TEM micrographs of Ni:Pt 0.75:0.25 @ UiO-66(NH_2), which images were used to measure particle sizes.

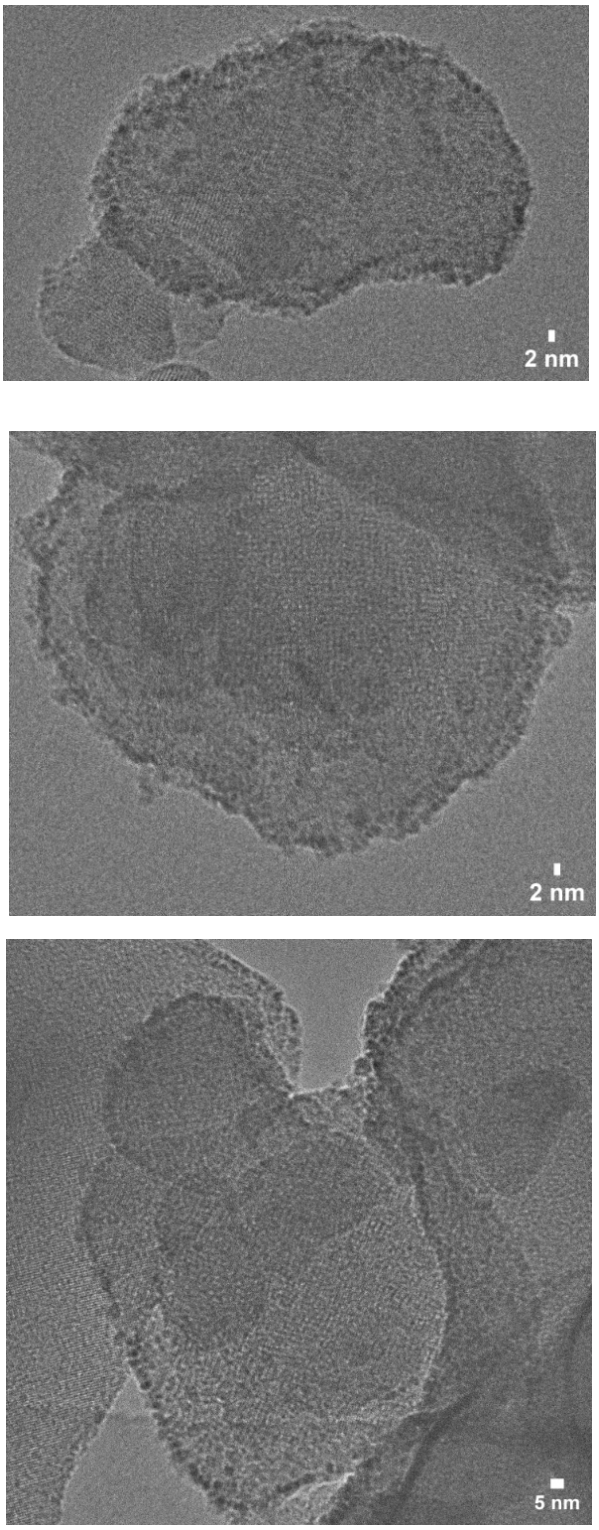

Figure 6.6: Supplementary TEM micrographs of Ni @ UiO-66(NH_2), which images were used to measure particle sizes.

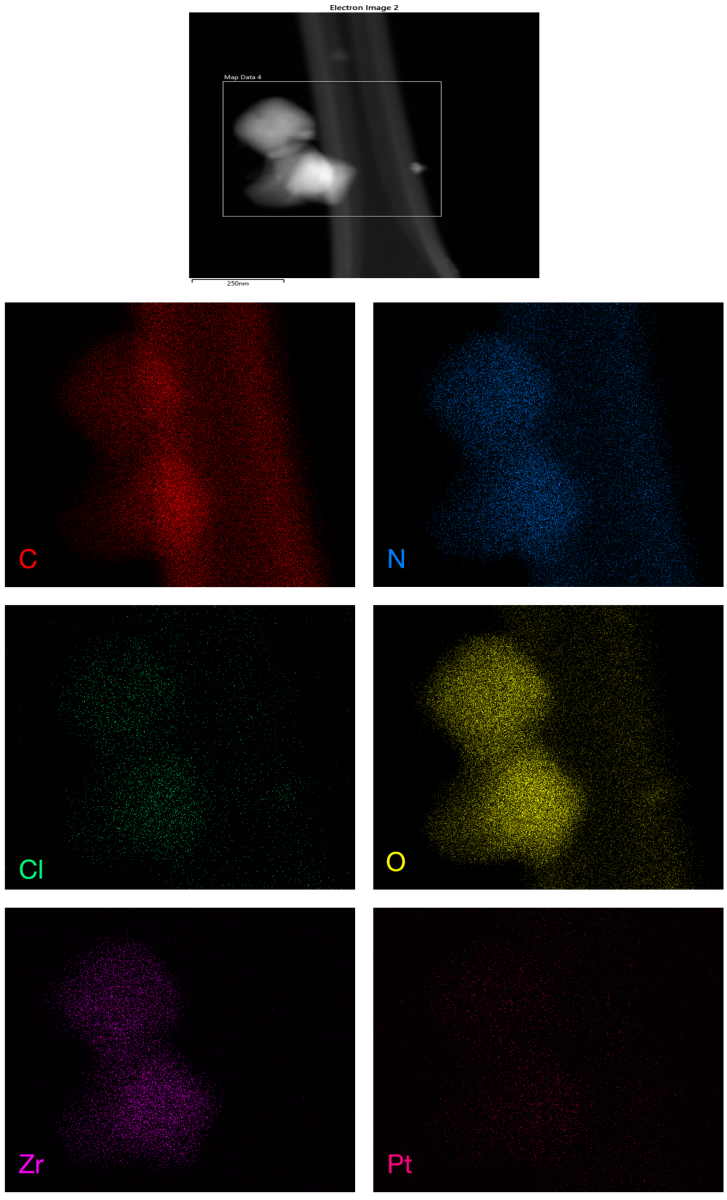

Figure 6.7: EDX mapping of Pt @ UiO-66(NH_2) after Pt deposition by magnetron sputtering.

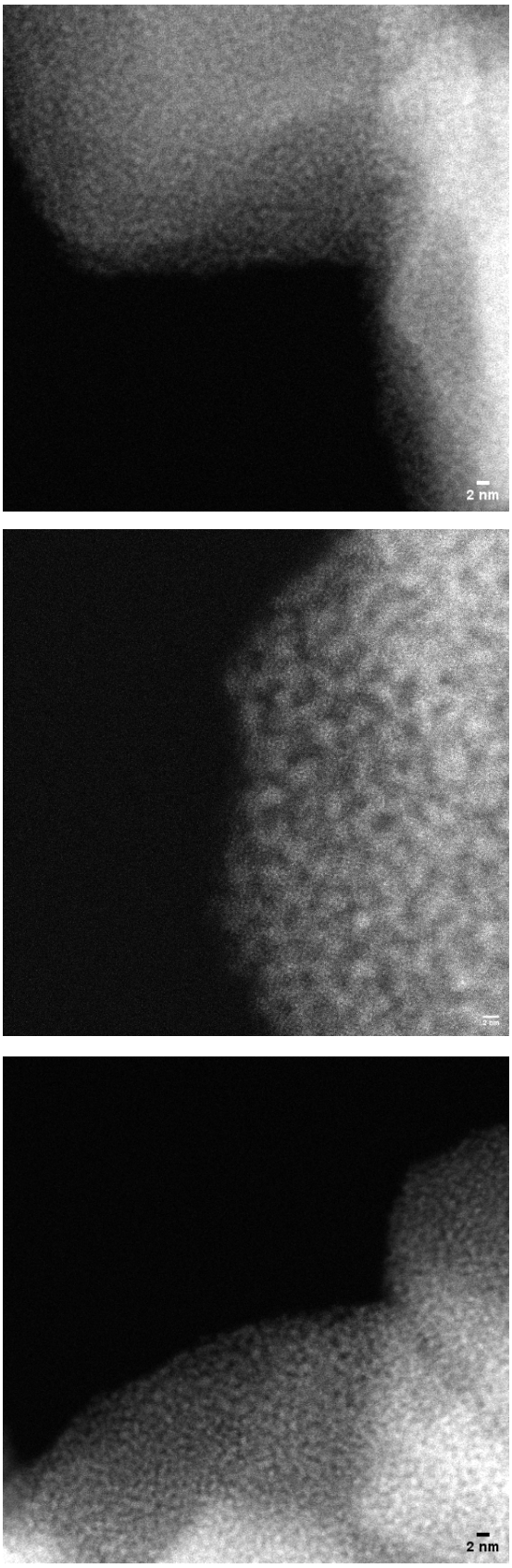

Figure 6.8: Attempts at imaging Pt @ UiO-66(NH_2) using STEM. It is impossible to image the material properly, due to electron beam-induced damage.

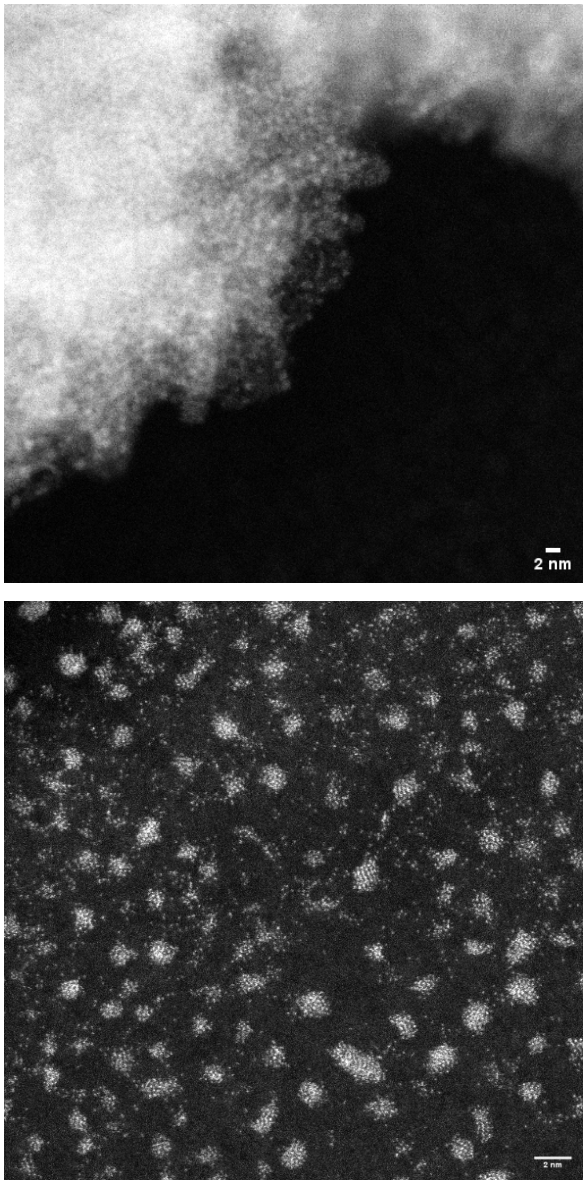

Figure 6.9: Two images from the same TEM grid, which was deposited with Pt directly, so that Pt is present on both UiO-66(NH_2) and holey carbon of the grid. (Upper) Imaging Pt @ UiO-66(NH_2), where Pt particle size is extremely difficult to measure due to highly scattering Zr and beam sensitivity. (Lower) Imaging Pt deposited onto the holey carbon of the TEM grid, where Pt particles are clearly defined and easy to measure.

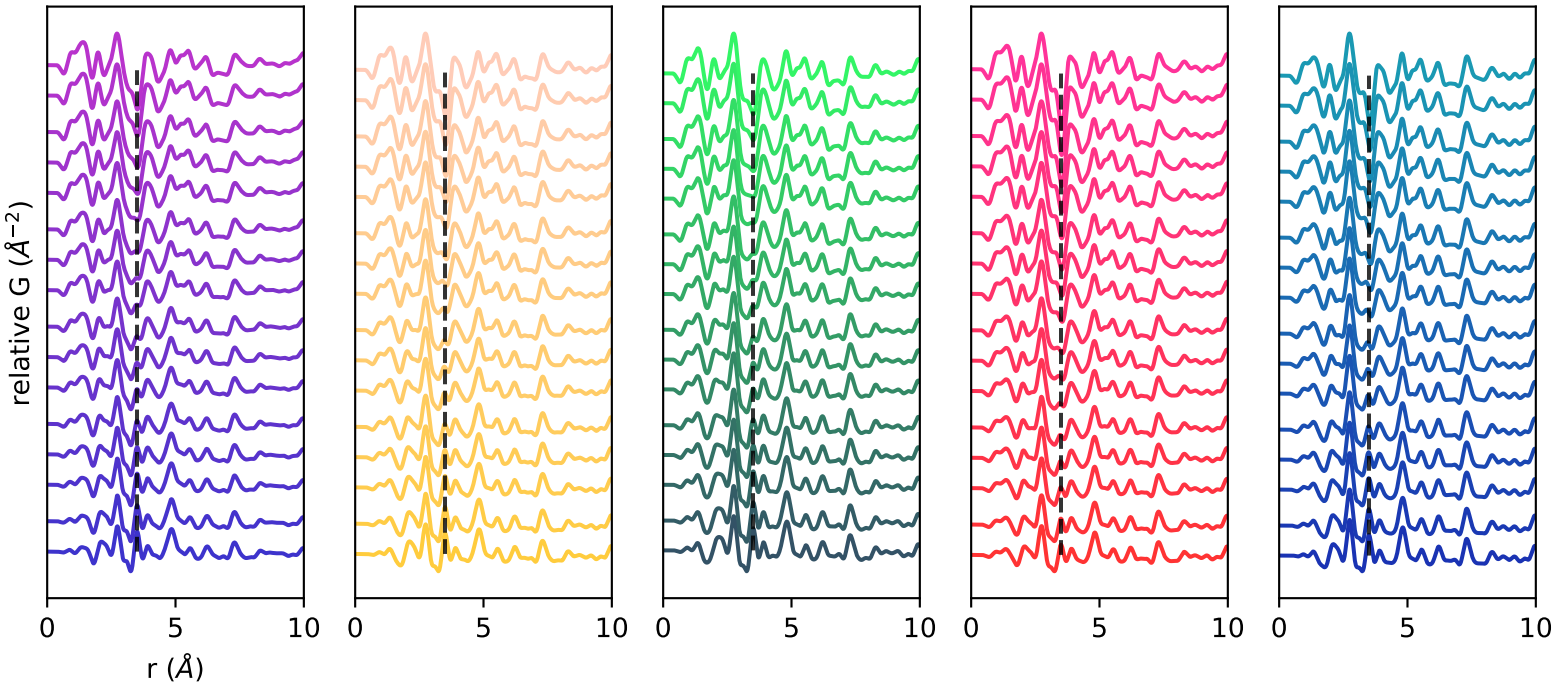

Figure 6.10: Subtraction of base MOF from PDF of Pt@UiO-66(NH_2) after 2.5 and 24 hours of photocatalytic exposure. x= 0.70 was used for final subtractions, as this is the subtraction coefficient which best neutralises the intracluster Zr-Zr correlation at 3.5 Å(dashed black line)

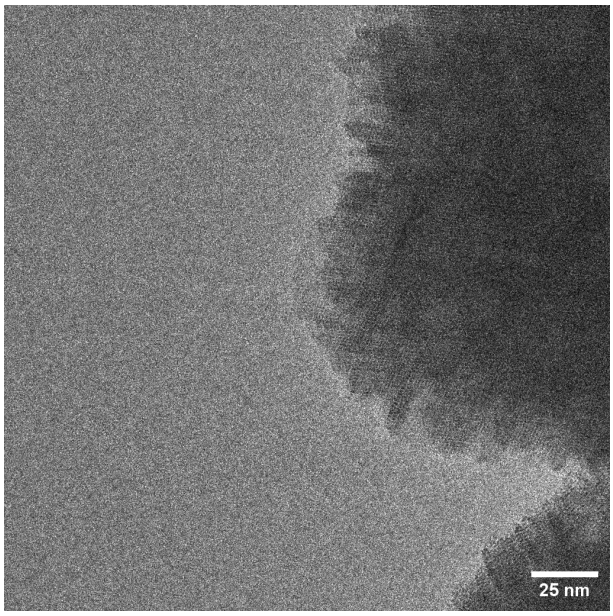

Figure 6.11: An image of Pt @ UiO-66(NH_2) captured with 80 kv electrons, with the aim to minimise beam damage. The lower energy electrons produce poorly resolved images

References

1 S. M. Stratton, S. Zhang and M. M. Montemore, *Surface Science Reports*, 2023, **78**, 100597.

2 A. Kuriganova, N. Faddeev, M. Gorshenkov, D. Kuznetsov, I. Leontyev and N. Smirnova, *Processes*, 2020, **8**, 947.

3 R. Kukla, *Surface and Coatings Technology*, 1997, **93**, 1–6.

4 J. T. Gudmundsson and A. Hecimovic, *Plasma Sources Science and Technology*, DOI:10.1088/1361-6595/aa940d.

5 B. Cornils and W. A. Herrmann, in *Journal of Catalysis*, Academic Press Inc., 2003, vol. 216, pp. 23–31.

6 United Nations, https://www.un.org/sustainabledevelopment/sustainable-consumption-production/, accessed 29/05/2022,.

7 Johnson Matthey, http://www.platinum.matthey.com/services/market-research/market-data-tables, accessed 25/05/2022,.

8 International Platinum Group Metals Association, https://ipa-news.com/assets/sustainability/IPA_Guidance/2022-06-21-LCA%20Fact%20Sheet%202022_IPA.pdf, accessed 20/08/2024, 2024.

9 B. H. Lipshutz, B. A. Frieman, C. T. Lee, A. Lower, D. M. Nihan and B. R. Taft, *Chemistry - An Asian Journal*, 2006, **1**, 417–429.

10 X. F. Yang, A. Wang, B. Qiao, J. Li, J. Liu and T. Zhang, *Accounts of Chemical Research*, 2013, **46**, 1740–1748.

11 J. Aarons, M. Sarwar, D. Thompsett and C.-K. Skylaris, *The Journal of Chemical Physics*, 2016, **145**, 220901.

12 J. M. Rahm and P. Erhart, *Nano Letters*, 2017, **17**, 5775–5781.

13 L. Liu and A. Corma, *Chemical Reviews*, 2018, **118**, 4981–5079.

14 S. Hejazi, S. Mohajernia, B. Osuagwu, G. Zoppellaro, P. Andryskova, O. Tomanec, S. Kment, R. Zbořil and P. Schmuki, *Advanced Materials*, 2020, **32**, 1908505.

15 S. Liang, C. Hao and Y. Shi, *ChemCatChem*, 2015, **7**, 2559–2567.

16 L. Zhang, Y. Ren, W. Liu, A. Wang and T. Zhang, *National Science Review*, 2018, **5**, 653–672.

17 S. F. J. Hackett, R. M. Brydson, M. H. Gass, I. Harvey, A. D. Newman, K. Wilson and A. F. Lee, *Angewandte Chemie*, 2007, **119**, 8747–8750.

18 M. Moliner, J. E. Gabay, C. E. Kliewer, R. T. Carr, J. Guzman, G. L. Casty, P. Serna and A. Corma, *Journal of the American Chemical Society*, 2016, **138**, 15743–15750.

19 B. Qiao, A. Wang, X. Yang, L. F. Allard, Z. Jiang, Y. Cui, J. Liu, J. Li and T. Zhang, *Nature Chemistry*, 2011, **3**, 634–641.

20 S. Nahar, M. F. M. Zain, A. A. H. Kadhum, H. A. Hasan and M. R. Hasan, *Materials*, 2017, **10**, 629.

21 C. Acar, I. Dincer and C. Zamfirescu, *International Journal of Energy Research*, 2014, **38**, 1903–1920.

22 Suresh C. Pillai, Vignesh Kumarave, *Photocatalysis*, De Gruyter.

23 P. T. Anastas and J. C. Warner, *Green Chemistry: Theory and Practice*, Oxford University Press: New York, 1998.

24 B. Ohtani, *Catalysts*, 2013, **3**, 942–953.

25 X. Wei, X. He, P. Wu, F. Gong, D. Wang, S. Wang, S. Lu, J. Zhang, S. Xiang, T. Kai and P. Ding, *International Journal of Hydrogen Energy*, 2021, **46**, 27974–27996.

26 X. Li, J. Yu, J. Low, Y. Fang, J. Xiao and X. Chen, *Journal of Materials Chemistry A*, 2015, **3**, 2485–2534.

27 Z. Zhang and J. T. Yates, *Chemical Reviews*, 2012, **112**, 5520–5551.

28 N. Fajrina and M. Tahir, *International Journal of Hydrogen Energy*, 2019, **44**, 540–577.

29 R. T. Tung, *Materials Science and Engineering: R: Reports*, 2001, **35**, 1–138.

30 H. Idriss, *Current Opinion in Chemical Engineering*, 2020, **29**, 74–82.

31 S. A. Bhat and J. Sadhukhan, *AIChE Journal*, 2009, **55**, 408–422.

32 M. Voldsund, K. Jordal and R. Anantharaman, *International Journal of Hydrogen Energy*, 2016, **41**, 4969–4992.

33 G. W. Crabtree, M. S. Dresselhaus and M. V. Buchanan, *Physics Today*, 2004, **57**, 39–44.

34 S. Chatterjee, R. K. Parsapur and K.-W. Huang, *ACS Energy Letters*, 2021, **6**, 4390–4394.

35 A. Fujishima and K. Honda, *Nature*, 1972, **238**, 37–38.

36 W. Chen, J. Pei, C.-T. He, J. Wan, H. Ren, Y. Wang, J. Dong, K. Wu, W.-C. Cheong, J. Mao, X. Zheng, W. Yan, Z. Zhuang, C. Chen, Q. Peng, D. Wang and Y. Li, *Advanced Materials*, 2018, **30**, 1800396.

37 Y. Wang, C. Peng, T. Jiang and X. Li, *Frontiers in Energy*, 2021, **15**, 656–666.

38 J.-M. Herrmann, *Catalysis Today*, 1999, **53**, 115–129.

39 Z. H. N. Al-Azri, W.-T. Chen, A. Chan, V. Jovic, T. Ina, H. Idriss and G. I. N. Waterhouse, *Journal of Catalysis*, 2015, **329**, 355–367.

40 S. Sato and J. M. White, *Chemical Physics Letters*, 1980, **72**, 83–86.

41 S. Trasatti, *Journal of Electroanalytical Chemistry and Interfacial Electrochemistry*, 1972, **39**, 163–184.

42 T. Liu, C. Xi, C. Dong, C. Cheng, J. Qin, S. Hu, H. Liu and X.-W. Du, *The Journal of Physical Chemistry C*, 2019, **123**, 28319–28326.

43 L. Valenzano, B. Civalleri, S. Chavan, S. Bordiga, M. H. Nilsen, S. Jakobsen, K. P. Lillerud and C. Lamberti, *Chemistry of Materials*, 2011, **23**, 1700–1718.

44 R. Freund, O. Zaremba, G. Arnauts, R. Ameloot, G. Skorupskii, M. Dincă, A. Bavykina, J. Gascon, A. Ejsmont, J. Goscianska, M. Kalmutzki, U. Lächelt, E. Ploetz, C. S. Diercks and S. Wuttke, *Angewandte Chemie International Edition*, 2021, **60**, 23975–24001.

45 C. Serre, F. Millange, S. Surblé and G. Férey, *Angewandte Chemie International Edition*, 2004, **43**, 6285–6289.

46 J. H. Cavka, S. Jakobsen, U. Olsbye, N. Guillou, C. Lamberti, S. Bordiga and K. P. Lillerud, *Journal of the American Chemical Society*, 2008, **130**, 13850–13851.

47 John-Chu-Chia Hsu, *McGill Green Chemistry Journal*, 2015, **1**, 35.

48 H. Li, M. Eddaoudi, M. O'Keeffe and O. M. Yaghi, *Nature*, 1999, **402**, 276–279.

49 N. Stock and S. Biswas, *Chemical Reviews*, 2012, **112**, 933–969.

50 C. Atzori, G. C. Shearer, L. Maschio, B. Civalleri, F. Bonino, C. Lamberti, S. Svelle, K. P. Lillerud and S. Bordiga, *The Journal of Physical Chemistry C*, 2017, **121**, 9312–9324.

51 F. C. N. Firth, M. J. Cliffe, D. Vulpe, M. Aragones-Anglada, P. Z. Moghadam, D. Fairen-Jimenez, B. Slater and C. P. Grey, *Journal of Materials Chemistry A*, 2019, **7**, 7459–7469.

52 A. Schaate, P. Roy, A. Godt, J. Lippke, F. Waltz, M. Wiebcke and P. Behrens, *Chemistry – A European Journal*, 2011, **17**, 6643–6651.

53 H. L. B. Boström, S. Emmerling, F. Heck, C. Koschnick, A. J. Jones, M. J. Cliffe, R. Al Natour, M. Bonneau, V. Guillerm, O. Shekhah, M. Eddaoudi, J. Lopez-Cabrelles, S. Furukawa, M. Romero-Angel, C. Martí-Gastaldo, M. Yan, A. J. Morris, I. Romero-Muñiz, Y. Xiong, A. E. Platero-Prats, J. Roth, W. L. Queen, K. S. Mertin, D. E. Schier, N. R. Champness, H. H.-M. Yeung and B. V. Lotsch, *Advanced Materials*, 2024, **36**, 2304832.

54 G. C. Shearer, S. Chavan, J. Ethiraj, J. G. Vitillo, S. Svelle, U. Olsbye, C. Lamberti, S. Bordiga and K. P. Lillerud, *Chemistry of Materials*, 2014, **26**, 4068–4071.

55 F. C. N. Firth, M. W. Gaultois, Y. Wu, J. M. Stratford, D. S. Keeble, C. P. Grey and M. J. Cliffe, *Journal of the American Chemical Society*, 2021, **143**, 19668–19683.

56 H. Xu, S. Sommer, N. L. N. Broge, J. Gao and B. B. Iversen, *Chemistry – A European Journal*, 2019, **25**, 2051–2058.

57 Woodward, Patrick, M.; Karen, Pavel.; Evans, John, O; Vogt, Thomas, *Solid State and Materials Chemistry*, Cambridge University Press, 2021.

58 S. Zhang, J. Gong, S. Chu, D. Z. Xiao, B. Reeja-Jayan and A. J. H. McGaughey, *APL Machine Learning*, 2023, **1**, 026115.

59 Anton Kelly and Kevin M. Knowles, *Crystallography and Crystal Defects*, Wiley, 2nd edn.

60 J. He and S. B. Sinnott, *Journal of the American Ceramic Society*, 2005, **88**, 737–741.

61 C. Falaise, C. Volkringer, J.-F. Vigier, N. Henry, A. Beaurain and T. Loiseau, *Chemistry – A European Journal*, 2013, **19**, 5324–5331.

62 R. M. Rego, G. Sriram, K. V. Ajeya, H.-Y. Jung, M. D. Kurkuri and M. Kigga, *Journal of Hazardous Materials*, 2021, **416**, 125941.

63 Z. Wang, A. Bilegsaikhan, R. T. Jerozal, T. A. Pitt and P. J. Milner, *ACS Applied Materials & Interfaces*, 2021, **13**, 17517–17531.

64 L. Wang, J. Li, L. Cheng, Y. Song, P. Zeng and X. Wen, *Journal of Materials Chemistry A*, 2021, **9**, 14868–14876.

65 C. A. Trickett, K. J. Gagnon, S. Lee, F. Gándara, H.-B. Bürgi and O. M. Yaghi, *Angewandte Chemie International Edition*, 2015, **54**, 11162–11167.

66 S. Ling and B. Slater, *Chemical Science*, 2016, **7**, 4706–4712.

67 A. De Vos, K. Hendrickx, P. Van Der Voort, V. Van Speybroeck and K. Lejaeghere, *Chemistry of Materials*, 2017, **29**, 3006–3019.

68 M. J. Cliffe, W. Wan, X. Zou, P. A. Chater, A. K. Kleppe, M. G. Tucker, H. Wilhelm, N. P. Funnell, F. X. Coudert and A. L. Goodwin, *Nature Communications*, DOI:10.1038/ncomms5176.

69 O. V. Gutov, M. G. Hevia, E. C. Escudero-Adán and A. Shafir, *Inorganic Chemistry*, 2015, **54**, 8396–8400.

70 L. Liu, Z. Chen, J. Wang, D. Zhang, Y. Zhu, S. Ling, K.-W. Huang, Y. Belmabkhout, K. Adil, Y. Zhang, B. Slater, M. Eddaoudi and Y. Han, *Nature Chemistry*, 2019, **11**, 622–628.

71 C. Caratelli, J. Hajek, F. G. Cirujano, M. Waroquier, F. X. Llabrés I Xamena and V. Van Speybroeck, *Journal of Catalysis*, 2017, **352**, 401–414.

72 H. Wu, Y. S. Chua, V. Krungleviciute, M. Tyagi, P. Chen, T. Yildirim and W. Zhou, *Journal of the American Chemical Society*, 2013, **135**, 10525–10532.

73 F. Vermoortele, B. Bueken, G. Le Bars, B. Van De Voorde, M. Vandichel, K. Houthoofd, A. Vimont, M. Daturi, M. Waroquier, V. Van Speybroeck, C. Kirschhock and D. E. De Vos, *Journal of the American Chemical Society*, 2013, **135**, 11465–11468.

74 W. Xiang, J. Ren, S. Chen, C. Shen, Y. Chen and M. Zhang, *Applied Energy*, 2020, **277**, 115560.

75 X. Feng, H. S. Jena, C. Krishnaraj, K. Leus, G. Wang, H. Chen, C. Jia and P. V. D. Voort, *ACS Applied Materials & Interfaces*, DOI:10.1021/acsami.1c13525.

76 L. Liu, S. Du, X. Guo, Y. Xiao, Z. Yin, N. Yang, Y. Bao, X. Zhu, S. Jin, Z. Feng and F. Zhang, *Journal of the American Chemical Society*, 2022, **144**, 2747–2754.

77 Z. Wang, A. Bilegsaikhan, R. T. Jerozal, T. A. Pitt and P. J. Milner, *ACS Applied Materials & Interfaces*, 2021, **13**, 17517–17531.

78 F. G. Cirujano and F. X. Llabrés i Xamena, *The Journal of Physical Chemistry Letters*, 2020, **11**, 4879–4890.

79 W. Xiang, J. Ren, S. Chen, C. Shen, Y. Chen, M. Zhang and C. Liu, *Applied Energy*, 2020, **277**, 115560.

80 A. Jrad, G. Al Sabeh, K. Hannouche, R. Al Natour, O. Haidar, H. Sammoury, M. N. Ahmad and M. Hmadeh, *ACS Applied Nano Materials*, 2023, **6**, 18698–18720.

81 J.-D. Xiao, Q. Shang, Y. Xiong, Q. Zhang, Y. Luo, S.-H. Yu and H.-L. Jiang, *Angewandte Chemie*, 2016, **128**, 9535–9539.

82 W. Zhang, W. Ji, L. Li, P. Qin, I. E. Khalil, Z. Gu, P. Wang, H. Li, Y. Fan, Z. Ren, Y. Shen, W. Zhang, Y. Fu and F. Huo, *ACS Applied Materials & Interfaces*, 2020, **12**, 52660–52667.

83 Y. Yang, D. Zhang, W. Ji, F. Bi, L. Song and X. Zhang, *Journal of Colloid and Interface Science*, 2022, **606**, 1811–1822.

84 C. Castillo-Blas, J. M. Moreno, I. Romero-Muñiz and A. E. Platero-Prats, *Nanoscale*, 2020, **12**, 15577–15587.

85 S. Rangwani, A. J. Howarth, M. R. DeStefano, C. D. Malliakas, A. E. Platero-Prats, K. W. Chapman and O. K. Farha, *Polyhedron*, 2018, **151**, 338–343.

86 K. M. Ø. Jensen, M. Christensen, P. Juhas, C. Tyrsted, E. D. Bøjesen, N. Lock, S. J. L. Billinge and B. B. Iversen, *Journal of the American Chemical Society*, 2012, **134**, 6785–6792.

87 A. E. Platero-Prats, Z. Li, L. C. Gallington, A. W. Peters, J. T. Hupp, O. K. Farha and K. W. Chapman, *Faraday Discussions*, 2017, **201**, 337–350.

88 A. E. Platero-Prats, A. B. League, V. Bernales, J. Ye, L. C. Gallington, A. Vjunov, N. M. Schweitzer, Z. Li, J. Zheng, B. L. Mehdi, A. J. Stevens, A. Dohnalkova, M. Balasubramanian, O. K. Farha, J. T. Hupp, N. D. Browning, J. L. Fulton, D. M. Camaioni, J. A. Lercher, D. G. Truhlar, L. Gagliardi, C. J. Cramer and K. W. Chapman, *Journal of the American Chemical Society*, 2017, **139**, 10410–10418.

89 M. A. Newton, K. W. Chapman, D. Thompsett and P. J. Chupas, *Journal of the American Chemical Society*, 2012, **134**, 5036–5039.

90 P. J. Chupas, K. W. Chapman, H. Chen and C. P. Grey, *Catalysis Today*, 2009, **145**, 213–219.

91 S. Banerjee, C.-H. Liu, J. D. Lee, A. Kovyakh, V. Grasmik, O. Prymak, C. Koenigsmann, H. Liu, L. Wang, A. M. M. Abeykoon, S. S. Wong, M. Epple, C. B. Murray and S. J. L. Billinge, *The Journal of Physical Chemistry C*, 2018, **122**, 29498–29506.

92 S. Muhamed, A. R. Kandy, A. Karmakar, S. Kundu and S. Mandal, *Inorganic Chemistry*, 2022, **61**, 13271–13275.

93 Martin T. Dove, *Structure and Dynamics: An Atomic View of Materials*, Oxford University Press.

94 D. Balzar, N. Audebrand, M. R. Daymond, A. Fitch, A. Hewat, J. I. Langford, A. Le Bail, D. Louër, O. Masson, C. N. McCowan, N. C. Popa, P. W. Stephens and B. H. Toby, *Journal of Applied Crystallography*, 2004, **37**, 911–924.

95 A. A. Coelho, *Journal of Applied Crystallography*, 2018, **51**, 210–218.

96 D. Sun, Y. Fu, W. Liu, L. Ye, D. Wang, L. Yang, X. Fu and Z. Li, *Chemistry – A European Journal*, 2013, **19**, 14279–14285.

97 A. Huang, L. Wan and J. Caro, *Materials Research Bulletin*, 2018, **98**, 308–313.

98 S. S. Chen, C. Hu, C.-H. Liu, Y.-H. Chen, T. Ahamad, S. M. Alshehri, P.-H. Huang and K. C.-W. Wu, *Journal of Hazardous Materials*, 2020, **397**, 122431.

99 J. Sui, H. Liu, S. Hu, K. Sun, G. Wan, H. Zhou, X. Zheng and H.-L. Jiang, *Advanced Materials*, 2022, **34**, 2109203.

100 L. Zhang, X. Zhao, Z. Yuan, M. Wu and H. Zhou, *Journal of Materials Chemistry A*, 2021, **9**, 3855–3879.

101 J. Canivet, M. Vandichel and D. Farrusseng, *Dalton Transactions*, 2016, **45**, 4090–4099.

102 L. Zhang, Y. Jia, G. Gao, X. Yan, N. Chen, J. Chen, M. T. Soo, B. Wood, D. Yang, A. Du and X. Yao, *Chem*, 2018, **4**, 285–297.

103 C. Yang, Y. Lu, L. Zhang, Z. Kong, T. Yang, L. Tao, Y. Zou and S. Wang, *Small Structures*, 2021, **2**, 2100058.

104 D. Olds, H.-W. Wang and K. Page, *Journal of Applied Crystallography*, 2015, **48**, 1651–1659.

105 T. W. Hansen, A. T. Delariva, S. R. Challa and A. K. Datye, *Accounts of Chemical Research*, 2013, **46**, 1720–1730.

106 N. Rao, M. N. Holerca, M. L. Klein and V. Pophristic, *The Journal of Physical Chemistry A*, 2007, **111**, 11395–11399.

107 M. J. Cliffe, W. Wan, X. Zou, P. A. Chater, A. K. Kleppe, M. G. Tucker, H. Wilhelm, N. P. Funnell, F. X. Coudert and A. L. Goodwin, *Nature Communications*, 2014, **5**, 1–8.

108 Y. Feng, Q. Chen, M. Jiang and J. Yao, *Industrial & Engineering Chemistry Research*, 2019, **58**, 17646–17659.

109 B. Bueken, N. Van Velthoven, A. Krajnc, S. Smolders, F. Taulelle, C. Mellot-Draznieks, G. Mali, T. D. Bennett and D. De Vos, *Chemistry of Materials*, 2017, **29**, 10478–10486.

110 H. Wu, Y. S. Chua, V. Krungleviciute, M. Tyagi, P. Chen, T. Yildirim and W. Zhou, *Journal of the American Chemical Society*, 2013, **135**, 10525–10532.

111 P. Brault, C. Josserand, J. M. Bauchire, A. Caillard, C. Charles and R. W. Boswell, *Physical Review Letters*, DOI:10.1103/PhysRevLett.102.045901.

112 T. Egami and S. J. L. Billinge, *Underneath the Bragg peaks: Structural analysis of complex materials*, Pergamon, Kiddington, Oxford, UK Boston, 2003.

113 E.-S. Jeong, C.-I. Park, Z. Jin, I.-H. Hwang, J.-K. Son, M.-Y. Kim, J.-S. Choi and S.-W. Han, *Catalysis Letters*, 2015, **145**, 971–983.

114 J.-B. Han, N. Wang, G.-P. Yu, Z.-H. Wei, Z.-G. Zhou and Q.-Q. Wang, *Solar Energy Materials and Solar Cells*, 2005, **88**, 293–299.

115 W. Raza, A. B. Tesler, A. Mazare, O. Tomanec, S. Kment and P. Schmuki, *ChemCatChem*, 2023, **15**, e202300327.

116 X. Wang, W. Zhang, R. Li, J. Han, J. Guo and B. Liu, *Reaction Kinetics, Mechanisms and Catalysis*, 2020, **129**, 505–518.

117 S. Wang, Z. Ai, X. Niu, W. Yang, R. Kang, Z. Lin, A. Waseem, L. Jiao and H.-L. Jiang, *Advanced Materials*, 2023, **35**, 2302512.

118 X. Peng, L. Ye, Y. Ding, L. Yi, C. Zhang and Z. Wen, *Applied Catalysis B: Environmental*, 2020, **260**, 118152.

119 C. Gomes Silva, I. Luz, F. X. Llabrés i Xamena, A. Corma and H. García, *Chemistry – A European Journal*, 2010, **16**, 11133–11138.

120 A. Y. Shan, T. I. Mohd. Ghazi and S. A. Rashid, *Applied Catalysis A: General*, 2010, **389**, 1–8.

121 A. Di Mauro, M. E. Fragalà, V. Privitera and G. Impellizzeri, *Materials Science in Semiconductor Processing*, 2017, **69**, 44–51.

122 L. Lüer, H.-J. Egelhaaf, D. Oelkrug, G. Cerullo, G. Lanzani, B.-H. Huisman and D. de Leeuw, *Organic Electronics*, 2004, **5**, 83–89.

123 D. Shukla, Y. S. Negi, J. S. Uppadhyaya and V. Kumar, *Polymer Reviews*, 2012, **52**, 189–228.

124 V. Mylläri, T.-P. Ruoko and P. Järvelä, *Polymer Degradation and Stability*, 2014, **109**, 278–284.

125 C. Acar, I. Dincer and G. F. Naterer, *International Journal of Energy Research*, 2016, **40**, 1449–1473.

126 X. Peng, L. Ye, Y. Ding, L. Yi, C. Zhang and Z. Wen, *Applied Catalysis B: Environmental*, 2020, **260**, 118152.

127 Nickel Insitute, https://nickelinstitute.org/en/nickel-applications, accessed 27/09/2024,.

128 G. M. Mudd, *Ore Geology Reviews*, 2010, **38**, 9–26.

129 G. A. Campbell, *Mineral Economics*, 2020, **33**, 21–28.

130 G. Bartzas and K. Komnitsas, *Science of The Total Environment*, 2024, **952**, 175902.

131 H. Kawano, *Progress in Surface Science*, 2022, **97**, 100583.

132 K. Domen, S. Naito, M. Soma, T. Onishi and K. Tamaru, *Journal of the Chemical Society, Chemical Communications*, 1980, 543–544.

133 C.-C. Hu and H. Teng, *Journal of Catalysis*, 2010, **272**, 1–8.

134 Y. Yamada, T. Miyahigashi, H. Kotani, K. Ohkubo and S. Fukuzumi, *Energy & Environmental Science*, 2012, **5**, 6111.

135 S. Cao, C.-J. Wang, X.-J. Lv, Y. Chen and W.-F. Fu, *Applied Catalysis B: Environmental*, 2015, **162**, 381–391.

136 H. Husin, W.-N. Su, H.-M. Chen, C.-J. Pan, S.-H. Chang, J. Rick, W.-T. Chuang, H.-S. Sheu and B.-J. Hwang, *Green Chemistry*, 2011, **13**, 1745–1754.

137 P. Salcedo-Abraira, S. M. F. Vilela, A. A. Babaryk, M. Cabrero-Antonino, P. Gregorio, F. Salles, S. Navalón, H. García and P. Horcajada, *Nano Research*, 2021, **14**, 450–457.

138 Z.-Y. Wang, B. Zhang, S. Liu, G.-R. Li, T. Yan and X.-P. Gao, *Advanced Functional Materials*, 2022, **32**, 2200893.

139 S. Ekeroth, J. Ekspong, D. K. Perivoliotis, S. Sharma, R. Boyd, N. Brenning, E. Gracia-Espino, L. Edman, U. Helmersson and T. Wågberg, *ACS Applied Nano Materials*, 2021, **4**, 12957–12965.

140 Z. Cao, Q. Chen, J. Zhang, H. Li, Y. Jiang, S. Shen, G. Fu, B. Lu, Z. Xie and L. Zheng, *Nature Communications*, 2017, **8**, 15131.

141 W. Hou and S. B. Cronin, *Advanced Functional Materials*, 2013, **23**, 1612–1619.

142 D. A. Keen and M. T. Dove, *Journal of Physics: Condensed Matter*, 1999, **11**, 9263.

143 R.-J. Liu, P. A. Crozier, C. M. Smith, D. A. Hucul, J. Blackson and G. Salaita, *Applied Catalysis A: General*, 2005, **282**, 111–121.

144 Inorganic Crystal Structure Database, https://www.psds.ac.uk/, accessed 30/09/2024,.

145 Z. Jiang, Y. Zheng, L. Zhang, L. Xu, Q. Feng, C. Luo, W. Tan and J. Wang, *International Journal of Hydrogen Energy*, 2024, **82**, 703–712.